Space Sci Rev (2012) 170:641–737
DOI 10.1007/s11214-012-9916-y

Selection of the Mars Science Laboratory Landing Site

M. Golombek · J. Grant · D. Kipp · A. Vasavada · R. Kirk · R. Fergason · P. Bellutta · F. Calef · K. Larsen · Y. Katayama · A. Huertas · R. Beyer · A. Chen · T. Parker · B. Pollard · S. Lee · Y. Sun · R. Hoover · H. Sladek · J. Grotzinger · R. Welch · E. Noe Dobrea · J. Michalski · M. Watkins

Received: 20 October 2011 / Accepted: 25 June 2012 / Published online: 21 July 2012

Abstract The selection of Gale crater as the Mars Science Laboratory landing site took over five years, involved broad participation of the science community via five open workshops,

R. Hoover now at Ohio University, Athens, OH 45701.

M. Golombek (✉) · D. Kipp · A. Vasavada · P. Bellutta · F. Calef · Y. Katayama · A. Huertas · A. Chen · T. Parker · B. Pollard · S. Lee · Y. Sun · R. Hoover · H. Sladek · R. Welch · E. Noe Dobrea · J. Michalski · M. Watkins
Jet Propulsion Laboratory, California Institute of Technology, Pasadena, CA 91109, USA
e-mail: mgolombek@jpl.nasa.gov

J. Grant
National Air and Space Museum, Smithsonian Institution, Washington, DC 20560, USA

R. Kirk · R. Fergason
U.S. Geological Survey, Flagstaff, AZ 86001, USA

K. Larsen
Laboratory Atmospheric and Space Physics, University of Colorado, Boulder, CO 80309, USA

Y. Katayama
Lunar and Planetary Exploration Program Group, Japan Aerospace Exploration Agency, Tokyo, Japan

R. Beyer
NASA Ames Research Center, Moffett Field, CA 94035, USA

Y. Sun · J. Grotzinger
California Institute of Technology, Pasadena, CA 91125, USA

R. Hoover
University of Colorado, Boulder, USA

H. Sladek
University of Montana Western, Dillon, MT 59725, USA

E. Noe Dobrea · J. Michalski
Planetary Science Institute, Tucson, AZ 85719, USA

and narrowed an initial >50 sites (25 by 20 km) to four finalists (Eberswalde, Gale, Holden and Mawrth) based on science and safety. Engineering constraints important to the selection included: (1) latitude (±30°) for thermal management of the rover and instruments, (2) elevation (< −1 km) for sufficient atmosphere to slow the spacecraft, (3) relief of <100–130 m at baselines of 1–1000 m for control authority and sufficient fuel during powered descent, (4) slopes of <30° at baselines of 2–5 m for rover stability at touchdown, (5) moderate rock abundance to avoid impacting the belly pan during touchdown, and (6) a radar-reflective, load-bearing, and trafficable surface that is safe for landing and roving and not dominated by fine-grained dust. Science criteria important for the selection include the ability to assess past habitable environments, which include diversity, context, and biosignature (including organics) preservation. Sites were evaluated in detail using targeted data from instruments on all active orbiters, and especially Mars Reconnaissance Orbiter. All of the final four sites have layered sedimentary rocks with spectral evidence for phyllosilicates that clearly address the science objectives of the mission. Sophisticated entry, descent and landing simulations that include detailed information on all of the engineering constraints indicate all of the final four sites are safe for landing. Evaluation of the traversabilty of the landing sites and target "go to" areas outside of the ellipse using slope and material properties information indicates that all are trafficable and "go to" sites can be accessed within the lifetime of the mission. In the final selection, Gale crater was favored over Eberswalde based on its greater diversity and potential habitability.

Keywords Landing sites · Mars · Surface materials · Surface characteristics · Mars Science Laboratory

1 Introduction

The Mars Science Laboratory (MSL) mission is a long-range rover with an analytical laboratory that was launched to Mars on November 26, 2011 (Grotzinger et al. this issue). The spacecraft will land in a small ellipse about 20 by 25 km with the capability to carry out detailed geology, mineralogy, geochemistry and organics investigations. It carries a sample acquisition and processing system for obtaining key samples for the analytic instruments to search for and assess habitable environments. To accomplish these investigations the rover, *Curiosity*, carries a sophisticated suite of instruments that includes remote sensing instruments on a mast, contact sensor instruments on an arm that are placed against soil and rocks, analytic laboratory instruments inside the rover that are fed samples, and atmospheric, and environmental monitoring instruments.

The flight system consists of an aeroshell, backshell and cruise stage (Grotzinger et al. this issue). The spacecraft enters the atmosphere directly from approach and uses the aeroshell and the friction of the atmosphere to initially slow itself. A parachute further slows the spacecraft and the rover is lowered on a tether to the surface, beneath a "sky crane" with the descent propulsion. The rover is placed directly on the surface and the surface mission begins. Because the rover is the first mission designed to traverse out of the ellipse during the nominal mission (1 Mars year), "go to" landing sites in which the area of prime science interest is outside of the landing ellipse were considered.

The process used for selecting the MSL landing site was broadly similar to that used for selection of the Mars Pathfinder (MPF) (Golombek et al. 1997a) and the Mars Exploration Rover (MER) landing sites (Golombek et al. 2003a), which involved close coordination between the engineering and science teams to identify potential landing sites and assess their

safety and included involvement of the broader science community via a series of open workshops. Preliminary engineering constraints were developed early in the process and revised as the spacecraft design matured and was tested. These engineering constraints were used in the initial identification and downselection of potential landing sites. As in previous site selection efforts significant changes in engineering capabilities as well as scientific understanding of Mars occurred during the process and resulted in major changes in the identification and search for landing sites. As examples, elevation and latitude constraints tightened dramatically during the process as the aerodynamic performance and rover design became better understood. In addition, data acquired from the High Resolution Imaging Science Experiment (HiRISE) (McEwen et al. 2007) and the Compact Reconnaissance Imaging Spectrometer for Mars (CRISM) (Murchie et al. 2007) on the Mars Reconnaissance Orbiter (MRO) fundamentally changed our ability to characterize the safety of landing sites and considerably sharpened our understanding of the aqueous mineralogy. These advances, along with the delay in launch from 2009 to 2011, added new opportunities for identifying high science priority landing sites relatively late in the process and required the development of new methods for characterizing the surface at very high resolution.

The ability to characterize the surface in so much detail (most specifically slopes and rocks at the scale of the rover) allowed landing safety to be estimated with high fidelity (certainly beyond any previous landing site selection effort) via simulations. Because most of the high science priority landing sites are "go to" sites involving potentially long traverses, these data were also used to determine the traversability and model the amount of time needed to traverse and exit the ellipse. Finally, improvements in numerical models of Mars' atmosphere and the extensive observational record of atmospheric temperatures and dust activity greatly enhanced the ability to predict conditions and assess safety during entry and descent at specific landing sites.

The MSL landing site selection process has taken about six years beginning with the development of the mission, engineering constraints, and the solicitation of potential landing sites in 2005 (Table 1). The First MSL Landing Site Workshop was held in June 2006 at which about 35 sites were proposed and prioritized for imaging by MRO, which was in orbit, but had not started its nominal mission. These landing sites were imaged by MRO for about a year before the Second MSL Landing Site Workshop was held in October 2007. About 50 landing sites were considered after which six sites were selected for continued imaging and further study. New MRO data resulted in the consideration of four new landing sites in July 2008 and the addition of a seventh site to the short list. The Third MSL Landing Site Workshop was held in September 2008 at which all seven sites were evaluated on their science merit with respect to the MSL science objectives and safety after which they were downselected to four. The launch delay and extensive new remote sensing data acquired allowed the consideration of potential new landing sites in 2009. Two new sites were selected for imaging and evaluated in some detail, but safety concerns resulted in no new sites added to the final four. The final four landing sites were evaluated in detail with respect to their surface characteristics and science at the Fourth and Fifth MSL Landing Site Workshops held in September 2010 and May 2011, respectively. Simulations of entry, descent, landing, and rover operations indicated that all four landing sites were safe for landing and that the rover could traverse out of the ellipse quickly enough to study materials of prime interest during the nominal mission. All four sites were also deemed of high science merit. The selection was evaluated by an external peer review panel in June 2011, deemed to be within planetary protection guidelines, and the Gale crater landing site was selected for MSL by NASA Headquarters in July 2011.

The landing site selection process benefitted from the participation of the broader science community, instrument science teams on active orbiters, project science team members and

Table 1 Major Mars Science Laboratory Landing Site Workshops, activities and selection

Year	Workshop	Science activities and workshop results	Engineering activity
2006	#1 5/31–6/2	35 sites proposed, considered and ranked (Top sites: Holden, Jezero, Mawrth, Miyamoto, Nili Fossae, Terby; Second tier sites: Chloride sites, E Meridiani, Eberswalde, Melas, NE Syrtis)	Constraints defined and refined
2007	#2 10/23–25	50 sites considered from new MRO data; 6 sites selected (Eberwalde, Holden, Mawrth, Miyamoto, Nili Fossae Trough, N Meridiani)	Engineering constraints (e.g., rock abundance, elevation, latitude, etc.) for each site were evaluated
2008	7/8–24	Call for new sites: 4 new sites proposed (Gale, S. Meridiani Planum, Chloride west of Miyamoto, Carbonate in Nili Fossae)	
2008	#3 9/15–17	Steering committee adds 7th site (Gale); 4 sites selected (Eberswalde, Gale, Holden, Mawrth)	
2009		Call for new sites: 7 new sites proposed (Nili Fossae carbonate, NE Syrtis Major*, Xanthe Terra, E Margaritifer*, Ladon basin, Vallis Marineris, Vastitas Borealis), two recommended for additional imaging and analysis by Steering Committee (indicated by *). No sites were added.	Limited ongoing studies
2010	#4 9/27–29	Detailed science evaluations of 4 sites (Eberswalde, Gale, Holden, Mawrth)	Engineering studies
2011	#5 5/16–18	Project recommendation, Independent land site certification review, Planetary protection review, NASA HQ Selection, July 2011	Mature studies (e.g., wheel actuators, thermal)

engineering personnel, and project and program personnel at JPL and NASA Headquarters. The overall landing site analysis and selection process was managed by the MSL Mission System Manager (M. Watkins) with science leadership from the MSL Project Scientist (J. Grotzinger) and Deputy Project Scientist (A. Vasavada). A NASA appointed MSL Landing Site Steering Committee (Table 2), co-chaired by two competitively selected individuals (M. Golombek and J. Grant), oversaw the external community process and provided expertise and made decisions that could not be scheduled during open workshops. Some funding for investigators was provided from the NASA Mars Data Analysis Program. Special data products and studies were also funded by the Critical Data Products (CDP) program sponsored by the JPL Mars Exploration Program office. These data products yielded quantitative maps of atmospheric conditions (temperatures and dust storms), as well as surface properties (thermal inertia, rock abundance, and topography) that enabled high-fidelity simulations of the landing process for estimating landing site safety and traversability. Detailed engineering analyses from a safety perspective (including simulations) were conducted by the MSL systems engineering team, working closely with the CDP investigators and the JPL Mars Exploration Program Landing Site Scientist (M. Golombek). Two groups, the Council of Terrains and the Council of Atmospheres, composed of project personnel and scientists working on data products met regularly during the landing site selection process.

Table 2 Mars Science Laboratory landing site steering committee

Name	Affiliation
John Grant[a]	Smithsonian Institution
Matthew Golombek[a]	Jet Propulsion Laboratory
Philip Christensen	Arizona State University
David DesMarais	Ames Research Center
John Grotzinger	California Institute of Technology
Virginia Gulick	NASA Ames Research Center
Bruce Jakosky	University of Colorado
Michael Malin[b]	Malin Space Science Systems
Alfred McEwen	University of Arizona
Douglas Ming	Johnson Space Center
Richard Morris	Johnson Space Center
Jack Mustard	Brown University
Timothy Parker	Jet Propulsion Laboratory
Roger Phillips	Washington University
	Southwest Research Institute
Dawn Sumner	University of California, Davis
Kenneth Tanaka	U.S. Geological Survey, Flagstaff
Richard Zurek	Jet Propulsion Laboratory

[a]Committee co-chairs

[b]Replaced by Kenneth Edgett, Malin Space Science Systems in 2011

This paper documents the selection of the MSL landing site. We begin by describing the engineering constraints on possible landing sites (e.g., ellipse size, latitude, elevation, slopes, rocks and surface properties) derived from the spacecraft and the entry, descent and landing (EDL) scenario and how they have changed throughout the selection process (Sect. 2). Next we describe the planetary protection constraints (Sect. 3) and the science objectives of the mission (Sect. 4). The data used to evaluate landing sites are described in Sect. 5 and the definition and properties of the atmosphere are described in Sect. 6. We provide a historical account of the landing site downselection activities that occurred and the results of the landing site workshops in Sect. 7 and describe the science attributes of the final four landing sites in Sect. 8. The surface characteristics of the final landings sites are described, judged against the engineering constraints, and compared to previous landing sites in Sect. 9. The engineering simulations to determine the probability of successful landing at each of the sites are presented in Sect. 10 and the traversability of the sites and "go to" areas is described in Sect. 11. We conclude in Sect. 12 with the final deliberations and landing site selection.

2 Landing Site Engineering Constraints

2.1 MSL Entry, Descent and Landing

The MSL EDL includes several innovations that particularly improved the science of landing site selection. First, inclusion of entry guidance in the architecture allows the spacecraft to actively control range flown through the use of bank angle modulation to steer the vehicle (aero-maneuvering) during hypersonic flight (Steltzner et al. 2006). The spacecraft flies almost 50 km farther downrange than simple ballistic descents and thus uses more of the atmosphere to slow down the spacecraft (Kipp et al. 2007). A major benefit of entry guidance

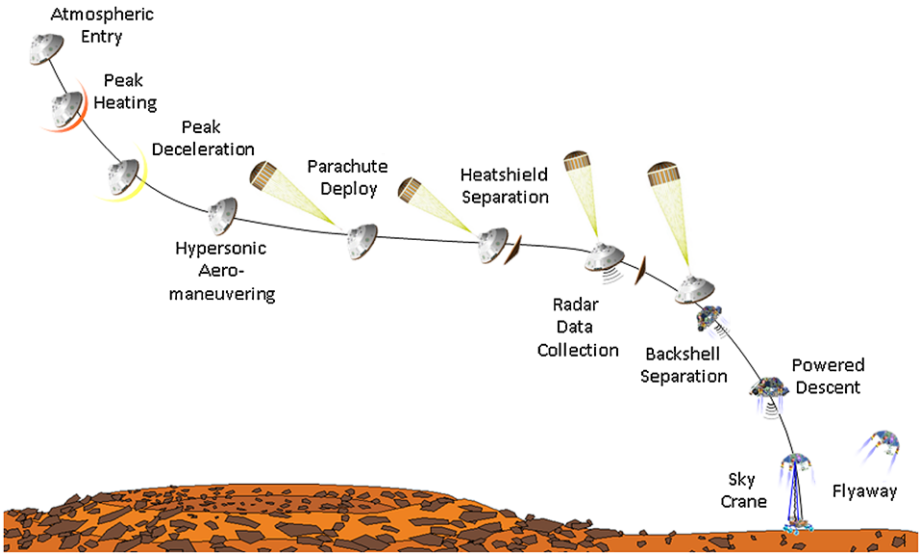

Fig. 1 Entry, descent and landing sequence for the Mars Science Laboratory from cruise stage separation through landing. The main events during EDL are atmospheric slowing behind the heat shield and aeromaneuvering, parachute deployment, powered descent and landing beneath the sky crane

for the site selection process is a dramatically smaller landing ellipse than that of previous Mars missions. Previous spacecraft that used uncontrolled ballistic descent had best case landing ellipses that were around 100 km long. With areo-maneuvering, MSL's margined landing ellipse is about 25 km long. Because landing sites must avoid craters and steep or rugged terrain, the smaller ellipse allowed dramatically more ellipses to be considered for MSL than any other Mars landed mission. Another benefit of this smaller ellipse (and the expected long range of the MSL rover), was the ability to consider "go to" landing sites for the first time, in which landing occurred in smooth, flat terrain next to areas of prime scientific interest. Secondly, development of the sky crane landing technique created a landing system significantly more robust to high surface slopes during touchdown when compared to prior Mars missions. This allowed the consideration of substantially rougher landing sites than could be considered for past missions.

The MSL EDL sequence of events is shown in Fig. 1 (Steltzner et al. 2006; Prakash et al. 2008). Entry interface is defined as occurring when the vehicle reaches a radius of 3522.2 km from the center of Mars, which is roughly atmospheric entry. Prior to atmospheric entry the entry vehicle separates from the cruise stage and jettisons two cruise balance masses. These masses allow for a centrally balanced spacecraft during spinning cruise that after jettisoning create an offset center-of-gravity that results in an aerodynamic lifting force on the vehicle during entry. The orientation of this lifting force is controlled by use of roll thrusters in order to guide the spacecraft towards its target on the surface (Mendeck and Craig 2011).

After atmospheric entry, the vehicle experiences peak heating and peak deceleration while performing hypersonic aero-maneuvering to control the range flown prior to parachute deployment. Parachute deployment is triggered after the vehicle has slowed to approximately Mach 1.7 and heatshield separation is triggered after the vehicle has slowed to approximately Mach 0.8. After jettisoning the heatshield the Terminal Descent Sensor (TDS) begins acquiring radar measurements of the surface that enable on-board determination of

Table 3 Summary of final landing site engineering constraints

Engineering parameter	Requirement	Origin
Latitude	$\pm 30°$	Thermal management
Elevation	< -1 km with respect to MOLA geoid	Sufficient atmosphere to slow spacecraft
Ellipse dimension	25 km by 20 km, roughly E–W	Aero-maneuvering accuracy
Terrain relief 1–1000 m baselines	100–130 m	Control authority and sufficient fuel during powered descent
Slopes at 2–5 m length scale	$<30°$	Rover stability at touchdown
Rock height and abundance	Less than 0.5 % probability of at least one $\leq$0.55 m high rock in 4 m^2 area, Equivalent to rock abundance of <8 %	Impacting rover belly pan or inside of wheels during touchdown
Radar reflectivity	Ka band reflective with radar backscatter cross section between -20 dB and 15 dB	Radar altimeter (TDS) returns during descent
Load bearing surface	Thermal inertia	No sinkage during touchdown
No thick dust deposits	>100 J m^{-2} $s^{-0.5}$ K^{-1} and albedo <0.25, Radar reflectivity >0.01 for load bearing bulk density	Rover trafficability

ground-relative altitude and velocity. TDS measurements continue during parachute deployment until the vehicle reaches its backshell separation altitude, just less than two kilometers above ground level. After backshell separation the spacecraft flies a closed-loop powered descent profile that ends when the sky crane phase begins approximately 20 meters above the surface with nominally zero horizontal velocity and 0.75 m/s vertical velocity. During the sky crane phase the rover is separated from the descent stage and lowered on three nylon bridles while the rover's mobility system is simultaneously deployed to its touchdown configuration. Once the bridles are fully extended the rover is suspended approximately 10 m below the descent stage; which continues to descend at the rate of 0.75 m/s until the rover is placed gently on the surface. After touchdown is sensed, the bridles are cut via pyrotechnically actuated line cutters and the descent stage flies to a safe distance away from the rover before impacting the Martian surface. This EDL scenario and spacecraft and sensor capabilities are what define the engineering constraints on landing sites described next and summarized in Table 3.

2.2 Elevation, Latitude, Ellipse Size and Thermal Constraints

2.2.1 Elevation, Latitude and Ellipse Size

One of the programmatic goals of the MSL mission was to open access to more of Mars through increased EDL and operational capabilities, primarily in terms of landing site latitude, elevation, and the ellipse size. This goal is based on the premise that MSL should be able to follow up on discoveries (e.g., from orbital missions) wherever they might occur, without being limited by the stopping power of the atmosphere above the site (i.e., elevation), the thermal environment, or the presence of nearby hazardous terrain. The MSL mission was not formulated with a particular landing site in mind, but with a large envelope

of capabilities that would allow the selection of a landing site to occur as late as the year of launch, allowing more time for ongoing discovery. The design goals circa 2004 included the capability to survive and operate at latitudes up to ±60° (in order to access ground ice), to reach elevations as high as +2.5 km (in order to access much of the southern highlands), and to land within an ellipse of 10 by 5 km.

Several factors led to a refinement of this capability envelope in 2005–06. As the design of the mission progressed, the engineering challenges associated with these capabilities became better defined. Precision landing (i.e., steering toward a safe spot identified in real time) was removed as a programmatic goal. The Planetary Protection categorization for MSL disallowed landing near ground ice (or liquid water) unless a costly full-spacecraft sterilization was performed (see Sect. 3). Meanwhile, the first set of major discoveries from the Mars Express and Mars Reconnaissance Orbiter missions allowed the science community to begin to constrain the types and locations of sites that would be the most relevant to the mission goals. A list of candidate sites was formulated as part of the first community workshop in May 2006 and contained few sites above 1 km elevation. In consultation with MSL program management at NASA Headquarters in July 2006, the Mars Exploration Program refined the Project-level requirements to be ±45° latitude, +1 km, and a 25 by 20 km ellipse. To allow for further design flexibility as scientific desires and engineering challenges continued to evolve, the Program also set a capability floor of ±30° latitude, 0 km elevation, and a 40 by 40 km ellipse.

Going into the second community workshop in October 2007, the constraints were relatively unchanged: ±45° latitude, +1 km, and a 25 by 20 km ellipse. Based on the scientific discussions of particular sites at this workshop and the realization that telecom (during EDL) and operational performance would be significantly degraded at higher-latitude landing sites, the latitude range was narrowed to ±30° latitude. When four final candidate sites were chosen in November 2008 after the fourth workshop, the elevation requirement was adjusted to 0 km, allowing the EDL engineers to trade that capability to reduce risk in other parts of the EDL design. At this time, sites above −1 km were considered to not have sufficient margin in their EDL timeline and the design was subsequently optimized for the actual sites (highest elevation of −1.4 km). Following selection of the landing site and the successful launch of MSL, the final targeted landing ellipse was 19.7 km by 6.9 km.

2.2.2 Thermal Constraints

The environmental requirements guiding the rover design include ground and air temperatures, atmospheric pressure, atmospheric dust opacity and fallout rates, and wind speeds. Ground and air temperature have the greatest impact on the rover design and are also the most dependent on the landing site (primarily through latitude). The ranges of each parameter required for rover survival and operability were established early in the development phase and therefore reflect the wide latitude (and elevation) range initially considered for landing sites. Some constraints were relaxed as the landing site ranges narrowed.

In colder conditions, more of the rover's electrical power is used for supplementary electrical heating of the various motors, mechanisms, and electronics used for scientific activities. In the coldest conditions, the time and energy required to warm these devices may leave little for science, effectively making the rover non-productive. The lower limit on ground and near-surface air temperature on Mars is set by the condensation point of CO_2, the primary atmospheric constituent. At sites near 60° latitude in winter, the rover could fulfill its mission objectives only if it were able to remain productive when temperatures were fixed at the CO_2 frost point for months at a time. For the finalist sites bounded by 30° latitude, while

transient periods of CO_2 frost temperatures cannot be ruled out, the Project can accept limited productivity at those times without sacrificing mission goals. This allowed the thermal design to view CO_2 frost conditions as a constraint on survival, rather than operability. The rover is designed to survive indefinitely at CO_2 frost temperatures (along with a cold wind and clear atmospheric conditions).

For operability at the finalist sites, the rover was designed to a fictitious, low-thermal-inertia site at 27° south latitude. Thermal inertia is a measure of a surface materials resistance to a change in temperature, so a low thermal inertia site would be where the most extreme winter and summer conditions occur within the ±27° latitude band (due to Mars' eccentric orbit). The rover is designed to operate productively over the ground temperature range expected at this extreme site, approximately −120 °C to 40 °C, though considerably more energy is diverted to electric heaters at the lower end of the range. The near-equatorial and moderate-thermal-inertia Gale crater site has a somewhat reduced range of ground temperatures of approximately −100 °C to +10 °C. Other environmental constraints were considered in the design as well, such as daytime overheating (e.g., on the warmest days expected at the finalist sites along with a dusty rover and no wind), not cooling off sufficiently at night (e.g., on days when nighttime temperatures are unusually warm due to high dust opacity), and part fatigue due to thermal cycling (for low-thermal-inertia sites where the largest diurnal temperature swings occur). The environmental requirements and predictions are more fully described in Vasavada et al. (this issue).

2.3 Slopes and Relief

Prior to the Second Landing Site Workshop, the MSL Project evaluated and published as a user's guide of known or estimated engineering requirements on landing sites based on landing and traversability capabilities (MSL Project 2007). At that time, there were slope constraints at 2–10 km, 1–2 km, 0.2–1 km and 2–5 m that derived from radar spoofing, control authority during powered descent, and rover stability during touchdown. Further study and testing of EDL system design and performance have reduced the number of slope and/or relief constraints to two: (1) relief constraints at 1–1000 m for adequate control authority during powered descent, and (2) 2–5 m slope constraints for rover stability during touchdown.

The main constraint on terrain variability at the 1–1000 meter length scale derives from estimates of TDS performance during descent and relief that might exceed fuel available for landing. This length scale is the furthest distance between the landed position of the rover and locations where the TDS radar beams intersect the surface while measuring altitude during parachute descent. This constraint ensures that the ground altitude solution at backshell separation is a reasonable estimate of the ground altitude at the ultimate touchdown location. This, in turn, ensures proper control authority and fuel consumption during powered descent. Early versions of the user's guide specified a 43 meter maximum relief at length scales up to 1 km, roughly equivalent to a 2.5° slope (MSL Project 2007). Design modifications have since allowed the EDL team to allocate more fuel to powered flight. Current powered flight tuning enables the vehicle to safely accommodate up to 100–130 meters of relief at length scales from 1–1000 m.

At rover length scales (2–5 meters), slope constraints ensure safe loading and stability of the rover during touchdown and trafficability of the rover during initial surface operations. While the vehicle was designed and built to handle 30° slopes, an initial engineering constraint of 15° was specified in early versions of the user's guide (MSL Project 2007). This apparent inconsistency was the result of an engineering test program that was not designed

to demonstrate the capability to land on slopes steeper than 15°. It was later decided to augment the test program to demonstrate capability beyond the initial 15° limit and demonstrate capability up to and even beyond 30°. A more complete discussion of slope tolerance during touchdown is included in Sect. 10, but tests show that risk increases at slopes >30°.

2.4 Rocks

On landing, the area below the rover must be free of rocks capable of damaging the rover's lower structure, or "belly pan," which, as designed, is 0.6 m above the ground. The rover mobility system can accommodate rocks that are 0.55 m high assuming some sinkage. The probability of damaging the rover via landing on high rocks must be a small fraction of the allowable failure probability being book kept for EDL. This allocation implies the probability that a rock taller than 0.55 m occurs in a random sampled area of 4 m^2 (the area of the belly pan including the area out to the wheels) should be less than 0.5 % for the proposed sites. If the rock size-frequency distribution is assumed similar to models based on measured distributions at the existing landing sites (e.g., Golombek and Rapp 1997; Golombek et al. 2003b), this translates to a rock abundance (cumulative area covered by rocks) of <8 %. At the time the initial rock constraint was written, it was expected that the acquisition of very high-resolution images of high-priority landing sites would lead to a means to measure the rocks and thus estimate the hazard directly. HiRISE images have enabled the measurement of large rocks directly from their shadows and a measurement and characterization method was successfully developed for the Phoenix landing site selection (Golombek et al. 2008a), and improved upon for the MSL landing site evaluation (Golombek et al. 2011a, 2012). Subsequent testing and analysis has indicated that the area of greatest concern is just that of the belly pan, which is 2.682 m^2 and can tolarate rocks 0.6 m high; this area and rock height were used in the simulations (Sect. 10).

2.5 Radar Reflectivity and Surface Dust

The surface material at the landing site must: (i) be radar reflective (sufficient radar backscatter cross-section) to enable measurement of altitude and velocity during descent, (ii) bear the load of the rover at landing, (iii) be trafficable by the rover, and (iv) experience a range of temperatures within the limits of the rover design (Sect. 2.2.2). These requirements constrain the radar and thermophysical properties of the surface materials, including albedo, thermal inertia (and bulk density, through the latter), radar backscatter cross-section and reflectivity (and inferred bulk density).

The MSL Terminal Descent Sensor (TDS) is a Ka-band, pulse Doppler system that provides line-of-sight range and velocity estimates from each of 6 antennas. Its unique design described in Pollard and Chen (2009), allows the radar to operate successfully over the extensive altitude range (from above 7 km to rover touchdown) and ground-relative velocity (from up to 160 m/s to sub-1 m/s) of the MSL sky crane.

The TDS is designed to operate over a wide range of surface reflectivities. Given a standard Hagfors (1964) surface radar model and observations of Mars backscatter (Butler 1994), we have shown through analysis and laboratory testing that the radar continues to operate as designed with surfaces up several dB brighter or darker than the backscatter (conservatively assumed to be within the range of −20 to +15 dB) at the surface. Further, although the Ka-band radar is of higher frequency than those used in the Viking, Pathfinder, Mars Exploration Rovers, and Phoenix missions, we have also shown that the radar is impervious to any physical realizable amount of dust that can be lofted during landing.

To validate these assumptions and general radar performance, a field test campaign was executed to test the TDS across the entire MSL EDL flight envelope. Nineteen flights of an F/A-18 aircraft using a single TDS antenna in a wing-mounted pod were conducted to test the parachute and descent phases. The F/A-18 performed steep dives from −45° to −90° flight path angles at altitudes ranging from 14 km to 2 km above the ground at Rogers Dry Lake and the southern Sierra Nevada foothills. Late acquisition and powered descent EDL phases were tested using an A-STAR A350BA helicopter. With the six-antenna TDS installed on a nose-mounted gimbal, the helicopter performed powered-descent-like trajectories from 3 km above the ground to the surface during 37 flights over Rogers Dry Lake, Amboy Crater, Cadiz Sand Dunes, and Death Valley. Finally, the sky crane descent was tested in detail at the Echo Towers at China Lake, CA. All of the above tests have shown that there are no radar-related constraints on the landing site selection (other than being radar reflective), and that the radar will perform as designed at Mars.

Broad tracts of Mars have very low thermal inertia and high albedo and have been interpreted to be surfaces dominated by loose dust that could be meters thick (e.g., Christensen and Moore 1992; Mellon et al. 2008). Experience and extrapolation from the existing landing sites argues that loose dusty material is not load bearing (e.g., Christensen and Moore 1992; Golombek et al. 2008b). In addition, radar reflectivity is related to the bulk density of dry materials, so areas with low radar reflectivities might have surfaces with low bulk density (e.g., see Golombek et al. 1997a and references and discussion therein). Global thermal inertia and albedo data show a mode with thermal inertias less than 100 $\mathrm{J\,m^{-2}\,s^{-0.5}\,K^{-1}}$ and albedo higher than 0.25 that corresponds with these very dusty surfaces (Putzig et al. 2005; Mellon et al. 2008) that could be meters (Christensen and Moore 1992) to tens of meters thick (Mangold et al. 2009). Surfaces with these characteristics are not suitable for landing spacecraft or driving rovers (e.g., Golombek et al. 1997a, 2003a) and the dust would curtail science operations. Large temperature extremes at low thermal inertia, high albedo sites would also reduce surface operations through the diversion of available energy to rover thermal maintenance (see Sect. 2.2.2).

3 Planetary Protection

In accordance with international agreements, NASA places requirements on spacecraft in order to prevent the forward contamination of Mars while exploration of its biology and organic chemistry are ongoing. These requirements prescribe the cleanliness of a spacecraft in relation to its mission and science goals (e.g., *in situ* sampling, life detection, sample return, etc.) and landing site. The latter is a factor because some regions of Mars are more at risk than others, with a higher likelihood that terrestrial organisms may propagate or a higher potential for extant Martian life forms, primarily due to the presence of water (MEPAG et al. 2006).

It was recognized early in the MSL mission's formulation that the rover's physically hot radioisotope thermoelectric generator power source, if as a result of a crash becomes embedded in water-rich ground along with terrestrial microbes on spacecraft hardware, could potentially create an environment favorable to the propagation of microbes. Attempts were made to simulate this scenario (Hecht and Vasavada 2006) and quantify the probability of significant microbial propagation, but propagation could not be ruled out with confidence. The NASA Planetary Protection Office determined in August 2005 that MSL was categorized as a IVc mission (as defined by the Committee on Space Research of the International Council of Science) with two options for implementation: (i) perform a full-spacecraft sterilization with no restriction on landing site, or (ii) clean the spacecraft to a lesser degree but

accept a restriction that one-sigma landing ellipses that address failure modes subsequent to parachute opening be limited to regions not known to have extant water or water ice within 1 m of the surface.

After a cost analysis of the first option, the Project chose the second. Based on theoretical models and observations by the Mars Odyssey Gamma Ray Spectrometer (e.g., Mellon et al. 2004), a latitude limit of ±45° was chosen to exclude the possibility of ground ice within 1 m of typical flat surfaces. More recently, the Project determined that no other evidence for extant water or water ice exists at the four final candidate sites, e.g., radar ice signatures, gully morphologies, glacial, periglacial or lobate morphologies, icy mantles, thermal inertia anomalies, or significant areas covered by steep, poleward-facing slopes that could create low-latitude niches for ground ice (Vincendon et al. 2010). Water frost and adsorbed water in equilibrium with atmospheric humidity are possible at the MSL sites but are not considered relevant to the Planetary Protection concern.

4 Science Objectives

The Mars Science Laboratory mission was designed to explore a local region on Mars and to quantitatively assess past and present habitability and environmental conditions (Grotzinger et al. this issue). Assessment of present habitability (i.e., the ability to support life as we know it) requires an evaluation of the characteristics of the environment and the processes that influence it from microscopic to regional scales, and a comparison of those characteristics with what is known about the capacity of life to exist in such environments. Determination of past habitability has the added requirement of inferring environments and processes in the past from observation in the present, including the potential of the site to preserve evidence related to habitability (Summons et al. 2011). Such assessments require the integration of a wide variety of chemical, physical, and geological observations. These objectives were translated into specific criteria (diversity, context, habitability and fossil/biosignature preservation) for evaluating and prioritizing prospective landing sites during the third landing site workshop (see Sect. 7.7). Compared with recent missions that have been targeted to find evidence for past or present water, the task of searching for habitable environments is significantly more challenging (Grotzinger 2009).

The MSL mission has four primary science objectives to meet the overall habitability assessment goal (Grotzinger et al. this issue). The first is to assess the biological potential of at least one target environment by determining the nature and inventory of organic carbon compounds, searching for the chemical building blocks of life, and identifying features that may record the actions of biologically relevant processes. The second objective is to characterize the geology of the landing region at all appropriate spatial scales by investigating the chemical, isotopic, and mineralogical composition of surface and near-surface materials, and interpreting the processes that have formed rocks and soils. The third objective is to investigate planetary processes of relevance to past habitability (including the role of water) by assessing the long timescale evolution of the atmosphere and determining the present state, distribution, and cycling of water and CO_2. The fourth objective is to characterize the broad spectrum of surface radiation, including ultraviolet light, galactic cosmic radiation, solar proton events, and secondary neutrons.

While MSL is not designed to directly detect present-day life processes or to image microorganisms or their fossils, it does have the capability to detect complex organic molecules in rocks and soils (Grotzinger et al. this issue). If detected, a further goal would be to distinguish a Martian origin versus delivery by carbonaceous meteorites. MSL will study less

unique biosignatures as well, such as the isotopic composition of inorganic and organic carbon in rocks and soils, particular elemental and mineralogical concentrations and abundances, and unusual rock textures. The rover also can sample atmospheric gases directly, measuring the concentration and isotopic composition of potentially biogenic atmospheric species such as methane.

5 Data and Models Used to Evaluate Surface Characteristics

5.1 Introduction

Data available to select and certify landing sites on Mars has varied widely for each of the landed missions, but have included visible images at ever increasing resolution, visible to thermal infrared multispectral images, thermal images, thermal inertia and albedo, radar data, and altimeter data to infer elevation and slopes. Golombek et al. (2003a, 2008b) summarizes the data used for landing site selection efforts through MER. The Viking landing site selection activity relied mostly on Mariner 9 information prior to arrival and then an intense effort to find new sites after arrival when previously identified sites appeared too dangerous in Viking orbiter images (Masursky and Crabill 1976a, 1976b, 1981). Although Mars Pathfinder had little new data since Viking, there was a much greater appreciation and models of how the Viking Lander 1 (VL1) and Viking Lander 2 (VL2) landing surfaces related to Viking Orbiter data and a clear Earth analog (Golombek et al. 1997a) that correctly predicted the surface characteristics of the landing site (Golombek et al. 1997b, 1999). The MER landing site selection effort benefited greatly from new and much higher resolution information from MGS and Odyssey that resulted in well characterized sites that matched predictions from orbital data (Golombek et al. 2003a, 2005). The Phoenix landing site selection relied on data from MGS and Odyssey (particularly Thermal Emission Imaging System, THEMIS nighttime thermal images, Christensen et al. 2004) until MRO began its nominal mission. The landing site was well imaged by HiRISE, thus becoming the first site that was well characterized at the scale of the lander (Arvidson et al. 2008) and was exactly what was expected from orbital data. The data acquired and processed for the MSL landing sites have set a new standard for characterizing the surface from orbit with effectively complete stereo HiRISE, CTX and CRISM coverage of the landing ellipses and "go to" areas. These data have directly measured most of the landing hazards and allowed a fairly complete understanding of their trafficability.

5.2 Image Data

Images of Mars used in previous site selection efforts include a wide variety of data from multiple spacecraft: (1) Mariner 9 images (many hundreds of meters per pixel); (2) Viking Orbiter images (tens of meters to hundreds of meters per pixel; global mosaic at 230 m/pixel); (3) MGS/MOC high-resolution images (several meters per pixel; Malin and Edgett 2001a); and (4) Mars Odyssey THEMIS 100 m/pixel thermal and 18 m/pixel visible images (Christensen et al. 2004). Images from (1) and (2) factored into the site selection for the Viking landers; MPF site selection dominantly used images from (2) and MER site selection used images from (2) to (4). MER slopes at the scale of a lander or rover (1–3 m) were evaluated using MOC stereo derived Digital Elevation Models (DEMs) and photoclinometery (or shape from shading; Beyer et al. 2003; Kirk et al. 2003). Phoenix was the first to use HiRISE data at 0.3 m/pixel from MRO, which

allowed the direct measurement of large rocks on the surface (Golombek et al. 2008a). HiRISE stereo pairs were also processed to make 1 m posting DEMs for several locations within the Phoenix landing ellipse (Kirk et al. 2008).

MSL profited from the complete suite of MRO imaging instruments and landing sites and "go to" areas had almost complete stereo HiRISE images (6 km wide) that were made into "wall to wall" 1 m elevation posting DEMs using stereogrammetry and photoclinometry (Kirk et al. 2011a, 2011b; Beyer and Kirk this issue). The sites also have complete coverage of stereo CTX images (30 km by 30 km) at about 6 m/pixel (Malin et al. 2007) and essentially complete visible to near infrared multispectral (512 bands) CRISM images (10 km by 10 km) coverage at 18 m/pixel (Murchie et al. 2007). The HiRISE images have been used to directly measure the large rocks and characterize the rock size-frequency distribution over all of the sites (Golombek et al. 2011a, 2012). Finally, multiple orbit HRSC stereo images (orthophoto image at 12.5 m/pixel) have been made into DEMs with 50 m elevation postings at all of the landings sites (Gwinner et al. 2009, 2010a, 2010b).

5.3 Altimetry Data

MGS Mars Orbiter Laser Altimeter (MOLA) data have provided definitive global elevation information (Smith et al. 2001) that, when combined with gravity data, has defined the geoid and its relationship with atmospheric pressure (Smith and Zuber 1998). MOLA data also allow evaluation of the long baseline slopes (~1 km) that are important for the airbag-encased landers (MPF and MER) as well as slopes on the hundreds of meters scale (Anderson et al. 2003) that are important for landing radar system performance. The returned spread of the MOLA laser pulse also provided a measure of the roughness within each ~75 m laser surface spot (Neumann et al. 2003). Gridded MOLA elevation data were also used to make shaded relief maps (Smith et al. 2001).

5.4 Thermophysical Properties

Thermophysical properties have been an important discriminator of potential landing sites and a tool for global extrapolation of what we learn at each landing site, because thermal inertia measurements (a composite of thermal conductivity, bulk density and heat capacity, and a measure of the resistance of surface materials to changes in temperature over the upper few thermal skin depths of ~2–30 centimeters) can be related to particle size, bulk density, and cohesion. Bulk thermal inertia observations of Mars used in landing site selection studies include values derived from: (1) Viking Infrared Thermal Mapper (IRTM) data at ~60 km per pixel (Kieffer et al. 1977; Palluconi and Kieffer 1981), (2) MGS Thermal Emission Spectrometer (TES) data (Christensen et al. 1992) at 8 pixels per degree (Mellon et al. 2000; Christensen et al. 2001) and at 20 pixels per degree (Putzig et al. 2005; Putzig and Mellon 2007), and (3) Mars Odyssey THEMIS data at ~100 m/pixel (Christensen et al. 2004; Fergason et al. 2006a; Fergason et al. this issue). Supervised classification of THEMIS thermal inertia data by comparing to surface materials in HiRISE images also yields surface material maps (Fergason et al. this issue) used for rover traversability studies.

The contrast between measurements of thermal emission from the surface at different wavelengths using IRTM and TES data have been used to determine the rock abundance (the fractional area covered by high thermal inertia rocky material) at about 60 and 8 km/pixel scales (Christensen 1986a; Nowicki and Christensen 2007). With the rock abundance and the bulk thermal inertia, the thermal inertia of the remaining soil, referred to as the fine-component thermal inertia (Kieffer et al. 1977), has also been determined (Christensen

1986a; Nowicki and Christensen 2007). The Lambert albedo (the brightness of reflected solar energy from the surface in which the viewing geometry has been taken into account) was also available as measured by both IRTM and TES at 1 pixel and 8 pixels per degree, respectively (e.g., Pleskot and Miner 1981; Christensen et al. 2001). The albedo can, for example, be used to infer the dustiness of the surface, as very dusty areas exhibit very high albedo (and, in addition, very low-thermal inertia). The amount of dust cover at the landing sites was also evaluated using the TES dust cover index (16 pixels per degree), which includes a more explicit measure of the particle size and the amount of dust coating the surface (Ruff and Christensen 2002).

5.5 Radar Data

Radar data have been used to infer surface roughness at the scale of the radar wavelength (diffuse scattering), as well as at 10–100 times the radar wavelength (specular reflection; Simpson et al. 1992; Haldemann et al. 1997; Harmon et al. 1999; Larsen et al. 2010). The interpretation of radar data for previous landing sites is summarized in Golombek et al. (2008b). Specular and diffuse radar data are available at 3.5 cm wavelength for many equatorial areas and some 12.6 cm data also exist. Root mean square (RMS) slopes at the 10–100 times radar wavelength scale compare favorably with those determined from MOC images. Slopes at the scale of the lander are important for evaluating lander stability and rover traversability. Radar reflectivity is important for the radar altimeter on a lander to accurately measure the descent of the spacecraft. Radar reflectivity can be related to the bulk density of the surface materials, which can be used to infer whether the surface is load bearing and trafficable (Golombek et al. 1997a).

5.6 Georegistration of Data Sets

MSL landing site base maps were produced by georegistering progressively lower to higher resolution images for establishing the best horizontal and vertical geodetic control possible for EDL Monte Carlo simulations, traverse analysis, and future tactical and strategic planning during operations. This is similar to Kim and Muller's (2009) "hierarchical co-registration technique" using pyramidal georegistration of progressively higher resolution images and is the same process used for MER (Golombek et al. 2003a). Using a geographic information system (ArcGIS), DEMs and visible images were coregistered and mosaiced from four principle sources: MGS MOLA (Smith et al. 2001), Mars Express HRSC, MRO CTX 6 m/pixel images (Malin et al. 2007), and the MRO HIRISE 0.25 m/pixel images (McEwen et al. 2007). Gridded MOLA data served as the base reference elevation dataset at ~0.5 km/pixel and are in a positive east planetocentric coordinate system referenced to the IAU/IAG 2000 frame, which can be easily converted to the inertia coordinates used by the spacecraft navigation team (e.g., Golombek et al. 2003a). All products were prepared in an equirectangular (aka equidistant cylindrical) projection with a central longitude and central latitude of zero, with units in meters relative to the Mars central meridian, on a sphere with radius 3,396,190 m. Because each landing site is relatively close to the equator, the amount of distortion introduced was considered minimal (three of the sites are ~25° poleward from the equator, while Gale is only ~4°). HRSC DEMs at 50 m/pixel created from images taken over multiple orbits (Gwinner et al. 2009, 2010a, 2010b) are controlled to MOLA as part of their production process, resulting in excellent three-dimensional registration to MOLA, and most are accompanied by an orthorectified 12.5–25 m/pixel panchromatic visible image (Gwinner et al. 2007) that is (by definition) georeferenced to the DEMs. Next, 6 m/pixel

low-emission angle, CTX images were georegistered to the HRSC images, with one base CTX for each landing site, then, where necessary, a second or third CTX "wing" image was referenced to the east or west. Finally, each HiRISE orthophoto was georeferenced to the CTX rectified image base.

All HiRISE images used were orthorectified in the map projection described above, based on the DEM constructed from the stereopair of which they were a part. These DEMs and orthoimages were individually controlled to MOLA as part of the production process, but because of the low resolution of the gridded altimetry file, the products did not align to one another at the HiRISE or even the CTX pixel scale. The orthoimages were therefore co-registered at higher precision via manual selection of a horizontally homogenous collection of 20–100 "tie" (i.e., ground control) points per image. Each image and its associated DEM were adjusted (typically by ∼100 m or less) in map coordinates based on spline interpolation of the tie point locations. To maintain geodetic control, tie point locations from registering CTX to HRSC were used as the initial HiRISE to CTX tie points, allowing horizontal connection to the HRSC (albeit, this was only a handful of points per HiRISE). Where subsequent HiRISE orthophotos overlapped, extra tie points in intersecting areas were captured to ensure horizontal registration and edge matching between the highest resolution images.

Once all HiRISE images were georeferenced, additional data products including delta radii elevations (elevation relative to the spheroid, as opposed to the geoid), geoid elevations, traverse hazards, and other rock hazard maps were rectified using the same tie points for each orthophoto. Table 4 shows the HiRISE image pairs used to create the DEMs, slope maps, rock maps, and traverse maps described in Sect. 9. These data products cover 80–85 % of the landing ellipses at the time of site selection. Rectified delta radii files were sent to the U.S. Geological Survey Astrogeology Research Program along with overlapping sections of CTX and HRSC DEMs converted to delta radii (by subtracting the MOLA geoid) for "equalization" and incorporation into a unified delta radii mosaic (Kirk et al. 2011a, 2011b) to be used for EDL simulations (Sect. 9.5.1). Other rock and traverse hazard maps were mosaiced and increased to 1 m/pixel cell size using a nearest neighbor algorithm to keep interpolation to a minimum. Most other global datasets used in this work, such as global TES thermal inertia and albedo, global day and nighttime THEMIS images (and global mosaic), and 100 m/pixel THEMIS thermal inertia data were produced in the same MOLA positive east planetocentric coordinate system referenced to the IAU/IAG 2000 frame. THEMIS thermal inertia maps produced by Fergason et al. (this issue) were georeferenced to the rectified CTX basemap to develop the material property maps.

6 Atmosphere Definition

The atmosphere is a key constraint on where a spacecraft can land on Mars, because the entry vehicle and parachute use the atmosphere to slow the lander. The dominant parameter is atmospheric density, or perhaps more accurately, the integrated stopping power of the atmosphere above any particular site given its elevation and the details of the entry, descent and landing (EDL) system. As described in Sect. 2.1, the initial elevation design goal of +2.5 km was chosen to allow access to more of Mars' surface, but was relaxed over time as the list of candidate sites narrowed. Other characteristics that affect the performance of the EDL system are density variability and wind (magnitude, direction, and variability over a range of length and temporal scales). The various stages of EDL such as encapsulated flight, parachute deployment, parachute descent, and powered descent, all have different vulnerabilities to these parameters, so each must be evaluated at the relevant altitude and horizontal

Table 4 HiRISE stereo pairs and images* used to make DEMs, orthophotos, rock maps, terrain classification, and traversabilty maps

Eberswalde Crater	Gale Crater	Holden Crater	Mawrth Vallis
PSP_008272_1560	PSP_009149_1750	PSP_002088_1530	PSP_005964_2045*
PSP_010474_1560*	PSP_009294_1750*	PSP_002154_1530*	ESP_011884_2045
PSP_010052_1560*	PSP_009505_1755*	PSP_007191_1535*	PSP_006676_2045*
PSP_010553_1560	PSP_009571_1755	PSP_007903_1535	PSP_007612_2045
ESP_011265_1560	PSP_009650_1755	PSP_010540_1535	PSP_008469_2040*
ESP_011331_1560*	PSP_009716_1755*	PSP_010685_1535*	PSP_008825_2040
ESP_016065_1560	PSP_010573_1755*	ESP_015999_1535	PSP_010816_2040*
ESP_016210_1560*	PSP_010639_1755	ESP_016276_1535*	PSP_010882_2040
ESP_019190_1560*	ESP_011417_1755	ESP_019045_1530*	ESP_015985_2040
ESP_019335_1560	ESP_011562_1755*	ESP_019322_1530	ESP_016262_2040*
ESP_019757_1560*	ESP_018854_1755*	ESP_019612_1535*	
ESP_020034_1560	ESP_018920_1755	ESP_019678_1535	
ESP_020324_1555*	PSP_001488_1750+	ESP_019823_1530*	
ESP_020390_1555	PSP_001752_1750	ESP_019889_1530	
	ESP_012551_1750+		
	ESP_012841_1750		
	ESP_019698_1750+		
	ESP_019988_1750		
	ESP_024234_1755+		
	ESP_024300_1755		
	ESP_023957_1755+		
	ESP_024023_1755		
	ESP_024102_1755+		
	ESP_025368_1755		
	ESP_025790_1750+		
	ESP_027135_1755		

Images with an asterisk and DEMs created with these images were produced prior to selection and denote those used for computing slope statistics, rock lists (and their derived products: rock abundance, cumulative fractional area, and "additional strikes") and were used for all landing simulations and traversability analyses and are depicted in Figs. 9, 12a, c, d, 13, 15, 16, and 21a, c, d. Images with a plus sign for Gale denote those images acquired or processed after selection and made into DEMs and orthophotos only for post-selection EDL, traverse planning, and science and are depicted in Figs. 12b and 21b

range from the landing target. In the early stages of site selection, a list of acceptable values was developed by the EDL team and distributed to the science community, who used it to vet potential sites by examining existing orbital and model data sets. Certain sites were determined to have increased risk based on their high elevation or their proximity to topography (e.g., regional-scale features such as Syrtis or local canyons or crater walls) that induced strong winds or wind shear.

Once a smaller set of candidate sites was defined, the MSL Project chartered a working group composed of EDL engineers and external atmospheric scientists (Council of Atmospheres) to define the atmospheric characteristics and their uncertainties at each site using high-resolution numerical models, and to prepare those results in a format that could be fed directly into EDL simulations (Vasavada et al. this issue). The results of these Monte Carlo simulations form the basis for validating the EDL approach and certifying the safety of landing sites. In addition, the group gathered detailed historical statistics of dust storms and

other weather events that could cause rare but significant deviations from mean conditions, and ran additional simulations against these anomalous conditions.

Atmospheric predictions for MSL are derived from numerical models with roughly kilometer spatial resolution (Rafkin et al. 2001; Tyler et al. 2002), compared with tens or hundreds of kilometer resolution at the time of Viking or Mars Pathfinder. The accuracy of the models has improved by including the high-resolution maps of topography (Smith et al. 2001), albedo, and thermal inertia from Mars Global Surveyor (Christensen et al. 2001; Mellon et al. 2008). The models were constrained by and validated against data sets from orbital imaging and sounding (thermal and radio) instruments, which were substantially improved over earlier mission atmospheric characterization efforts by the long history of TES and THEMIS thermal observations (Smith 2004) and the Mars Climate Sounder (MCS) on MRO (Kleinbohl et al. 2009). Finally, the assessment of risk from atypical conditions has been improved by the observational record of dust events over wide spatial and temporals scales from the wide-angle cameras on MGS (Cantor et al. 2001) and MRO.

As an input to the final site selection activities in Summer 2011, the Council of Atmospheres concluded that the final four candidate sites present acceptable risk from an atmospheric perspective, and furthermore, that the distinctions in risk level between the sites were not significant. The evaluation of atmospheric characteristics and risk are described more fully in Vasavada et al. (this issue).

7 Landing Site Downselection

This section provides a historical summary of the landing site selection process through each of the major community workshops, project meetings and steering committee teleconferences. We briefly describe the science and safety of candidate landing sites where necessary to explain the attributes of the sites that led to their ranking and downselection. We cite the published literature where available, but a complete record of the presentations and discussions at each workshop, summary letters, and downselection decisions can be found on the marsoweb and USGS web sites to which the reader is referred for additional information: http://marsoweb.nas.nasa.gov/landingsites/ and http://webgis.wr.usgs.gov/msl/index.htm. With regard to the spectral identification of hydrous minerals cited below, we use the nomenclature of the referenced source and note that phyllosilicates are sheet silicates that include clays (hydrous aluminum phyllosilicates), serpentine (hydrous magnesium phyllosilicates) and smectites (dioctohedral and trioctohedral clays).

7.1 First Landing Site Workshop

The First Mars Science Laboratory Landing Site Workshop was held May 31–June 2, 2006. The purpose of the workshop was to identify and evaluate potential landing sites best suited to achieving mission science objectives within the constraints imposed by engineering and planetary protection requirements and the necessity of ensuring a safe landing. The workshop was held prior to MRO getting into mapping orbit so that a list of potential landing sites would be available as soon as imaging began. Engineering constraints allowed the consideration of an enormous number of landing sites over $\sim$70 % of Mars because of the small landing ellipse (20 by 25 km), and broad latitude ($\pm 60°$) and high elevation ($+2$ km) constraints (Golombek et al. 2006a). Another unique aspect of the MSL mission is the possibility of "go to" sites, for which the rover would be expected to traverse outside of its landing ellipse to access the primary science target.

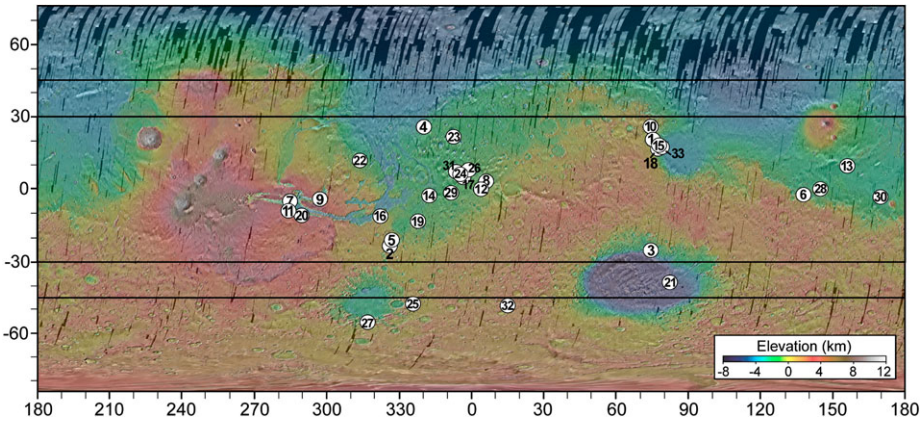

Fig. 2 THEMIS daytime thermal image mosaic overlain on MOLA topographic map of Mars showing location of landing sites proposed for the Mars Science Laboratory at the first workshop (numbered in order of prioritization, Table 5). Revised engineering constraints later restricted landing sites to ±45° latitude and finally ±30°

The workshop was well attended with about 100 participants that included Principal and Co-Investigators from MSL, Principal and Co-investigators from major orbiter instruments that were being used to image the sites, and many scientists unaffiliated with MSL, which highlights the Mars community's interest in MSL landing site activities (Golombek et al. 2007a, 2007a). A wide variety of sites were proposed at the workshop. A total of 33 general sites were proposed that incorporated 94 landing ellipses (multiple ellipses were proposed for some sites) that span a considerable range of latitudes and elevations on Mars (Fig. 2, Table 5). Most landing sites were proposed based on morphology (e.g., layered or deltaic deposits) or mineralogy (e.g., sulfates or phyllosilicates from OMEGA, Observatoire pour la Mineralogie, l'Eau, les Glaces, et l'Activite; Bibring et al. 2005) or both indicative of aqueous processes. In addition to the landing site presentations, there was substantial discussion of their merits and a vote by workshop participants to prioritize the sites based on their science potential and safety for subsequent imaging. Sites prioritized in the top third (Table 5) include three characterized by phyllosilicate signatures (Nili Fossae, Mawrth Vallis and Nilo Syrtis), two characterized by sulfate signatures (W. Candor and Juventae Chasma), with the rest characterized by layered deposits of likely or proposed aqueous origin. Most, but not all of the highest ranked two thirds of the sites were "go to" sites that have a safe landing site adjacent to the target of science interest that require traversing outside of the landing ellipse to sample the materials of highest interest.

The sites farthest north and south were at 23°N and 57°S, respectively, with all of the sites ranked in the top 50 % falling between 23°N and 28°S. By contrast, all of the sites lie between +1 km and −4.5 km elevation with all of the sites ranked in the top 50 % falling below −0.4 km. Of these, only one proposed site is located at an elevation above 0 km.

Following the workshop the Mars Science Laboratory Project conducted a complete review of the entry, descent and landing system and concluded that substantial savings in timeline and testing (and budget) could be realized if the elevation constraints were reduced to less than +1.0 km and thermal design and communications could be simplified if the latitude constraints were reduced to ±45°. NASA Headquarters approved these changes so that landing sites under consideration must meet these new constraints. Other engineering constraints remained unchanged except for the addition of a requirement that the slope over

Table 5 Landing sites prioritized in thirds (1–11, 12–23, 24–33) at first MSL workshop

Name	Location	Elevation	Target	Proposer
1. Nili Fossae Trough	20.93°N, 74.35°E	−0.6 km	Phyllosilicates	J. Mustard
2. Holden Crater Fan	26.32°S, 325.30°E	−2.3 km	Layered Materials	Irwin, Grant, Malin, Edgett, Rice
3. Terby Crater	27.74°S, 74.11°E	−5 km	Layered Material	S. Wilson, Cohen, Dobrea
4. Marwth Vallis	24.65°N, 340.1°E	∼ −3.1 km	Phyllosilicates	J.-P. Bibring, J. Michalski
5. Eberswalde Crater	23.19°S, 326.75°E	−0.8–0.4 km	Delta	J. Schieber, J. Dickson, J. Rice
6. Gale Crater	4.50°S, 137.35°E	−4.5 km	Interior Layered Deposits	J. Bell, N. Bridges
7. W Candor	5.80°S, 284.17°E	−4 km	Sulfate Deposits	N. Mangold
8. N Meridiani	2.37°N, 6.69°E	−1.5	Sedimentary Layers	Edgett/Malin
9. Juventae Chasma	4.45°S, 298.09°E	−2.8 km	Layered Sulfates	J. Grotzinger
10. Nilo Syrtis	29.16°N, 72.97°E	∼ −0.5	Phyllosilicates	J. Mustard
11. Melas Chasma	9.81°S, 283.62°E	−1.9 km	Paleolake	C. Quantin
12. E. Meridiani	0.01N°, 3.66° E	∼ −1.3 km	Sedimentary Layers	B. Hynek
13. Athabasca Vallis	9.93N, 156.77°E	−2.4 km	Cerberus Rupes Deposits	D. Burr
14. Iani Chaos	2.06°S, 342.41°E	< −2 km	Hematite, Sulfate	T. Glotch
15. Nili Fossae Crater	18.44°N, 77.58°E	−2.6 km	Valley Networks, Delta sediments	R. Harvey, J. Rice
16. Eos Chasma	10.7°S, 322.05°E	∼ −4 km	Chert	V. Hamilton
17. Meridiani Crater Lake	5.72°N, 358.03°E	∼ −1.5 km	Crater lake sediments	L. Posiolova
18. NE Syrtis Major	16.21°N, 76.63°E	∼1 km	Volcanics	R. Harvey
19. Margaritifer basin	12.85°S, 338.0°E	−2.12 km	Fluvial Deposits	K. Williams
20. E. Melas Chasma	11.72°S, 290.72°E	< −2 km	Interior Layered Deposits	M. Chojnacki
21. Hellas/Dao Vallis	39.5°S, 82,7°E	−6 km	Valley Terminus, Layered Deposits	L. Crumpler
22. Xanthe/Hypanis Vallis	11.4°N, 314.65°E	−2.6 km	Layered Deposits	L. Crumpler
23. Becquerel Crater	21.32°N, 352.52°E	−2.6–3.8 km	Layered Sedimentary Rocks	J.C. Bridges
24. SW Arabia Terra	6.01°N, 355.60°E	−1 km	Sed. Rocks, Methane	C. Allen
25. Gullies/Wirtz Crater	48.48°S, 335.05°E	−2.4 km	Gullies	W.E. Dietrich
26. W. Arabia Crater	8.45°N, 359.09°E	−1.2 km	Sedimentary Rocks	E. Heydari
27. Argyre	56.8°S, 317.7°E	−1.5 km	Glacial Features	J. Kargel
28. NW Slope Valleys	∼0, 145°E	∼ −2 km	Flood Features	J. Dohm
29. W. Meridiani	1.7°S, 352.39°E	∼ −1.0–1.5 km	Sediments, Hematite	H. Newsom
30. Elysium/Avernus Colles	3.05°S, 170.60°E	−2.5 km	High iron abundance	L. Crumpler
31. Meridiani Bench	7.5°N, 354°E	∼ −1–1.5 km	Layered Sediments	A. Howard
32. SML Craters	49.04°S, 14.494°E	> −0.5 km	Recent Climate Deposits	M. Kreslavsky
33. Isidis Basin Escarpment	18.00°N, 79.60°E	−3.5 km	Volatile sink	L. Crumpler

200–500 m length scale be $\leq 5°$ to avoid altimetry errors in preparation for the sky-crane landing maneuver (Golombek et al. 2007a).

7.2 Remote Sensing of Landing Sites

Of the 33 sites proposed and prioritized at the first workshop, 30 were defined and targeted by remote sensing assets. MRO data were collected at the rate of ∼3–5 targets per two week imaging cycle and required careful targeting (typically in coordination with the person proposing the site) of the location and distribution within proposed ellipses to maximize the ability to assess science and surface characteristics. The opportunity to target and quickly receive MRO images became a powerful incentive to participate in the site selection process for those not involved on MRO science teams.

For each landing site proposed, a single 20 by 25 km ellipse was defined that appears smooth and flat. In addition, a Region of Interest (ROI) was defined that includes the landing ellipse and if it was a "go to" site, the area of prime science interest for the rover to explore. Finally, each site included the location of the preferred HiRISE image for the standard survey images that were being acquired by MRO. The standard MRO survey images for MSL landing sites were a collocated set composed of: 6 km wide by 10 km long (or longer) HiRISE image at 0.3 m/pixel; 10 km by 10 km CRISM image at 18 m/pixel (512 bands); 30 km by 30 km CTX (Context Imager) image at 6 m/pixel. These locations were input into HiRISE targeting software and provided to the rest of the MRO instruments. The locations were also submitted to other orbiting imaging assets including Mars Global Surveyor, Mars Odyssey, and Mars Express (Golombek et al. 2007b).

7.3 Second Landing Site Workshop

Presentations at the Second Landing Site Workshop on October 23–25, 2007 included updates on previously proposed sites and on new sites based on discoveries from interpretation of MRO data (over 30 sites that included a total of 51 ellipses across much of mid- and low-latitude Mars; Golombek et al. 2008c). The goal of the workshop was to trim the number of landing sites under consideration to approximately five. All sites presented were discussed and voted on by workshop participants to determine the subset that the science community felt best satisfied the MSL science objectives while meeting basic safety and accessibility criteria. Subsequent discussion attempted to pare the top sites while maintaining a diversity of science characteristics and level of risk. Possible "safe haven" sites (with larger ellipses at lower elevation) and "latitude bands" (defined by northern and southern latitudes important for mission design for targeting and communication during entry, descent and landing) for the landing sites were also discussed as factors that might impact mission operations and performance.

Based on the presentations and discussions, voting revealed the 11 highest priority sites based on science were: Nili Fossae trough (21°N, 74°E), NE Syrtis (16°N, 77°E), Jezero crater (18°N, 78°E), Holden crater (26°S, 325°E), Eberswalde crater (23°S, 327°E), Miyamoto crater (referred to as Runcorn crater or E and S Meridiani at the workshop) (3°S, 353°E), Chloride sites (12°S, 345°E; 18°S, 3°E), E Meridiani (0°N, 4°E), Mawrth Vallis (close to 25°N, 340°E), Terby crater (28°S, 74°E), and Melas Chasma (10°S, 284°E). Collectively, these sites represent a range of inferred depositional settings deemed highly relevant to the science objectives of MSL and each is briefly summarized from descriptions presented in Grant et al. (2010a).

The Nili Fossae ellipse is characterized by alteration minerals and carbonates (Mustard et al. 2008, 2010; Poulet et al. 2005) and provides access to altered and unaltered Noachian

crustal materials west of the ellipse and impact ejecta and Hesperian volcanic materials in the ellipse. Accessible rocks may have formed in a variety of environments including hydrothermal, alluvial/fluvial, and shallow crust/pedogenic settings (Ehlmann et al. 2010; Mangold et al. 2007; Michalski et al. 2010a; Mustard et al. 2008, 2010).

The ellipse in NE Syrtis Major is located on the northern margin of the Syrtis Major volcanic complex and a northward traverse would provide access to volcanic and then distinct, diverse units exposing Hesperian and Noachian-aged sequences with hydrated and phyllosilicate mineral signatures (Bibring et al. 2005, 2006; Ehlmann et al. 2010; Mustard et al. 2008, 2010; Poulet et al. 2007).

In Jezero crater, the ellipse is on likely volcanic materials filling the crater floor and east of phyllosilicate-bearing, late-Noachian fluvial fan deposits (Ehlmann et al. 2008a; Fassett and Head 2005). The watershed for the input valleys would have likely transported diverse altered materials from eroded Noachian-aged crust to the west (Ehlmann et al. 2008a).

Holden and Eberswalde craters are located in the ancient terrain of southern Margaritifer Terra (Scott and Tanaka 1986; Fig. 3). The ellipse in Holden crater is located on a broad alluvial bajada flanking portions of the wall (Moore and Howard 2005; Pondrelli et al. 2005), whereas the ellipse in Eberswalde crater lies on the crater floor. Both Holden and Eberswalde craters are probably no older than Hesperian in age (Irwin and Grant 2011) and contain distinctive alluvial fan/deltaic and lacustrine deposits (e.g., Grant et al. 2008; Moore et al. 2003). The fan and delta deposits in both craters were likely emplaced around the time of the Amazonian to Hesperian transition or even later (Grant and Wilson 2011), whereas the putative lake deposits in Holden which form the prime target for MSL may date to earlier in the Hesperian (Grant et al. 2008; Irwin and Grant 2011). The delta on the western wall of Eberswalde (Lewis and Aharonson 2006; Malin and Edgett 2003; Moore et al. 2003) was likely deposited into a lake within the crater over a period ranging from decades (Jerolmack et al. 2004) to more than a hundred thousand years (Bhattacharya et al. 2005). The deposits in Holden and Eberswalde both coincide with phyllosilicate mineral enrichments (Grant et al. 2008; Milliken et al. 2008; Milliken and Bish 2010), which points to accumulation in a standing body of water (Grant and Parker 2002; Grant et al. 2008; Malin and Edgett 2000; Pondrelli et al. 2005, 2008).

The ellipse in western Miyamoto crater targets a series of raised curvilinear ridges and other, sometimes phyllosilicate-bearing features and deposits inferred to represent late-Noachian inverted fluvial deposits (Newsom et al. 2010). These deposits are distributed in a patchwork fashion amongst other, younger materials of less certain origin and are located west of layered sulfate and hematite-bearing deposits forming Meridiani Planum (Arvidson et al. 2006; Squyres et al. 2006).

An ellipse associated with the chloride site south of Meridiani Planum provides access to a small basin near the terminus of a valley network where putative chloride deposits have been identified (Osterloo et al. 2008, 2010). The chloride deposits, inferred to have formed via in situ precipitation within a sedimentary sequence, would have required substantial water prior to their emplacement and could comprise a good setting for preservation of any organic materials (Osterloo et al. 2008, 2010).

The ellipse for the East Meridiani landing site is approximately 600 km northeast of the Mars Exploration Rover Opportunity landing site in Meridiani Planum. The site includes a sequence of sulfate and hydrated mineral bearing layers that likely record ancient aqueous depositional and/or alteration settings good for the preservation of organics and biosignatures (Hynek and Phillips 2008; Hynek et al. 2002; Poulet et al. 2008a).

The ellipse in Melas Chasma is within a basin on the southern wall of the chasmata (Quantin et al. 2005) and covers layered sedimentary beds deposited in a postulated paleolake that was fed by tributaries of Hesperian age (Dromart et al. 2007; Metz et al. 2009;

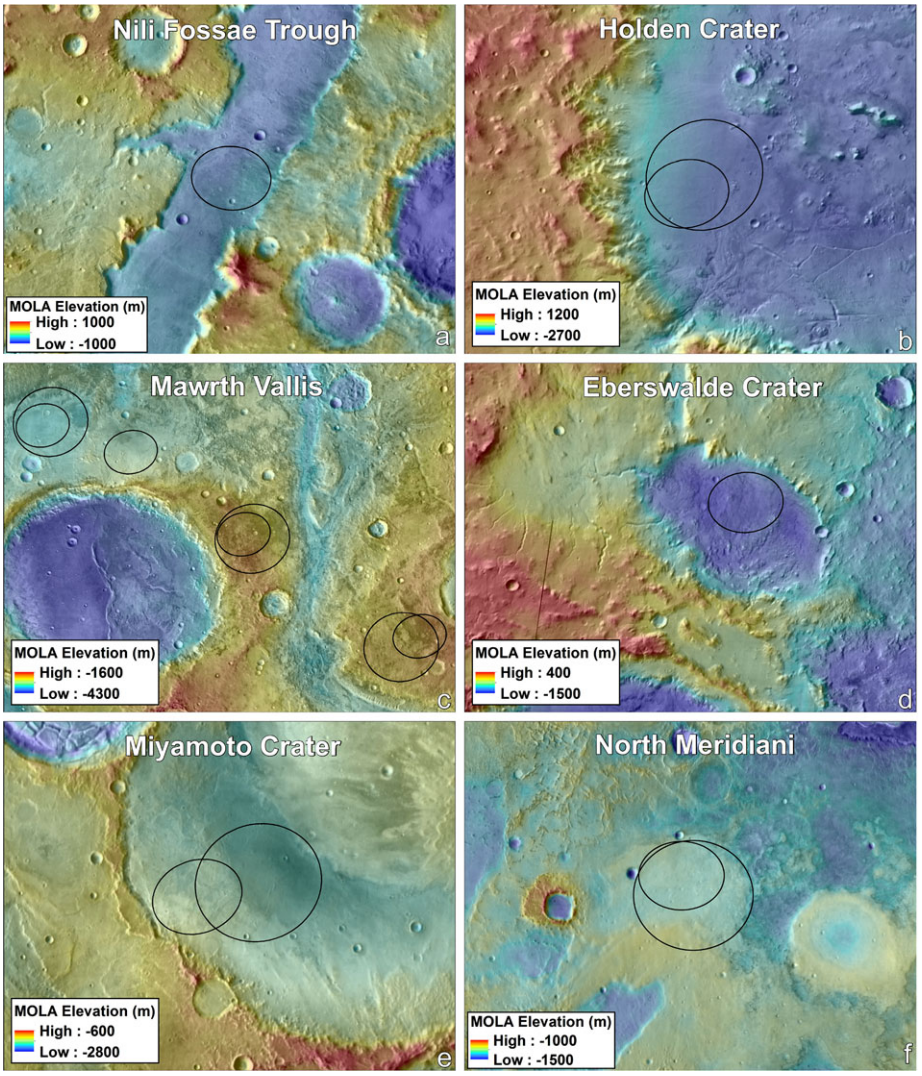

Fig. 3 Landing sites under consideration for the Mars Science Laboratory after the second landing site workshop and project meeting: (**a**) Nili Fossae, (**b**) Holden, (**c**) Mawrth, (**d**) Eberswalde, (**e**) Miyamoto, and (**f**) North Meridiani. Primary ellipses are 20 km by 25 km and safe haven ellipses are 32 km by 35 km at coordinates in Table 6. Base maps are THEMIS daytime thermal image mosaic overlain on MOLA topography with north up. Marwth ellipse numbers from northwest to southeast are 4, 1, 2, and 3

Quantin et al. 2005). Some of the beds may have been deposited in sublacustrine fans (Metz et al. 2009) and the depositional setting suggests water was present for at least hundreds to thousands of years (Metz et al. 2009).

A proposed ellipse west of Mawrth Vallis covers a thick, widespread, and layered sequence of rocks incorporating phyllosilicates and reflecting a complex aqueous history and alteration of basalt (Bibring et al. 2005; Bishop et al. 2008; Loizeau et al. 2007; Michalski and Noe Dobrea 2007; Poulet et al. 2005; Wray et al. 2008). Within the Mawrth

sequence, Al phyllosilicates overlie Fe/Mg phyllosilicates without any observable interbedding and whose emplacement may reflect pedogenic alteration (Loizeau et al. 2010) or aqueous alteration of volcanic ash deposits (Noe Dobrea et al. 2010), but remains uncertain (Bibring et al. 2005; Bishop et al. 2008; Michalski and Noe Dobrea 2007; Noe Dobrea et al. 2010; Wray et al. 2008). At least some of the layered materials predate nearby Mawrth Vallis (Loizeau et al. 2010), but it is unclear when their alteration ended, as development of the uppermost Al phyllosilicate bearing units may post-date formation of Mawrth Vallis (Wray et al. 2008).

The ellipse in Terby crater is adjacent to a ~2 km thick sequence of well-exposed, Noachian-aged, phyllosilicate-bearing, light- and intermediate-toned layered sedimentary deposits. The morphology of the layered deposits and their hydrated mineral signature (Ansan et al. 2005, 2011) is consistent with deposition in a long-lived lacustrine environment, but a loess-like origin cannot be ruled out (Wilson et al. 2007).

Additional discussion that included consideration of engineering constraints and science diversity further trimmed the list to six: Nili Fossae, Holden crater, Mawrth Vallis, Jezero crater, Terby crater, and Miyamoto crater (Golombek et al. 2008c). Three sites from the top 11 that did not make the final list, but might have satisfied the engineering constraints include NE Syrtis, Chloride sites, and E Meridiani. These three sites were deemed of lesser priority, but might have been considered among potential replacements if the final list of six were changed as a result of subsequent issues or considerations. It is important to note that these sites fell within two broad latitude bands for targeting the mission, with Holden, Terby and Eberswalde craters falling within the southern 15°S–30°S latitude band and Nili Fossae, Mawrth Vallis, Miyamoto, and Jezero craters falling within the northern 15°S–30°N latitude band. Uncertainties regarding how operations might be limited by the colder temperatures experienced in the southern latitude band made assessing inclusion of these sites difficult.

7.4 MSL Project Meeting

A subsequent MSL project meeting held on December 4, 2007 included a discussion of science potential, safety, engineering analysis, and programmatics of 11 sites. This included 10 of the 11 sites ranked highest at the second workshop (minus Melas Chasma, for which an MSL ellipse could not be safely placed) plus an additional site, North Meridiani. The N Meridiani site was considered to be safe relative to MSL engineering constraints and provided access to layered sulfates in the landing ellipse near the base of the unit traversed by the Opportunity rover. Exploration to the north and out of the ellipse would provide access to ridge-forming material with inverted channels and other evidence for past fluvial activity (Edgett 2005). Participants in the meeting included the Project Science Group (PSG), the Landing Site Steering Committee, site proposers, and key project personnel.

Six landing sites were recommended (Table 6): Nili Fossae trough, Holden, Mawrth Vallis, Eberswalde, Miyamoto and N Meridiani. This list is similar to that from the second community workshop with some exceptions. Jezero was subsequently found to have unacceptably high rock abundance. The MSL PSG recommended including Eberswalde for scientific reasons in place of Terby for which there were concerns about likely cold temperatures. It was recognized that each of these sites had potential liens due to various engineering, safety and operations concerns but all were accepted by the project engineering and management team for in-depth analysis (Golombek et al. 2008c).

Table 6 is the list of the six landing sites that were studied for landing MSL after the second workshop. For each site, the center latitude, longitude and elevation of the ellipse is listed as well as a possible safe haven ellipse (Fig. 3). Prime ellipses are 20 by 25 km and safe

Table 6 Downselected MSL landing sites

Name	Location	Elevation	Target
Nili Fossae Trough	21.01°N, 74.45°E	−608 m	Noachian Phyllosilicates
Holden Crater			
Primary	26.38°S, 325.08°E	−1940 m	Fluvial Layers, Phyllosilicates
Safe Haven	26.25°S, 325.21°E	−2137 m	
Mawrth Vallis			
Site 1 Primary	24.65°N, 340.1°E	−3093 m	Noachian Layered Phyllosilicates
Site 2	23.99°N, 341.04°E	−2246 m	
Site 2 Safe Haven	23.95°N, 341.11°E	−2254 m	
Site 3	23.21°N, 342.43°E	−2187 m	
Site 3 Safe Haven	23.12°N, 342.20°E	−2268 m	
Site 4	24.85°N, 339.42°E	−3359 m	
Site 4 Safe Haven	24.88°N, 339.78°E	−3355 m	
Eberswalde Crater	23.86°S, 326.73°E	−1450 m	Delta
Miyamoto Crater	3.51°S, 352.26°E	−1807 m	Phyllosilicates, Sulfates?
Safe Haven	3.09°S, 352.59°E	−1958 m	
N Meridiani			
Primary	1.58°N, 357.48°E	−1289 m	Layered Sulfates
Safe Haven	1.48°N, 357.55°E	−1301 m	
Gale Crater added	4.49°S, 137.42°E	−4451	Layered Sulfates and Phyllosilicates

haven ellipses are 32 by 35 km, both oriented along entry azimuths. Single prime ellipses were considered at each of the sites, except Mawrth, which has four. These sites became the focus of MRO image acquisition, with the emphasis on covering the prime ellipses and then on completing stereo for generating topographic maps for evaluating small-scale slopes.

7.5 First Consideration of New Landing Sites

On July 8, 2008 the NASA appointed Mars Landing Site Steering Committee reviewed new data collected by MRO and other spacecraft since the second workshop to ensure that new discoveries were considered in the process of identifying candidate MSL landing sites. Four new sites were submitted for consideration following a call to the Mars Landing Site Steering Committee, MRO Project Science Group (PSG), and the MSL PSG. These sites included: South Meridiani Planum (3.05°S, 354.61°E), Chloride "site 17" (3.07°S, 351.53°E), Gale crater (4.49°S, 137.43°E), and Nili Fossae carbonate (21.69°N, 78.85°E) (Golombek et al. 2009a).

The candidate ellipse for the South Meridiani Planum site is located on the hematite and sulfate plains south of the area traversed by the Opportunity rover (Arvidson et al. 2006; Squyres et al. 2006), but would also enable "go to" access to phyllosilicate-bearing, Noachian uplands to the south (Wiseman et al. 2008). An additional putative chloride site west of Miyamoto crater was proposed to examine the deposits in a small basin based on

rationale similar to that given for the previous chloride site south of Meridiani Planum and proposed at the second workshop (Osterloo et al. 2008, 2010).

An ellipse in Gale crater is north-northwest of a ~5 km-thick sequence of layered materials (Cabrol et al. 1999; Malin and Edgett 2000, 2001a, 2001b) possessing an intriguing sequence of phyllosilicate-bearing layers beneath sulfate-bearing layers, implying at least some of the sequence was deposited in an aqueous setting (Milliken et al. 2010). The layered sequence is in the central mound, requiring a "go to" drive and provides the opportunity to evaluate changing environmental conditions during the transition from Noachian-aged, phyllosilicate-bearing rocks to Hesperian-aged, sulfate-rich rocks (Milliken et al. 2010).

Finally, an ellipse was placed northwest of Isidis basin and was dubbed "Nili Fossae Carbonate" based on the detection of carbonate-bearing rocks (Ehlmann et al. 2008b). The carbonate site also provided access to various phyllosilicate-bearing lithologies, thereby enabling the relationship between these altered minerals and the regional Nili Fossae olivine unit to be analyzed (Ehlmann et al. 2008b).

After a two-week period to review the new sites, a telecon was held that included summary presentations of each site, safety concerns, and a discussion of the schedule and status of the site selection process. The 25 participants represented the Steering Committee, MSL PSG, NASA Headquarters, and individuals who had proposed the sites. There was unanimous agreement that all four of the new sites were potentially equally or more compelling than the existing six sites (Golombek et al. 2009a). Moreover, the new S Meridiani site was considered scientifically more compelling than the N Meridiani site and equally safe. Hence, the S Meridiani site was swapped for the N Meridiani site. Limited diversity of geologic targets at the Chloride site was a concern. The Gale crater site was preferred by a two-to-one margin over the Nili carbonate site. As a result, Gale crater was added to the existing list of sites under consideration, bringing the total to seven (Table 6).

7.6 Third MSL Landing Site Workshop

The Third Mars Science Laboratory (MSL) Landing Site Workshop was held September 15–17, 2008. The meeting was attended by approximately 125–150 participants; the main objective was to provide a general ranking of the sites based on science potential, with emphasis on defining the top third, middle third and bottom third (Golombek et al. 2009a). Presentations were grouped into an introductory session followed by individual sessions for each of the seven sites remaining under consideration. The introductory session included presentations on how to apply the scientific objectives of MSL to Mars and the selection of the landing site. Ample time was provided for discussion of all sites and supporting materials related to all aspects of the workshop, including individual presentation materials, were posted in real time at the landing site web sites.

All seven remaining sites clearly possess high science merit and were deemed by the MSL project to satisfy preliminary engineering criteria as understood at the time. The seven sites included in order of presentation: Miyamoto crater, S Meridiani Planum, Nili Fossae trough, Holden crater, Eberswalde crater, Mawrth Vallis, and Gale crater.

After all sites were presented and discussed, paper ballots were distributed that included 11 questions divided between four major mission-relevant landing site science criteria (Table 7): diversity, context, habitability, and preservation potential (with emphasis placed on diversity and context) that were developed to evaluate the landing sites. These specific questions within these criteria are shown in Fig. 4 and explained in Table 7. Workshop participants were instructed to assign green (highest), yellow, or red (lowest) colors to each site for each of the questions with emphasis placed on using all color categories to maximize the

Table 7 Four major mission relevant landing site science criteria

Criteria	Description
Diversity	A site with a variety of possible science objectives will ensure a greater chance for scientific success. Examples: multiple and differentiated science targets, multiple types of evidence (e.g., morphologic and geologic), variety in mineralogy or styles of stratigraphic expression.
Context	A site that can be placed in a larger, more regional context will ensure a greater depth of scientific understanding. The regional context provides constraints on past processes that led to the environments being examined locally. Locally derived results can, in turn, be extrapolated regionally or globally.
Habitability	Sites with orbiter-derived evidence for habitable environments can be assessed to make specific predictions that will guide the exploration strategy for MSL. Particular high-priority geologic targets can be identified that can be accessed, interrogated, and interpreted by MSL.
Preservation	Sites with a higher potential for preserving evidence for past habitable environments will ensure a greater chance of scientific success. Using terrestrial analogs, sites can be assessed for the particular physical and chemical conditions that retain mineralogic, chemical, or morphologic evidence.

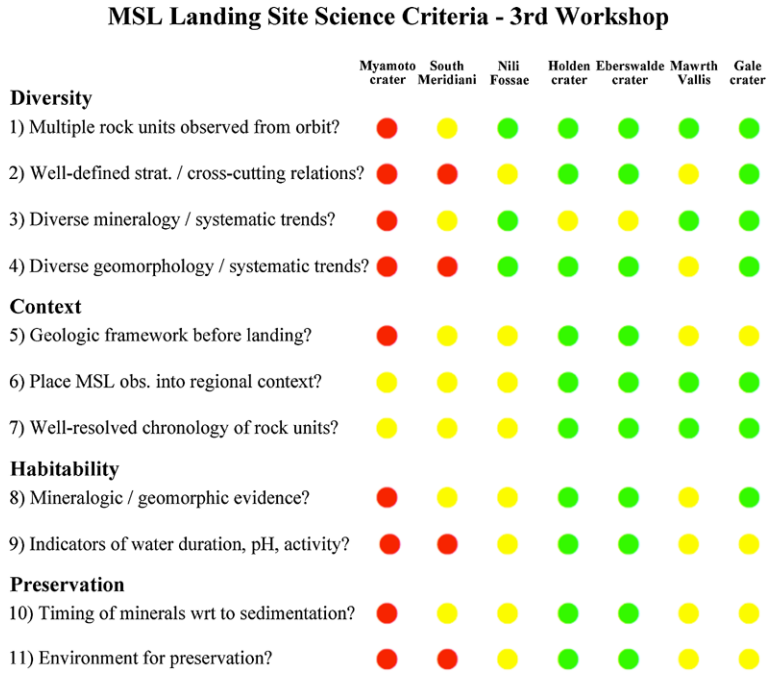

Fig. 4 Science criteria ranking for 7 sites considered from voting at the Third Landing Site Workshop using the criteria in Table 7 and the specific questions for those criteria shown herein, with *green* being high value, *red* low value and *yellow* intermediate. At a subsequent project meeting, the sites under consideration were reduced to four with highest science ranking: Holden, Eberswalde, Gale, and Mawrth (ellipse 2), with Miyamoto, South Meridiani and Nili Fossae being dropped from consideration

ability to differentiate between sites. Results of the voting were presented as both the mode (color receiving the most votes) and weighted average (assigning five points to each green vote, three to each yellow vote, and one to each red vote that were then summed and divided by the total number of votes). Both methods yielded similar results (Fig. 4).

Eberswalde, Holden, and Gale craters were the three highest ranked sites based on science potential and were closely followed by Mawrth Vallis (ellipse 2) and Nili Fossae trough. Miyamoto crater and South Meridiani were deemed to possess lesser relative science merit. Because both Eberwalde crater and Holden crater are southern latitude sites that are sensitive to unresolved engineering concerns related to operations and mobility (not discussed at the workshop) it was deemed reasonable to carry four sites forward: the top three and either Mawrth Vallis or Nili Fossae.

7.7 MSL Project Meeting

On November 5, 2008, representatives of the MSL project management, engineering, and science teams met with members of the external MSL Landing Site Steering Committee and selected project review board members to discuss the engineering assessment of landing safety, traversability, and the current status of predicted actuator thermal performance, in order to combine this information with the science rankings from the third workshop. Project resources and timeline allowed only three or four sites to have the full data acquisition and detailed analyses required for final certification and approval.

The Science ranking from the third community workshop (Fig. 4) and vetted without change by the MSL Project Science Group was expressed in three groups from most prefered (Group 1: Holden, Eberswalde, Gale) to least prefered (Group 3: Miyamoto, S. Meridiani); with intermediate Group 2 (Mawrth, Nili). The Engineering ranking (focused on entry, descent and landing risk) was divided into 2 groups: Group 1—most safe (Holden, Gale, Mawrth), Group 2—less safe (Eberswalde, risk still fairly low for portions of ellipse, but potential high slopes and rock coverage issues in the remainder of ellipse), and "Group 2.5" (Nili, highest risk site due to high altitude stressing parachute deploy mach number and general entry and descent timeline margin; some entry, descent and landing review board members found it to have nearly unacceptable overall risk).

By comparing the science and engineering groupings, it was clear that Holden and Gale were in Group 1 for both and should be finalists. Mawrth advanced next due to being in Group 1 engineering and Group 2 science. It was then decided that the fourth and final site to advance should clearly be the last "Group 1" science site, Eberswalde, due to its strong science value and be subject to further data acquisition and safety assessment. Therefore the final four sites selected for further analysis were: Holden, Gale, Mawrth (ellipse #2), and Eberswalde (Golombek et al. 2009a, 2010).

7.8 Second Consideration of New Sites

Because of the delay in launching MSL and extensive new remote sensing data, a call was issued for potential new sites in August 2009. Addition of any new site required both mineralogic and morphologic evidence demonstrating a compelling case that it was at least as promising as the four sites under evaluation. Moreover, any proposed sites must appear as safe as the four sites under consideration (Golombek et al. 2011b).

As summarized by Grant et al. (2010a), seven new candidate sites were submitted by the science community and initially discussed by the Steering Committee in December,

2009: (1) Nili Carbonate plains (Ehlmann et al. 2008b) including ultramafic, phyllosilicate-bearing, and carbonate-bearing outcrops (21.7°N, 78.8°E), (2) a diverse assemblage of minerals straddling the Noachian-Hesperian boundary in northeast Syrtis (16.7°N, 76.9°E) with an ellipse to the north of the previous Syrtis sites (e.g., Bibring et al. 2005, 2006; Ehlmann et al. 2010; Mustard et al. 2008, 2010; Poulet et al. 2008a, 2008b; Mustard and Ehlmann 2009), (3) a delta deposit with possible toe-of-slope silica deposits (Popa et al. 2010) within a crater in Xanthe Terra (2.3°N, 309°E), (4) a putative chloride deposit (Osterloo et al. 2008, 2010) and possible overlying phyllosilicate deposits in east Margaritifer Terra (5.6°S, 353.5°E), (5) a putative chloride deposit (Osterloo et al. 2008, 2010) and nearby phyllosilicates deposits (Christensen et al. 2009) in Ladon basin (18.8°S, 332.5°E), (6) ice within a crater (Aftabi 2008) in Vastitas Borealis (70.5°N, 103°E), and (7) channels on the floor and near the wall of Valles Marineris (3.8°S, 324.6°E).

Only five of the sites proposed were evaluated: Vastitas Borealis (Aftabi 2008) and the floor of Valles Marineris were declared outside the bounds of existing engineering requirements for MSL. For the sites discussed, extensive eolian bedforms in the Nili Carbonate ellipse raised concerns. The delta deposit in Xanthe Terra (Popa et al. 2010) was dropped because of concerns about slopes within and outside the ellipse, uncertainties about the relationship between the depositional setting and remote detection of nearby amorphous silica, and fears that nearby phyllosilicates might not be accessible. Putative chloride deposits (Osterloo et al. 2008, 2010) in Ladon basin were near phyllosilicate deposits (Christensen 2009), but the stratigraphic relationship between them was unclear and resulted in diminished appeal.

The remaining two sites were then targeted for high spatial and spectral resolution coverage and the Steering Committee reconvened in May 2010, to further discuss the science merit of the sites as well as landing site safety based on initial evaluation of thermal inertia, slopes, and other first order safety parameters. The northeast Syrtis site was deemed scientifically compelling because it displayed an exposed rock sequence spanning the Noachian-Hesperian boundary, abundant and varied aqueous mineralogy, and likely represented diverse geologic settings that was probably formed *in situ* (Mustard and Ehlmann 2009). Significant concerns were raised, however, about slopes, scarps, and other landing hazards. The Committee felt that the "land on science" nature of the east Margaritifer Terra site (Christensen 2009) was attractive, but questions about the depositional setting and stratigraphic context of the chloride and phyllosilicates, concerns about eolian ripples and other potential hazards to landing safely and rover trafficability led to its being dropped. As a result, the Committee made the recommendation that neither the northeast Syrtis nor east Margaritifer Terra should be added to the existing four final MSL candidate landing sites (Golombek et al. 2011b).

7.9 Fourth Landing Site Workshop

The Fourth MSL Landing Site Workshop was open to the science community and was held September 27–29, 2010. Workshop presentations were grouped into an introductory session followed by individual sessions for each of the four sites. A final session on the morning of the last day was related to ongoing characterization of the candidate sites. Ample time was provided for discussion at the end of each session and on the final day of the workshop and was focused on the science opportunities afforded at each site. All discussion sessions were lively and involved. Supporting materials related to all aspects of the workshop, including all presentation materials, were posted in real time at the landing site web sites, providing an additional means for participants to review each site (Golombek et al. 2011b).

Table 8 Final 4 MSL landing site ellipse coordinates

Ellipses are 25 km by 20 km oriented east-west for the 2011 launch opportunity. Longitude, positive E, planetocentric. Elevation with respect to the MOLA geoid

Landing Site	Latitude (°)	Longitude (°)	Elevation (m)
Eberswalde	23.8953°S	326.7426°E	−1435
Gale	4.4868°S	137.4239°E	−4444
Holden	26.4007°S	325.1615°E	−2177
Mawrth	23.9883°N	341.0399°E	−2245

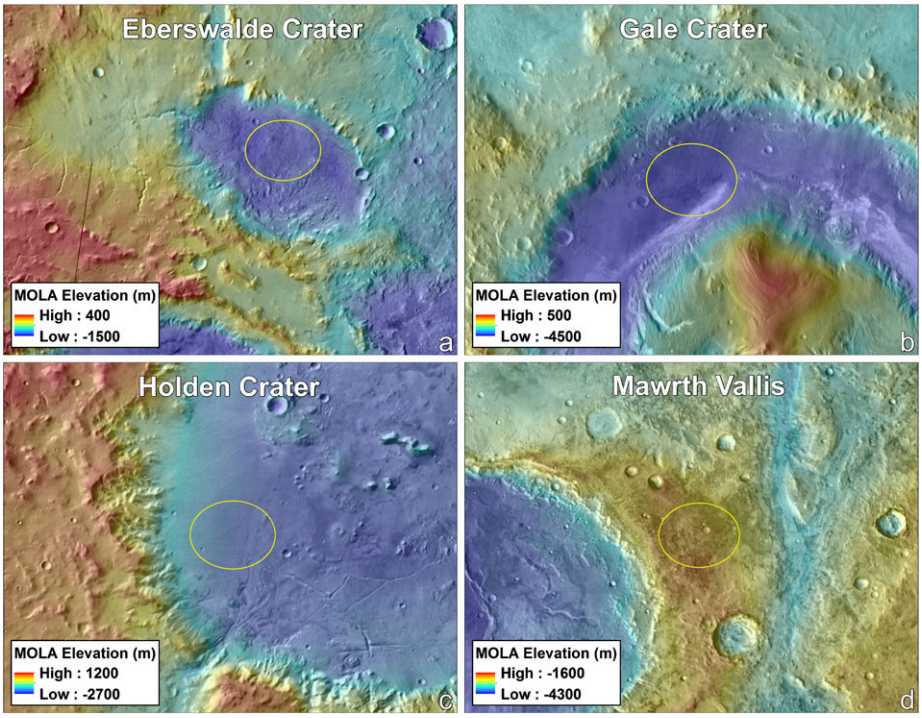

Fig. 5 Final 4 MSL landing ellipses on THEMIS daytime thermal image mosaic overlain on MOLA topographic maps: (**a**) Eberswalde, (**b**) Gale, (**c**) Holden, and (**d**) Mawrth (ellipse #2). Ellipses are 25 by 20 km oriented east-west for the 2011 opportunity with center coordinates in Table 8

All four remaining sites clearly possessed high science merit and were deemed to be generally safe for landing by the MSL project. Summary statements representing strong community consensus on the science merits of the sites were generated at the workshop. A common theme that emerged for each site was the need to develop specific sets of targets for exploration by the rover within and outside of the proposed landing ellipse. Coordinates for the 2011 ellipses at these locations are provided in Table 8 and shown in Fig. 5.

7.10 Fifth Landing Site Workshop

The Fifth and final MSL Landing Site Workshop was held May 16–18, 2011 and focused on scientific uncertainties for the four remaining candidate landing sites. The meeting was well attended on all three days, with well over 150 participants from the science commu-

nity and the MSL science team. Workshop presentations were grouped into an introductory session followed by individual sessions for each of the four remaining sites. There was also discussion of possible planetary protection issues related to the candidate sites, and a closing session related to ongoing characterization of the candidate sites with respect to landing safety and rover traversability. Time was provided for discussion at the end of each session and on the final day of the workshop. The product of the workshop was a series of summary statements or "quad charts" that highlight their science merits, deficiencies, and uncertainties as measured against major science objectives of the MSL mission (Tables 9, 10, 11, 12). All four sites possess high scientific merit and were deemed to be safe for landing and trafficable for the rover by the MSL project. The extremely high science merit of each of the sites was best expressed by the unanimous agreement from workshop participants that all four sites represented acceptable science targets for exploration by MSL. It is important to note that while the statements in the charts represent consensus, they did not represent a unanimous opinion of the community (or the Steering Committee) in a few instances.

8 Science Objectives of the Final Four Landing Sites

The primary scientific goal of the Mars Science Laboratory (MSL) is to assess the present and past habitability of Mars, with special emphasis on diversity, context, habitability, and preservation potential of target materials at the landing site (Grotzinger 2009; Grotzinger et al. this issue). Each of the four final candidate sites discussed at the fourth and fifth landing site workshops clearly possess high science merit and were deemed to be generally safe for landing by the MSL project. Further, there was unanimous agreement from participants at both the fourth and fifth workshops that all four of the sites represent acceptable science targets for exploration by MSL. The four sites in alphabetical order are: Eberswalde crater (23.9°S, 326.7°E), Gale crater (4.5°S, 137.4°E), Holden crater (26.4°S, 325.2°E), and Mawrth Vallis (24.0°N, 341.0°E). The following is a summary of the science at the final four sites as discussed at the fifth workshop with emphasis placed on citation of new results and discussion of the sites at that final workshop. As such, the section represents the material available to the community for evaluation of the sites at that time and not only provides information on conclusions about their merits, but also serves to identify remaining gaps in knowledge about their geologic evolution. The overarching hypothesis, pros, cons, and uncertainties are also included in the summary consensus statements in Tables 9–12.

8.1 Eberswalde Crater

At Eberswalde crater the over-arching hypothesis is that crater stratigraphy, geomorphology, and mineralogy record the evolution of a crater lake (Table 9), the history of hydrologic and climatic change resulting in the formation of a fluvial-deltaic system (e.g., Moore et al. 2003; Malin and Edgett 2003; Lewis and Aharonson 2006; Pondrelli et al. 2008), and a sedimentary depositional environment that might have been favorable to the preservation of organic materials and/or other kinds of biosignatures (Rice et al. 2011). In Eberswalde crater, the distribution and orientation of phyllosilicate-bearing beds appears consistent with the past presence of a long-lived fluvial-deltaic system (Bhattacharya et al. 2005). The candidate landing ellipse is on the crater floor and would provide access to lake sediments whereas delta deposits are located around the edge of the crater, with the largest towards the west (Rice et al. 2011). The large delta flanking the western edge of Eberswalde is an excellent preservation of a fluvial-deltaic deposit into standing water (although there is limited evidence for a shoreline) and integrates sedimentary material from a broad source region.

Table 9 Eberswalde Crater site: summary consensus statement of science merits, deficiencies, and uncertainties

Overarching Hypothesis	Specific Pros of Site		Possible Cons of Site	Remaining Uncertainties
Eberswalde crater stratigraphy, geomorphology, and mineralogy record the evolution of a crater lake, the history of hydrologic and climatic changes resulting in the formation of fluvial-deltaic systems, and a sedimentary depositional environment that might have been favorable to the preservation of organic materials and/or other kinds of biosignatures.	*Setting* Eberswalde shows excellent preservation of a fluvial-deltaic system emplaced into a standing body of water that integrates sedimentary material from a broad source region. Additional, smaller fluvial-deltaic systems and possible lacustrine deposits are also present. The landing site provides the opportunity to reconstruct quantitatively the sedimentary, hydrologic, and climate conditions during deposition. Specific formation models allow prediction of locations to target for exploration with MSL. Bottom set beds from each lobe of the delta can be defined and provide targets in which to seek organics. Evidence for episodic channel-meandering migration is recorded in the delta and associated estimates of discharge suggest its deposition extended for several hundred thousand years or more based on terrestrial analogs. *Diversity* In addition to fluvio-lacustrine deposits (e.g., sinuous ridges), Holden crater ejecta and possible megabreccia related to the Eberswalde impact event occur. Some megabreccia may express veins related to hydrothermal activity. The materials in the ellipse and delta include clay minerals whose distribution is associated with different outcrop characteristics.	*Preservation* Orbital detection of clay minerals near the bottom of the delta front, maybe in bottom set deposits, define a well-defined target for exploration. There are also potential lake deposits within the landing ellipse that offer exploration targets. On Earth, such deposits can concentrate and preserve organics and evidence for habitability and life. *Exploration Targets* Well-defined fluvial-deltaic-lacustrine and megabreccia targets coupled with mineralogical diversity within and outside of the ellipse define a short and long term exploration strategy. Lacustrine sediments likely exposed in and near the ellipse and distribution is becoming well-mapped. Distribution of targets make exploration of the site a mix of land on and "go to."	Relatively limited variety and modeled abundance of phyllosilicate minerals known to preserve organics detected from orbit. Science in landing ellipse is secondary to that outside of the ellipse.	Little evidence for shorelines corresponding to the elevation of the delta surface and the spillway to the eastern basin, though some aspects of the system (including the poorly defined shorelines) suggest it may have been ice-covered (though no deformation of delta as might be expected if it was). Predictions made enable this to be evaluated in situ. Delta emplacement might be consistent with delivery of water and sediment shortly after the Holden impact; this cannot be ruled out in advance of landing, but tests are proposed to resolve in situ. Sediment contributions to the delta from Holden ejecta are uncertain though mapping of tributaries and characteristics of incision will help resolve in advance of landing. Delta is no older than Early Hesperian and some investigators believe it may have been deposited as late as the Early Amazonian, but there is no consensus whether a post-Noachian age is a concern for preserving organics or for preserving evidence for past habitability or life on Mars.

Table 10 Gale Crater site: summary consensus statement of science merits, deficiencies, and uncertainties

Overarching Hypothesis	Specific Pros of Site		Possible Cons of Site	Remaining Uncertainties
Strata within the 5 km thick mound of layered sediments within Gale crater record a sequence of aqueous habitable environments over an extended period. These strata contain multiple hydrous minerals (sulfates, phyllosilicates) that indicate varying aqueous environmental conditions.	*Setting* Diverse stratigraphy in a 5 km mound within a 5 km deep Late Noachian crater. Stratigraphy includes well-defined beds of hydrated minerals and the lower mound includes contributions by fluvial processes and likely reflects deposition during changing and possibly global scale wetter-to-drier environmental conditions. Alluvial materials and inverted channels in the ellipse record hydrologic conditions when they were emplaced and provide the opportunity to sample materials weathered and eroded from the crater walls. *Diversity* Multiple mineralogical and stratigraphic units within the 5 km thick mound sequence with alternating inter-bedded phyllosilicate and sulfate bearing beds in the lower mound. Stratigraphy comprising the mound is continuous over many km and is well characterized in places. Alluvium in the landing ellipse enables sampling crater rim materials that may record environmental conditions during their emplacement and from before the formation of the north-south dichotomy on Mars.	*Preservation* The phyllosilicate-bearing units in the lower mound and moat include smectites that would help preserve organics if present. Biosignatures may be best preserved in the sulfate bearing strata in the mound. *Exploration Targets* The specific distribution of science targets within and outside of the ellipse is well defined. Preserved organics could occur in a high thermal inertia unit in fan in ellipse, in clay rich layers that may not have sulfates, and in the sulfates.	The original extent and timing of processes responsible for the present mound morphology needs better definition and the regional and global stratigraphic context of the mound is not firmly established and it is unlikely that all depositional aspects of the mound will be understood in advance of landing. Science in landing ellipse on and near an alluvial fan is secondary to that outside of the ellipse and observations within the ellipse may be encumbered by dust.	Although several testable models for mound formation exist, uncertainty remains about the depositional setting for much of the stratigraphy despite a better understanding of the constituent mineralogy. Nevertheless, bed continuity and morphology implies the origin of the lower section involved deposition onto a wet surface or into standing water and there is evidence for fluvial redistribution of mound materials. The source of water associated with deposition remains uncertain, but if sediments were deposited in a lake, the relative paucity of associated valleys suggests groundwater as opposed to meteoric sources. The source of the lower mound sediments is unknown but likely from outside of the crater and it is uncertain whether the mound is part of a larger deposit (though it is morphologically similar to deposits seen elsewhere on Mars). Valleys breaching the rim at a stratigraphic level now lost to erosion may have contributed fill to the crater and/or in lake. Crater statistics suggest Gale crater is Late Noachian, whereas floor deposits onlapping the lower mound and including the fan in ellipse are interpreted to be Early Hesperian, thereby bracketing the age of the lower mound. Age of upper mound and total time recorded in the mound is uncertain. Preservation potential of organics in the sulfate units may be compromised by the known presence of iron oxides.

Table 11 Holden Crater site: summary consensus statement of science merits, deficiencies, and uncertainties

Overarching Hypothesis	Specific Pros of Site		Specific Cons of Site	Remaining Uncertainties
Holden crater preserves evidence of a closed fluvial-lacustrine system that provides the opportunity to apply a geomorphic systems approach to evaluating and preserving evidence for a sustained, habitable environment.	*Setting* The bajada in the ellipse and light-toned layered materials comprise one of the largest and best preserved alluvial systems on Mars. The diverse and potentially weathered sediments likely record the environmental conditions responsible for their formation during the Hesperian, and perhaps into the Early Amazonian. This sequence is underlain by the light-toned layered deposits and overlying Uzboi flood deposits and enable the age of the target deposits to be related to global stratigraphy. Collectively, additional diverse and widespread megabreccias in and outside the ellipse and alluvial materials in the ellipse suggests sampling of rocks ranging in age from early crustal Noachian to perhaps into the Hesperian or even Early Amazonian. *Diversity* Diversity is represented by fan sediments, phyllosilicate-bearing light toned layered deposits, Uzboi flood deposits, and mega-breccias in the crater walls/floor. The mineralogical diversity in the light-toned layered deposits and crater walls/floor include both altered and primary compositions.	*Preservation* Strata comprising the light-toned layered materials may be the equivalent of bottom set beds emplaced in a lacustrine setting, which might preserve organics for interrogation by the MSL. *Exploration Targets* Well-defined exploration targets exist within and outside the landing ellipse. Targets within the ellipse offer access to all major units for interrogation, though thicker sections of the light-toned layered materials and megabreccias occur farther to the south. Putative bottomset beds provide a target for evaluating any preserved organics.	Origin of stratified light-toned materials as lacustrine versus alternate depositional processes remains uncertain, but in situ evaluation of bedding character and chemistry is likely to distinguish origin. Relatively limited variety of phyllosilicate minerals known to preserve organics detected from orbit.	There are no shorelines or stratal geometries and limited evidence for other properties associated with the light-toned layered deposits and fans that can be used to more confidently define their origin and genetic relationships. Diverse megabreccia occurrences within the ellipse, walls, and rims may include evidence that they supported an impact-induced hydrothermal system. Light-toned layers high on the west wall of Holden may relate to older beds excavated from the pre-existing Holden basin. Age of light-toned layered deposits and adjacent alluvial fan surfaces are no older than Early Hesperian and fans may be as young as Early Amazonian, though there is no consensus whether this is an issue for habitability and evaluating conditions for life.

Table 12 Mawrth Vallis site: summary consensus statement of science merits, deficiencies, and uncertainties

Overarching Hypothesis	Specific Pros of Site		Possible Cons of Site	Remaining Uncertainties
Mawrth Vallis records geologic processes during early Martian history, when aqueous phyllosilicate-forming processes were pervasive and persistent. This site provides the opportunity to understand the potential for early habitability on the planet and may be representative of global conditions on Mars.	*Setting* Exposes the oldest preserved rocks of the four candidate sites and provides an opportunity to explore Noachian crust to seek and investigate information about the processes active on early Mars. The relative ages of exposed rocks are well constrained and suggests they are among the oldest preserved on Mars and might be from a period not recorded in the rock record on Earth. Hydrated minerals are present and modeled to contribute several tens of percent by volume to the rocks (most of any of the sites) that formed in aqueous environments. The section within and near the landing ellipse appears to be mineralogically representative of other Noachian crustal sections in Arabia Terra, thus allowing an understanding of what possibly were widespread processes on early Mars. Capping mesa-forming materials appear unaltered and may record changing conditions during the Hesperian and younger times. *Diversity* The ellipse and go to outcrops encompass a diverse, complex mineralogical and rock sequence that includes many of the hydrated minerals found on Mars (multiple phyllosilicates and sulfates) whose formation records varying aqueous environmental conditions and any changes in surface aqueous alteration environments. Rocks were likely emplaced by multiple geologic mechanisms that probably included diagenetic (e.g., for Al-phyllosilicates), impact, fluvial, and/or pedogenic processes, and remain in situ.	*Preservation* Several locations in close proximity and within the ellipse may allow interrogation of a variety of rocks to help define the early period of time when water was present and determine whether the environment was habitable. The phyllosilicate-bearing units include smectites, suggesting they are well preserved and may contain/help preserve organics. *Exploration Targets* A good list of prioritized targets within the ellipse has been identified and targets outside the ellipse, including sulfates, are also well-defined. Both the Mg/Fe and Al- bearing phyllosilicate units need to be interrogated to assess the nature and distribution of any organics.	There is no consensus on the depositional setting or the mechanisms for concentrating or preserving organics and it is unlikely that the depositional setting will be further refined prior to landing and in situ evaluation. Although textural and chemical characterization of the units using the MSL payload may distinguish between models for emplacement history, there is not a consensus that such an approach will be successful.	The depositional setting(s) associated with emplacement of the rocks and mineralogic units at Mawrth remains uncertain, is unlikely to be resolved using existing orbital data sets, but may be resolved in situ. It is uncertain if the observed alteration record (i.e., represented by the Al-phyllosilicates) extends to the primary Fe/Mg smectite deposit and its potential organic record. It remains uncertain whether Oyama crater ejecta persists or which unit it might correspond to, though Al-phyllosilicates likely post-date Oyama. The amount, source, and duration of interaction with water in development of the units remains uncertain.

Two distinct clay minerals whose distribution is associated with different outcrop characteristics have been observed in Eberswalde, and are most abundant near the bottom of the delta front in possible bottomset deposits (Milliken and Bish 2010) that would form a well-defined target for exploration. In addition to the multiple delta-associated deposits, potential lake deposits occur on the crater floor and offer additional exploration targets as they may concentrate and preserve organics and evidence for habitability and life (Rice et al. 2011). Sinuous ridges in Eberswalde and hills of Holden megabreccia ejecta also occur in the landing ellipse and provide additional exploration targets (Milliken et al. 2010; Rice et al. 2011). Although discussed, it remains unclear whether the source of the water responsible for delta emplacement was related to the Holden impact or broader climatic conditions. Nevertheless, it is possible that the largest delta in Eberswalde is related in time to other alluvial deposits in the southern Margaritifer Terra region and formation may have occurred in the Late Hesperian or into the Early Amazonian (Grant and Wilson 2011). The landing site on the crater floor coupled with a traverse to the delta front to the west provides the opportunity to quantitatively reconstruct the sedimentary and hydrologic conditions during deposition and specific formation models enabled identification of specific locations to target for exploration with MSL.

8.2 Gale Crater

For the Gale crater site, the over-arching science hypothesis relates to the strata forming the mound within the crater to the south of the candidate landing ellipse (Table 10) and that it at least in part reflects accumulation in an aqueous habitable environments over an extended period of time (Thomson et al. 2011). Gale crater exposes a thick sequence of finely bedded deposits with more phyllosilicate-bearing rocks beneath sulfate-bearing rocks (Anderson and Bell 2010; Thomson et al. 2011), though alternating inter-bedded phyllosilicate and sulfate bearing beds are present in the lower mound (Milliken et al. 2010). Stratigraphy in the mound is continuous over many km and well characterized in places and deposition of the sedimentary sequence may relate to aqueous and/or eolian processes (Anderson and Bell 2010) with multiple mineralogical and stratigraphic units occurring within the 5 km thick mound sequence. While the ultimate source(s) of the sediments comprising the mound and the original extent of the constituent layers remain uncertain, the present expression of the mound is largely the result of eolian modification (Hobbs et al. 2010).

A transition from clay-bearing strata near the base of the mound to more sulfate bearing rocks higher in the mound may record a change from relatively wetter to drier conditions across the Noachian to Hesperian boundary (Milliken et al. 2010; Thomson et al. 2011). An unconformably overlying upper unit appears more consistent with eolian deposition (Anderson and Bell 2010). Although the setting represented by the diverse stratigraphy in the 5 km mound within Gale crater and adjacent areas remains uncertain, it is likely to be better defined by MSL. The phyllosilicate bearing units and sulfate bearing strata in the lower mound appear well exposed and may preserve organics and biosignatures (Anderson and Bell 2010). A number of specific targets for exploration to help refine our understanding of the depositional setting and whether it was characterized by potentially habitable conditions have been identified.

8.3 Holden Crater

At Holden, the over-arching hypothesis is that it preserves evidence of a closed fluvial-lacustrine system and provides the opportunity to evaluate and search for evidence of a

sustained, habitable environment in a setting where the sources and sinks of sediments and water are well constrained (Grant et al. 2008, 2010b, see Table 11). Images of the interior of Holden crater reveal laterally extensive, sub-meter phyllosilicate-bearing strata near the edge of the landing ellipse that is located on a bajada (Grant et al. 2008). The deposits are phyllosilicate-bearing (Milliken and Bish 2010) and the extent, scale, and orientation of the encompassing layers are likely indicative of emplacement in a distal alluvial and/or lacustrine setting (Grant et al. 2008, 2010b). The deposits were subsequently eroded and overlain by sediments carried into the crater by water draining from Uzboi Vallis (Grant et al. 2008, 2011). In Holden, fans flanking the western wall of the crater (and in the ellipse) appear to onlap more flat-lying light-toned strata lower in the section (Grant et al. 2008) and their emplacement may have extended into the Late Hesperian or Early Amazonian (Grant and Wilson 2011). The flat-lying light-toned rocks are not likely younger than Hesperian in age (Grant et al. 2010b, 2011). If the light-toned layered deposits on the crater floor, outcropping within the eastern edge and to the south and east of the ellipse, are bottomset beds (Grant et al. 2008, 2010b) they would comprise one of the largest and best preserved lacustrine systems on Mars and by analogy with lacustrine settings on the Earth suggests they may represent a good environment for preserving organics for interrogation by the MSL payload. Additional diversity is represented by mega-breccias in the crater walls/floor (Grant et al. 2008), which when combined with the aforementioned materials suggests the Holden site may include rocks covering the greatest section of Martian history of the four final sites. Further, the Holden sequence is bounded by the crater floor/walls and overlying Uzboi flood deposits (Grant et al. 2011) that enable the age of the fans and light-toned layered deposits to be placed firmly within the global stratigraphy (Grant and Parker 2002). Nevertheless, clear evidence for shorelines and/or stratal geometries that could confirm the depositional origin and relationship of the various units is lacking and requires in situ exploration. A variety of targets within and outside of the landing ellipse provide specific locations where outcrops may exist enabling various depositional models to be tested.

8.4 Mawrth Vallis

At Mawrth Vallis the over-arching hypothesis is that clay-bearing rocks record geologic processes during early (late Noachian) Martian history (Loizeau et al. 2010; Michalski et al. 2010b), when aqueous phyllosilicate-forming processes were pervasive and persistent. The site provides the opportunity to understand the potential for early habitability on the planet and may be representative of global conditions on Mars (Table 12). The landing ellipse west of Mawrth Vallis is on plains that display evidence for strata containing Mg–Fe smectites and Al-rich phyllosilicates (e.g., Loizeau et al. 2007, 2010; Bishop et al. 2008; Wray et al. 2008; McKeown et al. 2009; Michalski et al. 2010a, 2010b), sulfates (Noe Dobrea et al. 2011), and possibly jarosite (Farrand et al. 2009) that record varying aqueous environmental conditions and changing surface aqueous alteration environments. Constituent rocks were likely emplaced by multiple geologic mechanisms that probably included diagenetic, impact, fluvial, and/or pedogenic processes, and remain in situ (Michalski et al. 2010a, 2010b). The relationship of rocks in and near the landing ellipse to nearby Oyama crater remains uncertain (Loizeau et al. 2010), although layered, clay-bearing units appear to be exposed in the walls of the crater (and thus predate it), and aluminous clays appear to be deposited on the crater floor (and therefore postdate the crater). As is the case for Gale, further refinement of the set of depositional processes responsible for the sequence likely awaits in situ exploration.

The landing site is within the most extensive (Michalski et al. 2010a, 2010b; Noe Dobrea et al. 2010, 2011) and phyllosilicate-rich deposit (clays may contribute several tens of

percent by volume to the rocks) on the planet (Poulet et al. 2008b; Michalski et al. 2010a, 2010b) and may extend throughout western Arabia Terra (Noe Dobrea et al. 2010). Capping mesa-forming materials appear less altered and may record changing conditions during the Hesperian and younger time (Loizeau et al. 2010). A number of targets were identified and discussed at the fifth workshop and provide specific locations where varying depositional hypotheses can be evaluated. The site likely provides an opportunity to explore Noachian crustal materials to constrain the processes including aqueous, which were active on early Mars (Michalski et al. 2010a, 2010b).

9 Surface Characteristics of the Final Four Landing Sites

9.1 Introduction

Understanding the relationship between orbital remote sensing data and the surface is essential for safely landing spacecraft and for correctly interpreting the surfaces and materials globally present on Mars (see review in Golombek et al. 2008b and references therein). Landing site selection for the six successful landers included intense periods of data analysis of pre-existing and incoming information. These landing site selection efforts and the assessment of predictions after landing form the basis for much of our knowledge about how surface characteristics investigated by the landers and rovers relate to their remote sensing signatures. These landing site selection efforts and comparison with predictions from remote sensing data after landing has shown that surface characteristics at the six sites where spacecraft have successfully landed on Mars can be related favorably to their signatures in remotely sensed data from orbit and from the Earth. Comparisons of the rock abundance, types and coverage of soils (and their physical properties), thermal inertia, albedo, and topographic slope all agree with orbital remote sensing estimates and show that the surface characteristics of landing sites important for safely landing spacecraft can be accurately predicted with available remote sensing data (e.g., Golombek et al. 2008b, 2009b). Because the quality and quantity of orbital remote sensing information used to characterize the surface of the landing sites has drastically improved in the modern era of Mars exploration, the fidelity of the predictions from orbit has also improved. As an example, although geological expectations of the landing sites have not always been met (e.g., Golombek et al. 2005), the most recent landing by Phoenix using MRO data matched exactly what was expected from remote sensing data in both surface characteristics as well as geologic expectations.

9.2 Global Thermal Inertia and Albedo

A general relationship has been found between kilometer scale global thermal inertia (see also Sect. 9.3.1) and albedo data and specific materials found in the surface layer at the six landing sites (e.g., see reviews by Christensen and Moore 1992; Golombek et al. 2008b). The six landing sites sample two of the three dominant global thermal inertia and albedo units that cover ~80 % of the surface of Mars (units A, B and C in Putzig et al. 2005). The Viking (VL), Spirit (SPI), and Phoenix (PHX) landing sites (Fig. 6) sample the moderate to high thermal inertia and intermediate to high albedo unit C that is dominated by crusty, cloddy, blocky or frozen soils (duricrust) with various abundances of rocks and bright dust (Golombek et al. 2008b, 2009b; Jakosky and Christensen 1986; Christensen and Moore 1992; Moore and Jakosky 1989; Mellon et al. 2000, 2008; Putzig et al. 2005). The Opportunity landing site is representative of the moderate thermal inertia and low albedo surface unit B that is relatively dust free and composed of dark eolian

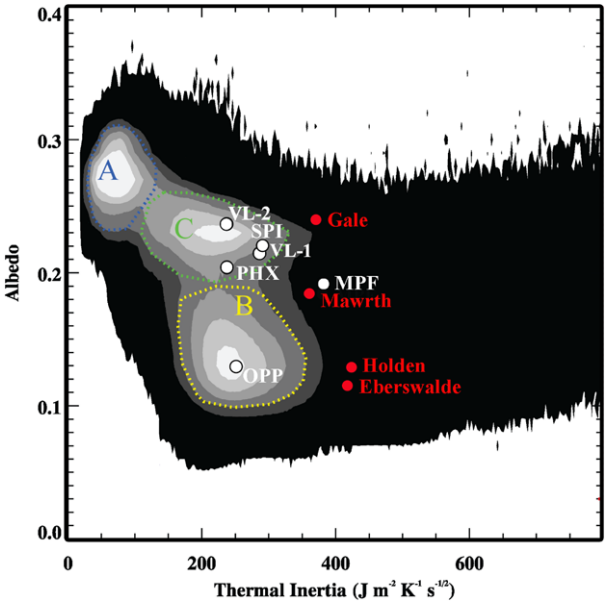

Fig. 6 Global TES thermal inertia versus albedo showing the three major thermal inertia-albedo units (A, B and C) that make up ~80 % of the surface of Mars along with the six previous landing sites and the final four MSL landing sites. Unit A has high albedo and very low thermal inertia (unit A) and is dominated by potentially thick bright red dust with very low rock abundance. Unit B, in which Opportunity (Opp) landed, has low albedo and is relatively dust free. Unit C, in which VL1, VL2, Spirit (SPI), and Phoenix (PHX) landed has moderate thermal inertia and intermediate to high albedo that is dominated by crusty, cloddy, blocky or frozen soils (duricrust) with various abundances of rocks and bright dust. Mars Pathfinder (MPF) has an albedo between units B and C, but has higher thermal inertia. The Mawrth 2 site is similar to MPF and Holden and Eberswalde have low albedo similar to Opp, but higher thermal inertia. Holden and Eberswalde should be relatively dust free; Mawrth should be as dusty as MPF. The Gale ellipse should be dusty, based on its albedo, but the higher thermal inertia indicates cemented soils. Plot adapted from Putzig et al. (2005). Thermal inertia and albedo data are from TES (Putzig and Mellon 2007)

sand and/or increased abundance of rocks. MPF has an albedo between units A and B, but has higher thermal inertia and resembles unit C sites with less dust (similar to dust devil tracks swept free of dust traversed by Spirit). The third main thermal inertia and albedo unit of Mars has high albedo and very low thermal inertia (unit A) and is dominated by potentially thick bright red dust with very low rock abundance. Such dusty areas have been eliminated as possible landing sites for solar-powered or rover missions due to concerns about dust coating the solar panels (reducing power) and sinkage as this material does not appear to be load bearing nor trafficable (Golombek et al. 2008b). Comparisons of soils and rocks covering the landing sites indicate that the main contributor to the bulk thermal inertia is the degree of induration or cementation (and grain size) of the soils or fine component, rather than rock, which generally cover less than one third of the surface (Jakosky and Christensen 1986; Mellon et al. 2000, 2008; Putzig et al. 2005; Fergason et al. 2006b). In addition, the albedo scales directly with the amount of dust and drift deposits observed at the landing sites, with higher albedo sites covered with more dust and drift deposits (Golombek et al. 2008b).

Three of the final four MSL landing sites generally have albedos similar to Unit B (Fig. 6, Table 13). Holden (0.13) and Eberswalde (0.12) have albedos as low as the Opportunity

Table 13 Landing site ellipse data

Site	Eberswalde	Gale	Holden	Mawrth	Phoenix	Opportunity	Spirit	MPF	VL2	VL1
Latitude of Ellipse, deg	−23.8953	−4.4868	−26.4007	23.9883	68.15	−2.06	−14.64	19.13	47.67	22.27
Longitude of Ellipse, +E, deg	326.7426	137.4239	325.1615	341.0399	233.97	353.77	175.06	326.78	134.26	312.03
Latitude of Lander, deg					68.22	−1.95	−14.57	19.10	47.67	22.27
Longitude of Lander, +E, deg					234.25	354.47	175.48	326.75	134.28	312.05
MOLA Elev., km, Ellipse center	−1.4	−4.4	−2.1	−2.2	−4.143	−1.440	−1.920	−3.7	−4.5	−3.6
Range	−1.6 to −1.2	−4.5 to −4.1	−2.3 to −1.6	−2.6 to −2.0	−2.6 to −2.0	−1.4 to −1.6	−1.8 to −1.9			
Lander elevation					−4.126	−1.384	−1.941	−3.7	−4.5	−3.6
Geoid, km, COM	3392.556	3395.641	3391.966	3392.498	3380.724	3395.526	3394.227	3393.482	3386.349	3339.299
1.2 km bi-dir slope, deg, mean ± SD	1.14 ± 0.96	1.23 ± 1.05	0.49 ± 0.44	0.84 ± 0.61	0.37 ± 0.31	0.15 ± 0.18	0.20 ± 0.44	0.25 ± 0.66	0.29 ± 0.29	0.26 ± 0.96
RMS, deg					0.48	0.26	0.49			
n	817	841	910	863	2356	680	679			
900 m bi-dir relief (m), mean ± SD	18.7 ± 16.7	18.5 ± 15.5	8.0 ± 7.1	14.2 ± 10.9						
n	747	770	723	788						
MOLA Pulse Width, m, mean ± SD	2.08 ± 2.55	1.99 ± 1.54	1.35 ± 1.04	1.98 ± 1.19	1.33 ± 1.27	0.84 ± 0.46	1.34 ± 1.11	1.52 ± 1.81	1.22 ± 0.55	1.54 ± 2.4
n	703	233	692	425	47371	2357	757	25853	10560	19848

Table 13 (*Continued*)

Site	Eberswalde	Gale	Holden	Mawrth	Phoenix	Opportunity	Spirit	MPF	VL2	VL1
Self affine 100 m Allan dev, m	5.3	4.0	3.3	3.7		3.4	5.8	5.0		1.8
100 m RMS slope, deg	3.0	2.3	1.9	2.1		1.9	3.3	2.9		1.0
5 m RMS slope, deg, a-dir	7.6	5.1	4.4	6.0	1.8	1.7–3.3	3.7 Cr Plns ~10 ColHills	4.9–5.1	1.6	5.1
3.5 cm radar RMS slope, deg						0.9 ± 0.2	4.7 ± 1.6	4.7 ± 1.6	2.0 ± 0.3	4.7 ± 1.8
3.5 cm radar reflectivity						0.05 ± 0.02	0.04 ± 0.02	0.05 ± 0.01	0.06 ± 0.01	0.04 ± 0.03
IRTM I, SI, mean ± SD	360	335	364	373 ± 41		319 ± 5	284 ± 0	434	338 ± 14	355
Range				343–401		314–326	284–284	396–533	321, 355	330–360
n	1	1	1	2		4	4		16	
Lander value						315	28	434	338	355
TES I, SI, mean ± SD (Mellon)	426 ± 77	407 ± 69	456 ± 67	306 ± 28		230 ± 18	286 ± 35	418 ± 36	242 ± 16	320 ± 15
Range	368–537	276–511	369–523	273–356		194–256	216–325		192–292	
n	4	7	6	7		32	27	512	450	570
Lander value						256	256	400	203	302
TES I, SI, mean ± SD (Christ.)	334 ± 45	323 ± 31	361 ± 16	291 ± 13		215 ± 13	239 ± 20	387 ± 29	246 ± 14	288 ± 9
Range	275–412	295–388	338–383	277–315		187–252	200–275	338–460	176–291	264–333
n	8	8	8	8		32	27	288	287	287
Lander value						223	248	376	250	284

Table 13 (*Continued*)

Site	Eberswalde	Gale	Holden	Mawrth	Phoenix	Opportunity	Spirit	MPF	VL2	VL1
TES I, SI, mean ± SD (Putzig)	418 ± 80	374 ± 32	423 ± 47	358 ± 44		189 ± 29	271 ± 56	393 ± 49	242 ± 22	292 ± 29
Range	239–591	313–457	318–567	279–509		112–248	117–388	278–681	131–314	181–576
n	44	44	44	44		183	164	1774	1790	1784
Lander value					200	222	300	386	234	283
THEMIS I, mean ± SD (Ferg.)	575 ± 150	365 ± 50	390 ± 25	310 ± 55						
Range	200–1400	205–555	275–550	140–530						
IRTM FC I, SI, mean ± SD	331	268	306	312 ± 11		307 ± 9	248 ± 22	338 ± 16	260 ± 12	284 ± 21
Range				301–327		297–318	230–276	317–363	238–280	260–326
n	1	1	1	4		4	4		16	
Lander value						307	248	338	260	284
IRTM albedo, mean ± SD	0.162	0.239	0.165	0.237 ± 0.007		0.138 ± 0.055	0.150 ± 0.069	0.215	0.243 ± 0.06	0.250
Range				0.228–0.243		0.090–0.190	0.090–0.211	0.19–0.23		0.23–0.25
n	1	1	1	4						
Lander value						0.194	0.236	0.215	0.254	0.250
TES albedo, mean ± SD	0.116 ± 0.001	0.242 ± 0.007	0.131 ± 0.002	0.185 ± 0.004	0.204 ± 0.002	0.171 ± 0.026	0.222 ± 0.023	0.218 ± 0.012	0.304 ± 0.012	0.255 ± 0.006
Range	0.115–0.117	0.231–0.251	0.127–0.133	0.179–0.193	0.200–0.208	0.124–0.235	0.173–0.265			
n	8	8	8	8	22					
Lander value					0.20	0.12	0.19, 0.26	0.19	0.24	0.22

Table 13 (*Continued*)

Site	Eberswalde	Gale	Holden	Mawrth	Phoenix	Opportunity	Spirit	MPF	VL2	VL1
DCI, mean ± SD	0.973 ± 0.00	0.954 ± 0.006	0.966 ± 0.006	0.969 ± 0.008		0.969 ± 0.005	0.950 ± 0.010	0.959 ± 0.008	0.947 ± 0.012	0.952 ± 0.007
Range	0.965–0.985	0.943–0.966	0.949–0.978	0.946–0.985		0.956–0.978	0.930–0.970	0.929–0.990	0.906–0.991	0.913–0.988
n	4	29	29	29		123	107	1147	1146	1146
Lander value	29					0.973	0.964	0.967	0.924	0.945
Rock abun, %, mean ± SD, IRTM	9.5 ± 2	10	11 ± 1	14 ± 5		5 ± 3	7.5 ± 1	18	17	16
Range	8–11		10–12	10–22		1–7	7–8 (bit of 3)	18–25		8–19
n	2		2	4		4	2			
Lander						∼3	8	18	17	16
Rock abun, %, mean ± SD (TES)	45 ± 7	19*	35*	27 ± 10		very low	11 ± 4	12 ± 4	13 ± 4	8 ± 5
Range	36–52			6–40						
n	6			9						
Rock abun, %, mean ± SD, HiR	6.6 ± 1.9	5.8 ± 1.4	5.0 ± 0.3	5.6 ± 0.9						
%, mean ± SD	5.4 ± 2.6	3.9 ± 3.0	0.3 ± 1.1	3.3 ± 2.7	∼3		5	10–20	30	8
Range	0–27	0–15	0–6	0–11						
n	1918	1904	1691	2283						

Table 13 (*Continued*)

Site	Eberswalde	Gale	Holden	Mawrth	Phoenix	Opportunity	Spirit	MPF	VL2	VL1
Number Rocks, mean ± SD, HiR	13.3 ± 23.8	7.7 ± 16.6	0.3 ± 1.8	3.7 ± 8.2						
Range	0–442	0–398	0–48	0–201						
n	16474	11031	14684	16616						
% Area >1 m Dia.						0.04	0.15	1	1	0.8
Rocks, mean/range						0.001–0.15	0.15–0.2	1–2		0.15–1.1

Notes: Latitude, Longitude +E is planetocentric MOLA IAU/IAG 2000 cartographic frame, positive east. MOLA elevations with respect to the MOLA geoid, measured from the center of mass (COM). 1.2 km bi-directional (bi-dir) slopes calculated as in Anderson et al. (2003). Pulse width is slope corrected data from Neumann et al. (2003). Self affine 100 m Allan deviation and RMS slope are calculated as described in Anderson et al. (2003). RMS slope at 5 m baseline from Kirk et al. (2003, 2008, 2011a, 2011b) and Beyer et al. (2003) from MOC and HiRISE stereogrammetry and photoclinometry (Cr Plns are Gusev Cratered Plains, ColHills are Columbia Hills). Radar data are 3.5 cm X-band measures of RMS slope and reflectivity as reported in Golombek et al. (2003a, 2008b). IRTM data set from P. Christensen includes bulk thermal inertia from Kieffer et al. (1977), Palluconi and Kieffer (1981), and Christensen and Malin (1988); rock abundance from Christensen (1986a); fine-component thermal inertia from Christensen (1982, 1986a, 1986b); and albedo from Pleskot and Miner (1981) at 1 or 2 pixels per degree. TES data from Mellon et al. (2000) (Mellon) and Christensen et al. (1992) (Christ.) at 8 pixels per degree and nighttime thermal inertia from Putzig and Mellon (2007) (Putzig) at 20 pixels per degree. THEMIS thermal inertia data from Fergason et al. (this issue) (Ferg.). All thermal inertia values in SI units or J m^{-2} $s^{-0.5}$ K^{-1}. TES albedo from Christensen et al. (2002) at 8 pixels per degree. Dust Cover Index (DCI) from Ruff and Christensen (2002) at 16 pixels per degree. TES rock abundance from Nowicki and Christensen (2007) at 8 pixels per degree. HiRISE rock abundance and number of rocks for MSL sites as reported in Golombek et al. (2012) for 450 m and 150 m cells, respectively. First listed HiRISE rock abundance is for landing simulations (rounded up to the next higher integer, with a 5 % minimum); second listed rock abundance is to the nearest one-tenth rock abundance with no minimum. HiRISE rock abundance for PHX from Golombek et al. (2012) and VL1, VL2, and MPF from Golombek et al. (2008a). Percent (%) area covered by rocks >1 m diameter (0.5 m high) from model size-frequency distribution curves pinned to total rock abundance as described in Golombek and Rapp (1997) and Golombek et al. (2003b). Lander data for IRTM and TES thermal inertia (Putzig), TES albedo, and IRTM rock abundance as reported in Golombek et al. (2008b). *Data point partially in the ellipse. Mean and SD from pixels (n) with >50 % area in the ellipse

landing site (0.12), but with higher thermal inertias. Mawrth (0.18) has albedo and thermal inertia similar to MPF. The landing ellipse for Gale has higher albedo (0.24), but the layers of greatest interest at the base of the mound have lower albedo (Pelkey and Jakosky 2002; Pelkey et al. 2004). The TES dust cover index (Table 13), which includes a more explicit measure of the presence of a thin dust layer (Ruff and Christensen 2002), also indicates that Holden, Mawrth and Eberswalde (all 0.97) should be as dust free as the Opportunity site (0.97), whereas the Gale landing site (0.95) should be as dusty as VL1 (0.95). The observed spectral identification of phyllosilicates at the sites is consistent with the lack of dust, as dusty regions do not show mineral identifications in thermal and infrared spectral data (Bandfield et al. 2000; Bibring et al. 2006; Mustard et al. 2008).

The bulk thermal inertia of the MSL landing sites are all comparable or higher than previous landing sites (Fig. 6, Table 13). As a result, surface materials at the MSL landing sites are expected to have no concerns of significant deposits of underdense or non-load-bearing materials (Fergason et al. this issue; Golombek et al. 2010). The thermal inertia (Putzig and Mellon 2007, nighttime) of Mawrth (358 $\mathrm{J\,m^{-2}\,K^{-1}\,s^{-1/2}}$) and Gale (374 $\mathrm{J\,m^{-2}\,K^{-1}\,s^{-1/2}}$) are comparable to that of the Pathfinder site (386 $\mathrm{J\,m^{-2}\,K^{-1}\,s^{-1/2}}$) and likely composed of moderately to highly cohesive, cemented sediments. Holden (423 $\mathrm{J\,m^{-2}\,K^{-1}\,s^{-1/2}}$) and Eberswalde (418 $\mathrm{J\,m^{-2}\,K^{-1}\,s^{-1/2}}$) both have thermal inertias slightly higher than the MPF site, and thus are dominated by highly cohesive duricrust or cemented sediments. These properties are consistent with the presence of layered sedimentary deposits at most of the MSL landing sites, many of which have scarps that exceed the angle of repose indicating well cemented layers.

9.3 THEMIS Thermal Inertia and Surface Material Maps

9.3.1 Introduction

Thermal inertia is defined as $I = (k\rho c)^{1/2}$, where k is the thermal conductivity, ρ is the bulk density of the surface material, and c is the specific heat, and represents the resistance to change in temperature of the upper 2–30 cm of the surface throughout the day. Fine particles change temperature quickly and so have a lower thermal inertia, whereas higher thermal inertia surfaces are composed of sand, duricrust, rock fragments, or a combination of these materials. Many equally plausible scenarios, such as mixtures of particles or the presence of duricrust, can result in surfaces with moderate thermal inertias. Because thermal inertia values only help constrain the surface properties, visible images from THEMIS, MOC, CTX, and HiRISE instruments are used to more definitively interpret surface materials responsible for the thermal inertia values. The method of Fergason et al. (2006a) was used to derive thermal inertia values from THEMIS infrared data shown in Fig. 7. Standard THEMIS data processing, consisting of decompression, radiometric calibration, and systematic noise removal is applied to each image (Christensen et al. 2004; Bandfield et al. 2004; Fergason et al. 2006a). Nighttime temperatures only were used because the effects of albedo and sun-heated slopes have mostly dissipated throughout the night, and the thermal contrast due to differences in particle sizes are at a maximum (e.g., Kieffer et al. 1973, 1977; Jakosky 1979; Palluconi and Kieffer 1981).

Surface material maps (Fig. 8) of the landing sites were made by supervised classification of the thermal inertia into four different units by comparing with surface materials observed in HiRISE images (Fergason et al. this issue). The lowest values of thermal inertia are on fine-grained surfaces that appear sandy or soil covered with little cohesion, such as eolian bed forms and expansive sand "sheets." Surfaces with low to intermediate thermal inertia

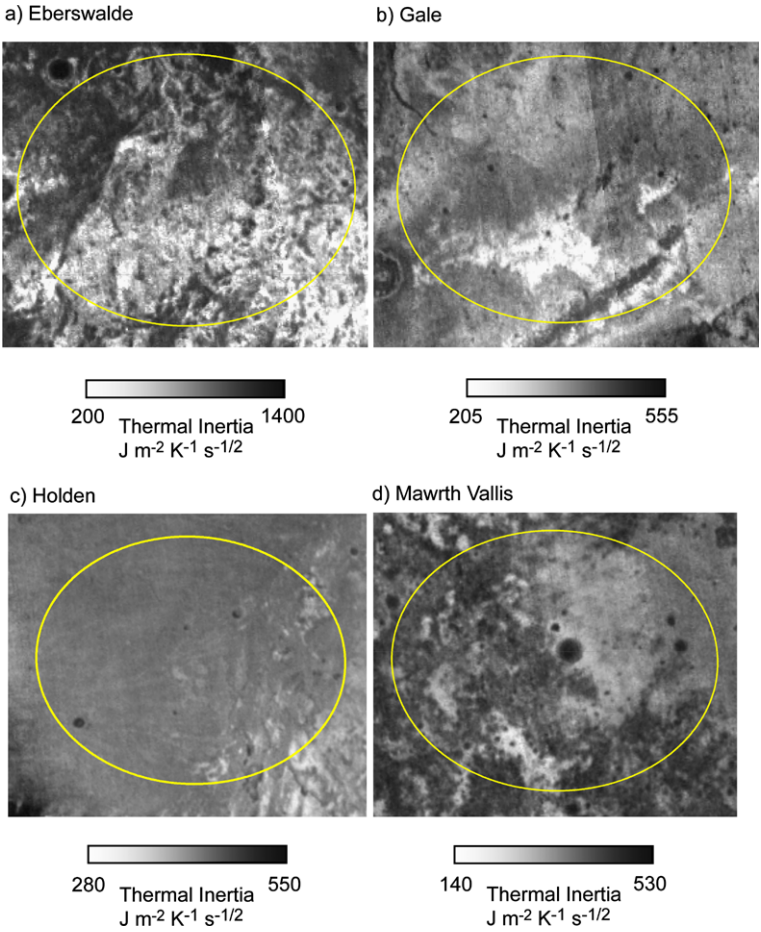

Fig. 7 THEMIS thermal inertia maps at 100 m/pixel of the MSL landing sites using the process of Fergason et al. (2006a) as described in the text and in Fergason et al. (this issue)

exhibit recognizable eolian bedforms overlying possible cemented or indurated soil surfaces or sedimentary rock. Intermediate to high thermal inertia values for the four sites correlate well with surfaces that appear to be well cemented or indurated sedimentary materials with little unconsolidated eolian cover. The highest thermal inertia values for the four sites tend to correlate with coherent rock units or cemented sedimentary surface materials.

9.3.2 Eberswalde Crater

At 100 m/pixel scale, Eberswalde primarily consists of two surface components (Fig. 7a): dark, relatively unconsolidated material and lighter, consolidated surfaces. Generally speaking, lower thermal inertia surfaces have more unconsolidated material present, typically expressed as dark deposits of eolian bed forms. Higher thermal inertia surfaces consist of more exposed bedrock or the presence of more rocky material (Fergason et al. this issue). In the surface material maps (Fig. 8a), this unit has thermal inertias of 440–500 J m^{-2} K^{-1} $s^{-1/2}$ and covers most of the ellipse. The mean thermal inertia of the landing ellipse is

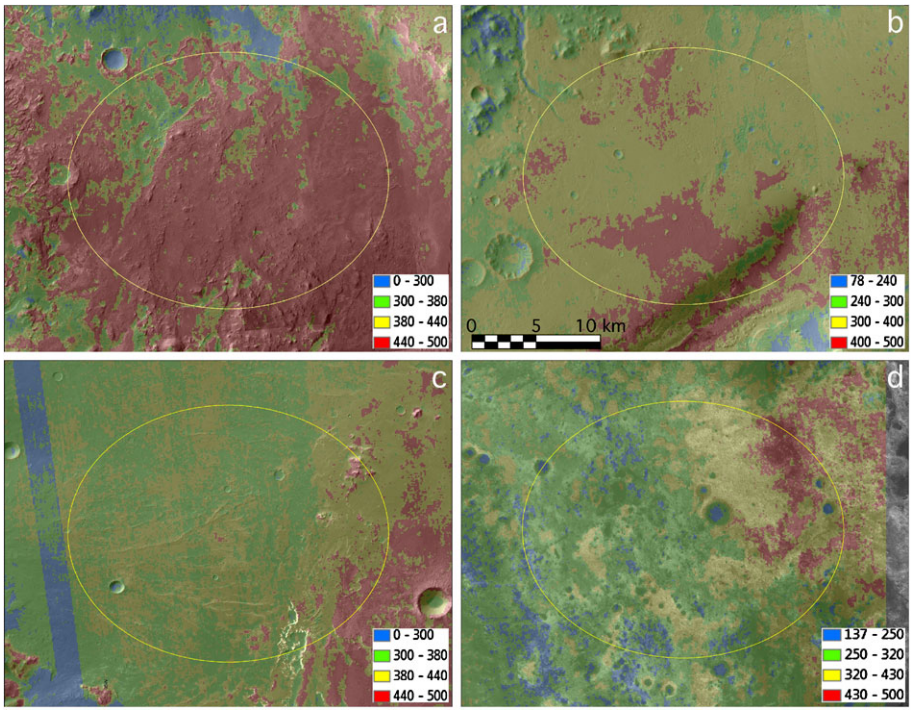

Fig. 8 Material properties maps of the MSL landing sites: (**a**) Eberswalde, (**b**) Gale, (**c**) Holden, and (**d**) Mawrth derived from supervised classification of the THEMIS thermal inertia data and materials observed in HiRISE images. See text for discussion and Fergason et al. (this issue). Low thermal inertia areas in blue are unconsolidated eolian bedforms. Areas with higher thermal inertia in green have eolian bedforms over duricrust, cemented alluvium or outcrop. Areas with still higher thermal inertia in yellow are composed of indurated alluvium, cemented sediment or outcrop. Areas with the highest thermal inertia in red are composed of indurated or cemented sediment or outcrop. Numbers are the range of thermal inertia values in each material in units of $\mathrm{J\,m^{-2}\,K^{-1}\,s^{-1/2}}$

575 $\mathrm{J\,m^{-2}\,K^{-1}\,s^{-1/2}}$ with a standard deviation of 150 $\mathrm{J\,m^{-2}\,K^{-1}\,s^{-1/2}}$ (Fig. 7a). The lowest thermal inertia value within the ellipse is 200 $\mathrm{J\,m^{-2}\,K^{-1}\,s^{-1/2}}$, and is primarily found in the interior of craters with eolian bed forms, inferred to be unconsolidated material (thermal inertia of $<$300 $\mathrm{J\,m^{-2}\,K^{-1}\,s^{-1/2}}$ in the surface material map, Fig. 8a). The thermal inertia of this unit is higher than that expected for air-fall dust and suggests that this region is primarily dust-free. Thermal inertia values as high as 1400 $\mathrm{J\,m^{-2}\,K^{-1}\,s^{-1/2}}$ are present, signifying exposed bedrock present at the surface at 100-m scales (Fergason et al. this issue).

9.3.3 Gale Crater

The mean thermal inertia in the Gale crater landing ellipse is 365 $\mathrm{J\,m^{-2}\,K^{-1}\,s^{-1/2}}$ with a standard deviation of 50 $\mathrm{J\,m^{-2}\,K^{-1}\,s^{-1/2}}$ (Fig. 7b). The lowest thermal inertia is 205 $\mathrm{J\,m^{-2}\,K^{-1}\,s^{-1/2}}$, and is found infilling small craters and also in the southern floor of the ellipse. This corresponds to the surface material map unit with thermal inertia $<$240 $\mathrm{J\,m^{-2}\,K^{-1}\,s^{-1/2}}$ (Fig. 8b) and corresponds to poorly consolidated eolian bed forms, with little dust (Fergason et al. this issue). The highest thermal inertia value observed is 555 $\mathrm{J\,m^{-2}\,K^{-1}\,s^{-1/2}}$ indicating there are no bedrock exposures at 100 m scales. This higher

thermal inertia surface typically has a scoured appearance with little unconsolidated material present, and may be well-indurated material or altered bedrock (Fergason et al. this issue). The majority of the ellipse has a moderate thermal inertia (300–400 J m^{-2} K^{-1} s$^{-1/2}$), which appears to be an indurated surface with unconsolidated materials present (Fig. 8b). A standard deviation of 50 J m^{-2} K^{-1} s$^{-1/2}$ indicates that this surface is very uniform with little variation in the surface properties; observations of surface properties from visible images confirm this interpretation (Fergason et al. this issue).

9.3.4 Holden Crater

The mean thermal inertia within the Holden crater landing ellipse is 390 J m^{-2} K^{-1} s$^{-1/2}$ with a standard deviation of 25 J m^{-2} K^{-1} s$^{-1/2}$ (Fig. 7c). The minimum thermal inertia value is 275 J m^{-2} K^{-1} s$^{-1/2}$. This value is higher than what is expected for surface dust, and suggests that the surface is relatively dust-free. The lower thermal inertia material (<300 J m^{-2} K^{-1} s$^{-1/2}$ in Fig. 8c) is limited to the interiors of some craters with pervasive bed forms (Fergason et al. this issue). The maximum thermal inertia value within the ellipse is 550 J m^{-2} K^{-1} s$^{-1/2}$, signifying that there is no bedrock exposed at the surface at the 100 m scale. These surfaces are consistent with indurated material and the presence of layered strata that must be cemented (Fergason et al. this issue). As indicated by the low standard deviation, the majority of the Holden ellipse has a consistent thermal inertia and surface material, and mainly consists of bed forms (mostly ripples) with cohesive soil beneath. Most of the ellipse is covered by surfaces with thermal inertia of 300–440 J m^{-2} K^{-1} s$^{-1/2}$ (Fig. 8c), which argues that the soil beneath the bed forms is well cemented and/or that in some cases the bed forms are indurated or are composed of grains larger than sand (Fergason et al. this issue).

9.3.5 Mawrth Vallis

Mawrth Vallis has the most thermophysical diversity of any of the four landing sites. The relationship between thermal inertia and surface texture or properties is not as straightforward as the other locations. Within the Mawrth Vallis landing ellipse, the mean thermal inertia is 310 J m^{-2} K^{-1} s$^{-1/2}$ with a standard deviation of 55 J m^{-2} K^{-1} s$^{-1/2}$ (Fig. 7d). The lowest thermal inertia value is 140 J m^{-2} K^{-1} s$^{-1/2}$, and the lowest inertia material unit (<250 J m^{-2} K^{-1} s$^{-1/2}$) corresponds to surfaces dominated by eolian bed forms (Fig. 8d) and thus is likely unconsolidated sediment, some of which may be dusty (Fergason et al. this issue). The highest thermal inertia value found in the ellipse is 530 J m^{-2} K^{-1} s$^{-1/2}$, and signifies that exposed bedrock is not present at the surface at 100 m scales. Although, it is likely (based on observations from visible data) that exposed bedrock is present at sub-THEMIS scales. The highest thermal inertia surface material (>430 J m^{-2} K^{-1} s$^{-1/2}$) corresponds to a dark capping unit with steep sides (Fig. 8d), suggesting a very well indurated unit that overlies exposed light-toned sedimentary rock with intermediate thermal inertias (250–430 J m^{-2} K^{-1} s$^{-1/2}$). Dark unconsolidated sand appears limited to small patches filling cracks in this unit (Fergason et al. this issue).

9.4 Rocks

9.4.1 Introduction

Rocks and rock size-frequency distributions were measured in the northern plains using software that segmented shadows cast in HiRISE images (Golombek et al. 2008a) and this technique correctly predicted the distributions measured by the Phoenix lander (Heet et al. 2009;

Golombek et al. 2012). The automated rock detection algorithm fits ellipses to shadows and cylinders to the rocks, and accurately measured rock diameter and height (within 1–2 pixels by comparison to spacecraft of known size) of ~10 million rocks over >1500 km^2 of the northern plains (Golombek et al. 2008a). Results show that the size-frequency distributions of rocks >1.5 m diameter are fully resolvable in HiRISE images of the northern plains, follow exponential models developed from lander measurements of smaller rocks (Golombek and Rapp 1997; Golombek et al. 2003b), and are continuous with rock distributions measured at the landing sites (Golombek et al. 2008a). As a result, HiRISE resolves the same population of rocks above 1.5 m diameter seen in lander images and thus size-frequency distributions can be accurately extrapolated along model curves to estimate the number of rocks at smaller diameters (Golombek et al. 2008a, 2012).

9.4.2 Improved Rock Mapping Techniques

Enhancements to the rock mapping techniques were motivated primarily by the considerable increase in the complexity and diversity of the terrain in the proposed MSL landing sites (full description in Golombek et al. 2011a, 2012). Because the HiRISE images have very high signal to noise ratios, straightforward blind deconvolution was used to sharpen the blurry edges of rock shadows that result from inherent imperfections in the optics (Biggs and Andrews 1997). The techniques iteratively blurs the original image and uses the difference between the two to update the restored image until it has the highest probability of being correct using a Maximum Likelihood Estimator (Holmes et al. 1995). The deconvolution process was applied uniformly in four iterations to the images by initializing the point-spread function to a 7 × 7 Gaussian kernel that approximates the point-spread function of the HiRISE camera (Kirk et al. 2008). After deconvolution sharpening, shadows as small as 3 pixels (~0.24 m^2) were detected and mapped in contrast to northern plains images in which shadows >5 pixels were mapped. In addition, each image was partitioned into eight equal sections to better tune shadow segmentation to image contrast, blur and noise, which resulted in improved detection results at sites with increased local or broader albedo variation. Finally, to eliminate detections of large shadowed escarpments and other non-rocks, which skewed the cumulative size-frequency curves, the number of rocks 2.25–1.5 m diameter was found to match the model distribution best and was used to determine the model cumulative area covered by rocks for each 450 m by 450 m area.

9.4.3 Rock Maps and Data

Maps and data provided for incorporation into landing simulations include: diameter, height and location of every rock detected in 150 m by 150 m tiles; summary size-frequency distributions in 450 m by 450 m areas, the cumulative number of rocks/m^2 >1.5 m diameter, and the best fit model distributions from the number of rocks/m^2 1.5–2.25 m diameter; and maps of the total number of rocks per tile and best fit cumulative fractional area model rock abundance (Fig. 9). Maps of the total number of rocks in 150 m tiles vary from 0 to 442, with averages of 0.3 to 13.3. Holden is the most rock free site (mean 0.3 rocks per tile). Most of Mawrth has less than 4 rocks per tile (mean 3.7 rocks per tile). Gale and Eberswalde are rockier (means of 7.7 and 13.3 rocks per tile, respectively). The relationship between the number of rocks in each tile, the cumulative area covered by rocks, and the probability of encountering one rock larger than 1.1 m diameter over a 4 m^2 area (the area of the belly pan out to the wheels) and one rock larger than 1.2 m diameter over a 2.682 m^2 area (the area of just the belly pan) on landing for two different simulations (Sect. 2.4) is shown in Table 14.

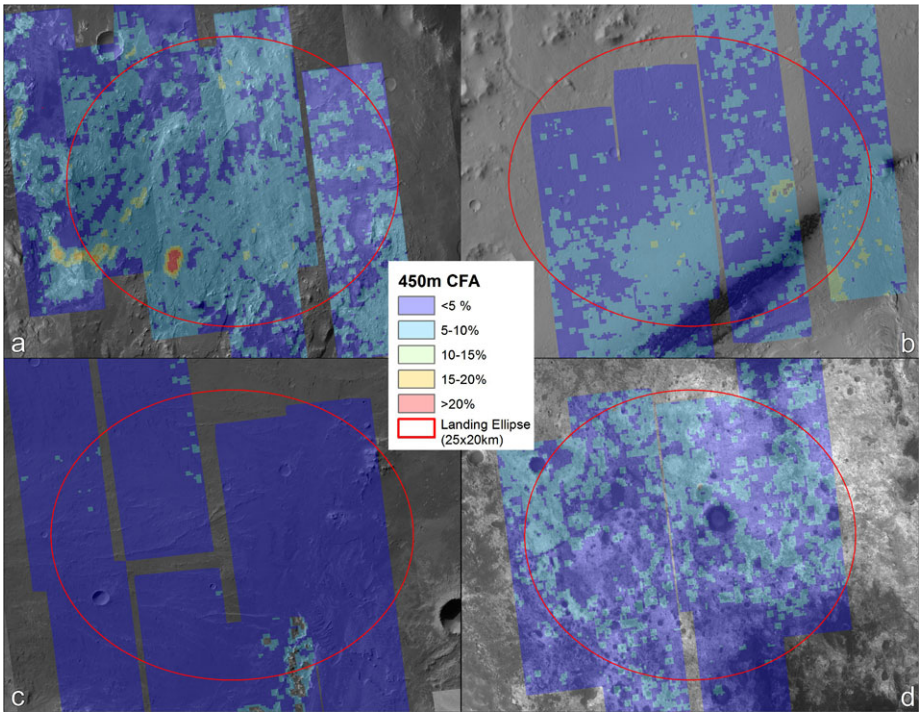

Fig. 9 Rock abundance maps of the final four MSL landing sites: (**a**) Eberswalde, (**b**) Gale, (**c**) Holden, and (**d**) Mawrth. Rock abundance is derived from rocks measured in HiRISE images in 450 m square areas fit to model cumulative size-frequency distribution for rocks 1.5–2.25 m diameter, sampled every 150 m (Golombek et al. 2011a, 2012). Cumulative fractional area covered by rocks is less than 10 % for most of the landing ellipse areas

Table 14 Number, cumulative fractional area covered by rocks, and probability of landing on 1 rock greater than given diameter

Rock density	Total number of rocks in 150 m tile	Total number of 1.5–2.25 m diameter rocks in 450 m bin	Equivalent cumulative fractional area (%)	Probability rover[a] lands on 1 rock >1.1 m diameter (%)	Probability belly pan of rover[b] lands on 1 rock >1.2 m diameter (%)
High		669	30	5.93	2.78
	>100	>321	>21		
Medium-High	21–100	171–320	<20	3.15	1.42
Medium-Low	9–20	57–170	<15	1.85	0.82
Low	4–8	4–56	<10	0.75	0.31
Very Low	0–3	1–3	~5	0.08	0.027

[a]Assumes 4 m^2 area under rover out to the wheels

[b]Assumes 2.682 m^2 area under just the belly pan of the rover

Two fits of the cumulative fractional area covered by rocks 1.5–2.25 m diameter in 450 m by 450 m grids were produced (Golombek et al. 2012). For the landing simulations, all rock abundances were rounded up to the next integer, and 1 rock was assumed as a minimum in all bins, which is equivalent to 4.1 % rock abundance—rounded up to 5 %. The second fit was to the closest one-tenth rock abundance with no minimum and thus is a more accurate measure of the actual rock abundance (Golombek et al. 2012).

The best-fit cumulative fractional area covered by rocks at the landing sites is shown in Fig. 9. These maps fit the rocks 1.5–2.25 m diameter in 450 m by 450 m grids spaced every 150 m to the size-frequency rock model according to the first method described above and explained in detail in Golombek et al. (2011a, 2012). Of the final four landing sites, Eberswalde has the highest rock abundance and Holden has the lowest. Eberswalde has broad tracks of the ellipse covered with 5–10 % cumulative fraction area covered by rocks (mean 6.6 ± 1.9 %). It also has the highest concentration of rocks in small areas covered by 27 % rocks. Holden has most of the ellipse effectively free of rocks (mean 5.0 ± 0.3 %), although some areas in the "go to" troughs to the southeast have higher rock abundances (up to 11 %). Gale is also somewhat rocky with broad tracks with 5–10 % area covered by rocks (particularly in the southern part of the ellipse), with a mean of 5.8 ± 1.4 % and a maximum of 15 %. Mawrth has most of the ellipse covered by a patchwork of <5 % and 5–10 % area covered by rocks (Fig. 9) with a mean of 5.6 ± 0.9 % and a maximum of 11 %. Using the second method the mean rock abundance in the landing ellipses is lower and 5.4 ± 2.6 %, 3.9 ± 3.0 %, 0.3 ± 1.1 % and 3.3 ± 2.7 % at Eberswalde, Gale, Holden and Mawrth, respectively.

9.4.4 Discussion

Average rock abundances of 4–5 % for Eberswalde and Gale compare favorably to the rock abundances at the Gusev cratered plains (the landing site has a rock abundance of around 5 %; Golombek et al. 2006b). The average rock abundance of around 3 % for Mawrth Vallis is similar to the Phoenix landing site (Golombek et al. 2012). Thermal differencing rock abundance estimates from IRTM (1 pixel per degree) and TES (8 pixels per degree) for the landing sites are higher than those measured in HiRISE images. IRTM rock abundance estimates average 10 %, 10 %, 11 %, and 14 % (Christensen 1986a) for Eberswalde, Gale, Holden, and Mawrth, respectively. TES rock abundance estimates (Nowicki and Christensen 2007) are less continuous and even higher, averaging 45 %, 19 %, 35 %, and 27 % for Eberswalde, Gale, Holden, and Mawrth, respectively (although TES data for Gale and Holden are from the edge of the ellipses). This discrepancy can be explained by the preponderance of layered outcrop at the sites, which would appear as rock thermally, but not as individual rock hazards, for which the size-frequency model distributions were developed.

Bulk rock abundances of <8 % indicate the probability of encountering 1 rock higher than the 0.55 m (corresponding to a 1.1 m diameter rock) under the rover during touchdown is <0.5 % (using the method in Golombek et al. 2003a, 2008a, 2012) and thus meet the engineering criterion for safe landing. The probability of landing on rocks higher than 1.1 m and 1.2 m diameter over 4 m^2 and 2.682 m^2 areas is 0.75 % and 0.31 %, respectively, for a surface with 8 % rock abundance. The convolved probability of landing at a particular point in the ellipse with the probability of failure due to landing on a rock >1.2 m diameter over 2.682 m^2 is 0.30 %, 0.17 %, 0.03 % and 0.08 % at Eberswalde, Gale, Holden, and Mawrth landing sites, respectively, and thus meet the engineering constraint of <0.5 % failure at the landing site (Golombek et al. 2012).

9.5 Slopes and Relief

9.5.1 Slopes and Relief at 0.1 & 1 km Length Scale

Relief <100 m over length scales of 0.01–1 km is important to ensure proper control authority and fuel consumption during powered descent and was evaluated using MOLA data initially and later the combined HiRISE DEMs (see next section). The most stringent of the 100 m relief constraint is at the greatest length scale (1 km), because this is the lowest slope at the greatest length scale. The MOLA elevations in the equatorial region of Mars are averaged over 463 m squares, so slopes were calculated over 9 pixels (3 by 3) to get the slope at 926 m length scale, binned to show the equivalent relief at <40 m (2.47°), 40–80 m (2.47°–4.94°), 80–100 m (4.94°–6.16°), 100–120 m (6.16°–7.38°), and over 120 m (>7.38°). Bi-directional relief at ~900 m spacing (the relief between 4 MOLA shots along an individual track) was also determined and plotted in the same relief bins. Results are shown in Fig. 10 and 900 m relief statistics are shown in Table 13. All of the ellipses are relatively smooth at the ~1 km scale, with most surfaces showing relief of <40 m. Most of the ellipses also show some areas with relief up to 40 m. Eberswalde and Gale ellipses also have small areas that exceed 80 m (6 out of 747 and 8 out of 770 measurements, respectively) and very small areas that exceed 100 m (4 out of 747 and 4 out of 770 measurements, respectively). Using the 900 m mean bi-directional relief as a metric at this length scale, Holden is the smoothest (8.0 m), followed by Mawrth (14.2 m), with Gale (18.5 m) and Eberswalde (18.7 m) much rougher.

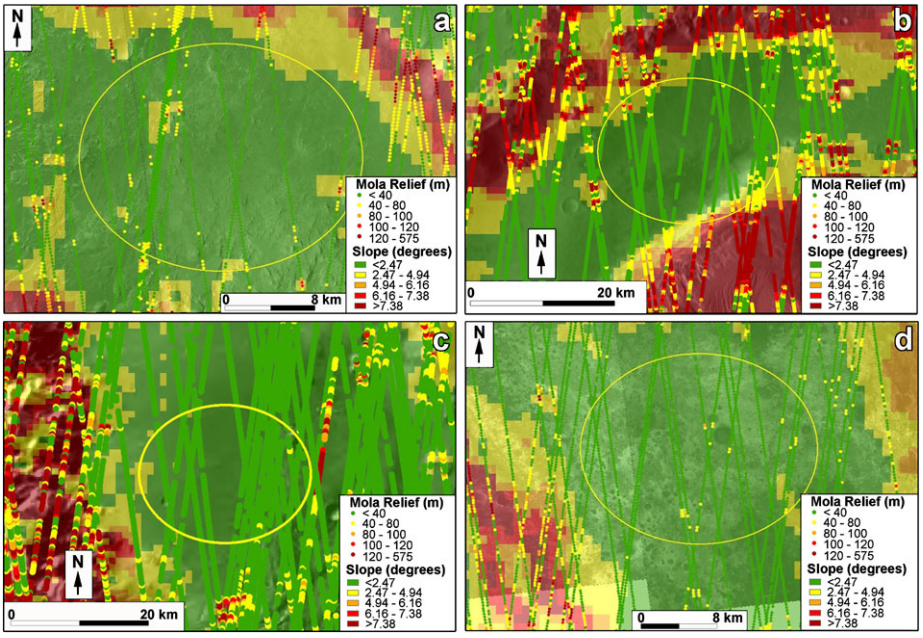

Fig. 10 MOLA slope and relief at the MSL landing sites: (**a**) Eberswalde, (**b**) Gale, (**c**) Holden, and (**d**) Mawrth. Maps show MOLA binned slope in the background with bi-directional MOLA relief at 900 m length scale overlain. MOLA binned elevations are averages in 463 m bins in the equatorial region and the slopes are binned to show the relief at 926 m length scale in 20 m increments between 40 m and 120 m. The relief constraint at 0.9 km derives from having control authority and enough fuel during powered descent, with 100–130 m relief being the maximum allowable

For comparison to other landing sites, the 1.2 km bi-directional slope along MOLA tracks was also calculated using the method described in Anderson et al. (2003). The mean slope (±SD, standard deviation) is included in Table 13 and confirms that Holden (0.49°) is the smoothest, followed by Mawrth (0.84°), with Eberswalde (1.14°) and Gale (1.23°) the roughest. All of the MSL sites are substantially rougher at this length scale than previous landing sites, which range from the smoothest at Opportunity (0.15°), to Spirit (0.2°) to VL1, VL2 and MPF (0.25°–0.29°). Even Holden, the smoothest of the MSL sites is about twice as rough as the roughest previous sites. Mawrth is about three times as rough and Eberswalde and Gale are about 4 to 5 times as rough.

Slopes at 100 m length, which could spoof the last radar measurement before airbag inflation for MER, were important for that landing site selection. Because individual MOLA shots are spaced about 300 m along a track, no direct measure of 100 m slopes could be made. To estimate relief and slopes at this scale, the MOLA pulse width and the relief at 100 m was extrapolated from that 0.3 to 1.2 km using the Allen deviation and Hurst exponent, assuming self-affine statistics (Anderson et al. 2003). In addition, the MOLA pulse spread is a measure of the RMS relief within the ∼75 m diameter laser spot after removal of regional slopes (Neumann et al. 2003). Garvin et al. (1999) and Smith et al. (2001) suggest RMS pulse spreads of <2 m have relief of <10 m over the shot point. Using the slope corrected data of Neumann et al. (2003), Holden is the smoothest ellipse (1.35 m), with Mawrth, Gale and Eberswalde much rougher (∼2 m) (Table 13), although the standard deviations are large so most ranges overlap. Holden is similar in extrapolated RMS roughness at ∼100 m length scale (1.9°) to Opportunity (1.9°), with Mawrth and Gale (∼2.1° and 2.3°, respectively) slightly rougher, and Eberswalde (3.0°) the roughest and comparable to Spirit (3.3°) and Pathfinder (2.9°). All of the MSL sites appear to be within the engineering constraint at this length scale (100 m).

To ensure proper control authority during powered descent, the relief at 1–1000 m scale must be less than 100–130 m (Sect. 2.3). The mosaiced DEMs (see next section) for each site were also used to assess terrain relief at the 1–1000 m scale. At each DEM posting, the maximum relief was determined for all elevation postings within 1000 m (Fig. 11). Sampling the DEM in this way approximates the worst-case scenario where only a single TDS radar measurement is taken prior to backshell separation and then EDL proceeds with the rover ultimately touching down at the location where the difference between that single measurement and local altitude is greatest. This upper bound, however, is inconsistent with the way EDL is actually flown. Many dozens of TDS measurements are taken and the altitude estimate at backshell separation will likely be closer to the local mean ground altitude within a 1 km radius. From simulations, a probability curve was developed that spans the gap from an idealized estimate to the worst case estimate and determines the local probability of exceeding the terrain relief allocation. This allocation varies by landing site and is set at 130 m for Eberswalde and 100 m for Holden, Mawrth and Gale. Results are consistent with the MOLA results and maps in Fig. 10 and indicate a very low probability of exceeding the fuel allocation for terrain relief at the sites.

9.5.2 Slopes at the Rover Length Scale

The MSL landing site selection process, like that for past surface missions from Pathfinder to Phoenix, relied on stereogrammetric and photoclinometric ("shape from shading") analysis of the highest resolution orbital images available to estimate slopes at the scale of the lander (Kirk et al. 2003, 2008; Beyer et al. 2003). MSL is, however, the first surface mission for which 0.25 m/pixel images from the MRO HiRISE (McEwen et al. 2007, 2010)

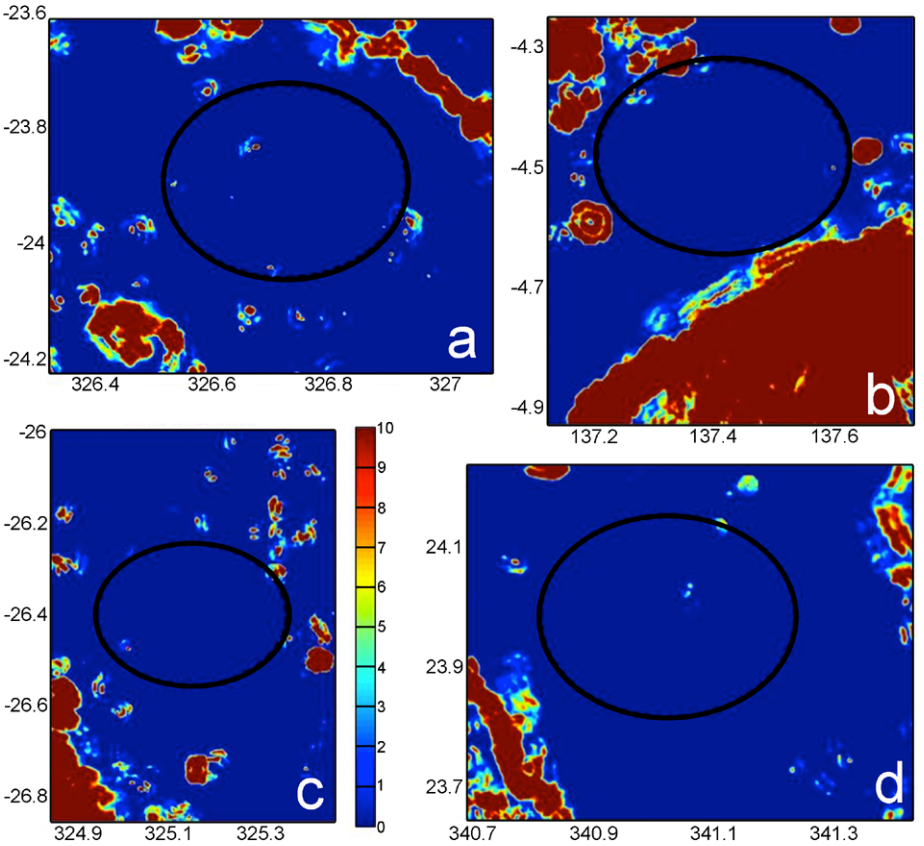

Fig. 11 Relief within 1 km at the landing sites (ellipses shown) to simulate radar performance. The maps are based on the maximum relief within 1 km at each elevation posting of each topographic map shown in Fig. 12. The scale is the probability of exceeding the fuel allocation (0–10 %) for terrain relief of 130 m at Eberswalde (**a**) and 100 m at Gale (**b**), Holden (**c**) and Mawrth (**d**). Note the close correspondence of these maps with those derived from the MOLA data in Fig. 10

have been available from the start of the selection process. Given that stereoanalysis yields DEMs with a resolution of 3 to 5 pixels at best (i.e., ∼1 m for HiRISE), photoclinometry is no longer required for its ability to measure slopes at the limit of the image resolution (as it was for MER site selection using MOC images) but remains useful for rapid reconnaissance of slopes over large areas, because it is automated and does not require stereo coverage. Beyer and Kirk (this issue) used this technique to evaluate the first HiRISE images of multiple sites early in the selection process, and to map slopes over broad areas at the Eberswalde, Gale, and Holden sites before stereo DEMs became available. Mawrth was not mapped because strong albedo variations over short distances make photoclinometry inapplicable. The photoclinometric slope estimates are generally consistent with those derived from stereo and reported below, though with greater scatter because of the sensitivity of the method to variations in surface albedo and to the accuracy with which atmospheric haze can be estimated. Eberswalde was found to be roughest, with RMS bidirectional slopes ranging from 1.5° to 8° over 2 m baseline, but even at this site, less than 0.5 % of the slopes exceeded 25°.

Stereomapping of the final four sites and samples of some earlier candidates was performed by Kirk et al. (2011a, 2011b) by the same approach developed by Kirk et al. (2008) in support of the Phoenix landing site selection. Data from the individual CCD detectors were radiometrically calibrated and "balanced" in the HiRISE Operations Center processing pipeline (Eliason et al. 2009). The USGS software system ISIS 3 (Anderson et al. 2004) was then used to remove geometric distortions and mosaic the data from the 10 red-channel CCDs into a single "ideal" image 20,000 pixels wide. Finally, the commercial software system SOCET SET (® BAE Systems; Miller and Walker 1993, 1995) was used to control each stereopair to the MOLA global DEM, produce an initial DEM by automated image matching (Zhang 2006; Zhang and Miller 1997; Zhang et al. 2006), and perform interactive quality control and editing to remove artifacts introduced in the matching step. All DEMs were produced with a grid spacing of 1 m/post (Mattson et al. 2009) and have an expected vertical precision (EP) on the order of 0.2 to 0.3 m (Kirk et al. 2008). The same software was also used to produce DEMs of the Nili Fossae and Gale sites from MRO CTX stereo images, and additional CTX DEMs were produced by the use of the NASA Ames Stereo Pipeline (Broxton and Edwards 2008), but these DEMs were not used in the landing simulations prior to selection. The CTX products have a grid spacing of 20–25 m and EP of ∼5 m as a result of the coarser ground sample distance (6 m/pixel) of the images.

HiRISE images are subject to distortion caused by spacecraft pointing variations ("jitter") while the image is being built up. The effect of spurious parallax from such jitter on slopes is negligible, but jitter in the along-track direction that exceeds about 2 pixels degrades matching accuracy or even makes image matching impossible. In the past, the only solution has been to acquire a new image or images, but Mattson et al. (2009) describe how comparison of features that appear in more than one CCD can be used to model high frequency jitter motions, allowing the distortions to be removed at the same time as optical distortions. This process was utilized for many of the MSL site images, so that repeat imaging was not necessary.

DEMs were produced from the initial stereopairs for several sites, including Mawrth 4 and Nili Fossae as well as what were later selected as the final four. Following this downselection, 21 additional DEMs were produced, yielding 75–95 % complete coverage of the 25 by 20 km ellipses as well as some science traverse or "go to" areas outside the Eberswalde, Gale, and Holden ellipses. After the Gale site was selected, an additional seven HiRISE DEMs (Table 4) were produced, filling small gaps in the landing ellipse, and extending coverage into the traverse area. Three CTX DEMs were also produced to provide a higher resolution topographic base map.

Topographic maps of the sites are shown in Fig. 12. The Eberswalde ellipse has the most rugged terrain with relief of ∼300 m (Fig. 12a) and ridges that have relief of ∼100 m. The ellipse is hemmed in by the rim of Eberswalde crater to the northeast and rugged terrain to the south and southeast. The Gale ellipse is situated on fairly low relief (<20 m) cratered plains between the crater rim to the northwest, the central mound to the southeast, and two large craters to the southwest (Fig. 12b). Some moderate sized craters are in the ellipse as well as several large hills in the eastern edge of the ellipse. The Holden ellipse is located on a gently sloping bajada surface between the Holden crater rim to the west, moderate hills to the northeast and the "go to" trough to the south-southeast (Fig. 12c). Both Holden and Gale appear relatively smooth. The Mawrth Vallis ellipse is located on fairly rugged terrain (Fig. 12d) that is positioned on the contact between Al-bearing and Fe–Mg-bearing phyllosilicates (Michalski et al. 2010a, 2010b). Total relief in the ellipse is almost 800 m, the greatest of all of the sites, but most of this occurs over long wavelengths across the ellipse.

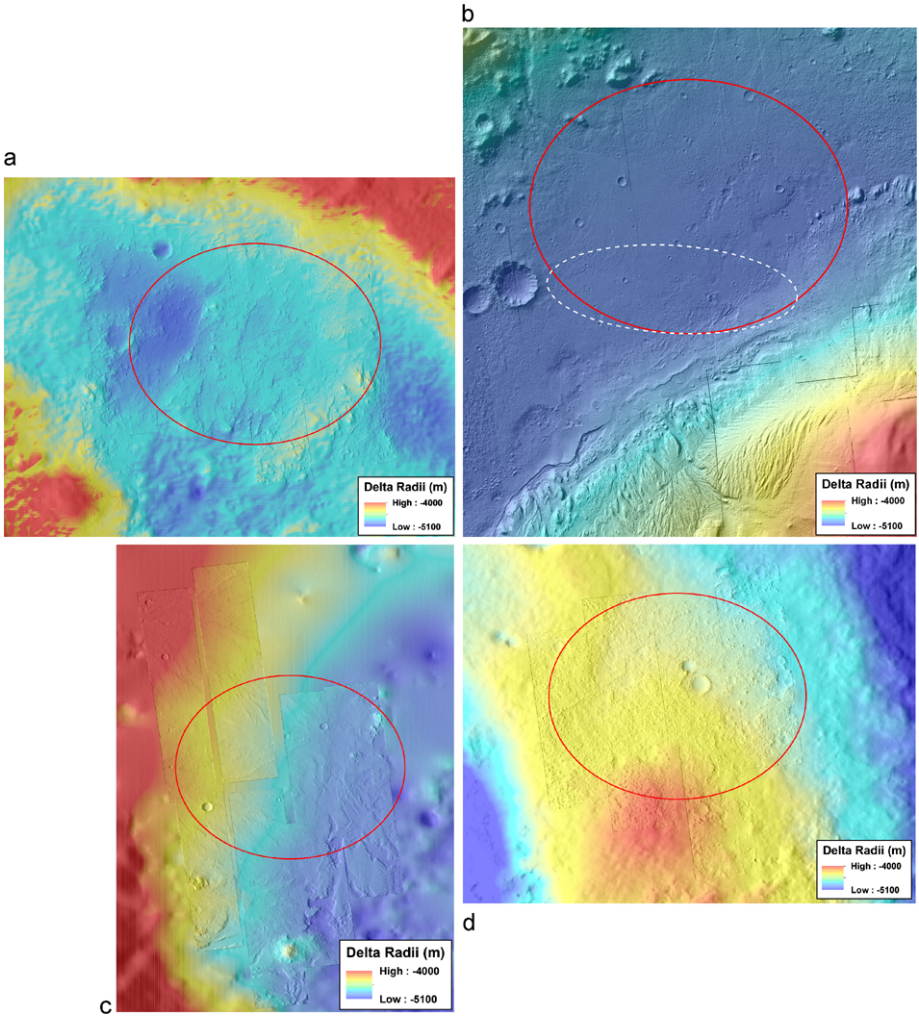

Fig. 12 Topographic shaded relief maps of the final four MSL landing sites: (**a**) Eberwalde, (**b**) Gale, (**c**) Holden, and (**d**) Mawrth. DEMs were created from individual HiRISE stereo pairs that have been placed on HRSC DEMs as described in the text. Maps are in delta radii measured from the center of mass of Mars minus the reference ellipsoid (3396190 m, which is the geoid plus the elevation). *Red ellipses* are 25 km by 20 km. Gale (**b**) also includes three CTX DEMs and a *white ellipse* (19.7 km by 6.9 km centered at 4.5965°S, 137.4019°E with long axis oriented at 93.5° clockwise from north) to which MSL has been targeted.

Of far greater concern is the short wavelength relief from ubiquitous mesas and hills (up to 30–50 m) throughout the ellipse and several moderate sized craters.

Kirk et al. (2011a, 2011b) report summary statistics for the adirectional slope at 1, 2, and 5 m (respectively the shortest baseline measurable with the DEMs and the approximate minimum and maximum dimensions of the rover wheelbase). Slopes for the individual stereopairs within each ellipse agree closely except in a few well-understood cases, notably the eastern part of Gale, which contains some rugged mounds and is therefore rougher on average than the rest of the ellipse. Here we show the statistics (Table 15) aggregated over the interior of each ellipse and the main traverse areas, as well as for HiRISE DEMs of the MER and Phoenix sites (Kirk et al. 2008). The slopes at 5 m baseline can also be compared

Table 15 Slopes of MSL final four and past landing sites at 5 m baseline

Site	Fraction of Ellipse	RMS Slope	98th %ile Slope	99th %ile Slope	Slopes >15° %	Slopes >20° %	Slopes >25° %	Slopes >30° %
Eberswalde	93 %	7.56	21.0	24.6	5.85	2.41	0.92	0.32
Eberswalde traverse		*8.88*	*22.1*	*24.8*	*10.04*	*3.42*	*0.96*	*0.27*
Mawrth 2	93 %	5.98	15.2	17.9	2.13	0.57	0.15	0.04
Gale	77 %	5.06	12.5	15.4	1.1	0.41	0.17	0.06
Gale traverse		*18.11*	*46.5*	*50.7*	*34.56*	*23.33*	*16.10*	*10.82*
Holden	86 %	4.44	11.4	14.3	0.85	0.29	0.08	0.02
Holden traverse		*6.44*	*17.2*	*20.1*	*3.32*	*1.02*	*0.29*	*0.09*
Spirit		3.73	9.8	12.0	0.36	0.05	0.01	0.00
Opportunity		3.27	8.0	9.4	0.06	0.00	0.00	0.00
Phoenix		1.85	3.8	4.3	0.00	0.00	0.00	0.00

directly to additional results for the past sites from MGS MOC images (Kirk et al. 2003, 2008). Overall RMS slopes increase from 4.4° to 7.6° in the order Holden, Gale, Mawrth, and Eberswalde. The smoothest of these sites, Holden, is similar to the cratered plains of Gusev on which Spirit landed. RMS slopes at Gale (5°) are similar to the cratered plains at VL1 and Pathfinder (Table 13). RMS slopes at Mawrth (6°) and Eberswalde (7.6°) are rougher than any of the previous landing sites, but do approach those of the Columbia Hills (∼10°) that Spirit ascended. As for all previously investigated sites (Kirk et al. 2003, 2008), the slope distributions are long-tailed (99th percentile ranges from 2.9 to 3.5 times the RMS value, compared to a theoretical value of 2.14 if the E–W and N–S slope components were normally distributed). Despite this, only 0.92 % and 0.32 % of slopes in the Eberswalde ellipse and much less in the others exceed 25° and 30° slopes, respectively, which would begin to present a landing hazard (Table 15). The Eberswalde and Holden traverse areas are somewhat rougher than their respective landing ellipses, but the central mound of Gale crater is extraordinarily rugged, with 16 % and 11 % of slopes exceeding 25° and 30°, respectively, and some as steep as 50°. Detailed analysis of the slope map of this area, combined with photointerpretation of the images to discriminate bedrock from unconsolidated sediments nevertheless shows that essentially every target of interest in the mapped portion of the central mound can be reached by an acceptable traverse (see Sect. 11).

In addition to analyzing slope statistics for individual DEMs and aggregating the results, Kirk et al. (2011a, 2011b) also produced sitewide mosaics of the DEM data, supplementing the 1 m/post HiRISE coverage with 50 m/post Mars Express HRSC DEMs (Gwinner et al. 2010a) and for the Gale ellipse three 25 m/post CTX DEMs. The HiRISE and CTX DEMs were controlled individually by photogrammetric bundle adjustment as they were produced, but the accuracy of their absolute positions is limited by the resolution of the MOLA DEM used as a reference. Additional, nonrigorous adjustments based on tie point measurements were therefore made during the mosaicking process, as described in Sect. 5.6. The CTX DEMs were found to contain substantial (∼100 m) horizontal and vertical distortions, which were traced to the optical distortion coefficients for the CTX camera (obtained from the NAIF Instrument Kernel) having the wrong sign. The horizontal distortions were removed in the process of tying the data to the HRSC orthoimages. Vertical distortions were removed by highpass filtering the difference between the CTX and HRSC DEMs and adding the results to the HRSC elevations. Vertical offsets were then applied to the HiRISE DEM values,

first to minimize the RMS difference between the overlapping HiRISE DEMs and then to a mosaic of the HiRISE DEMs to minimize its difference with respect to the HRSC or combined CTX and HRSC DEM before mosaicking it on top of the latter. These procedures yielded gap-free DEMs of each site (including the ellipse, traverse areas, and surrounding terrain) that were delivered to the MSL engineering team for use in simulations of entry, descent, and landing (Fig. 12). The main difficulty of using these models in the simulation process is the presence of discontinuities at the edges of the HiRISE coverage; although the CTX data are consistent with HiRISE on average, they cannot resolve all the features present in the latter, so jumps as large as several tens of meters occur where small features are cut by the HiRISE boundary.

As a side benefit of the adjustment and mosaicking process, the magnitude of the adjustments and the difference between overlapping HiRISE DEM segments can be used to assess, respectively, the absolute positional accuracy of individual controlled DEMs and their EP (Kirk et al. 2011a, 2011b). Absolute accuracies are on the order of 50–100 m horizontally and 10–20 m vertically, in excellent agreement with past estimates based on less definitive information such as the residual errors of the bundle adjustment itself (Kirk et al. 2008). More significantly, the EP is in the range 0.1–0.4 m, with smaller values in areas with more surface texture for the stereo matching algorithm to correlate. These height errors correspond to $\leq 2^\circ$ RMS error in the adirectional slope.

9.6 Radar Reflectivity and Roughness

X-band (3.5 cm) delay-Doppler radar observations, both single-station and interferometric, were used for landing site analysis and selection for the Mars Pathfinder (Haldemann et al. 1997) and the Mars Exploration Rovers (Golombek et al. 2003a). Similarly, the extant data were consulted regarding the four proposed MSL landing sites. A combination of gaps in the Goldstone Solar System Radar delay-Doppler observations, into which the Gale crater landing site falls, and the high, relative to terrestrial radar observations, latitudes of the other three landing sites, precludes full interferometric processing and analysis.

Analysis of the extant delay-Doppler data from the 2001, 2003, and 2005 oppositions, however, was used to screen landing sites for anomalous quasi-specular features that would indicate surface radar reflectivity outside the MSL engineering constraints (Prakash et al. 2008; Pollard and Chen 2009). Both the Holden crater and Eberswalde crater landing sites fell within the delay-Doppler observation taken on September 2, 2003. Given that the landing sites are $\sim$5.5 and 8 degrees south of the sub-radar track, the returned signal levels are significantly reduced. Longer integration of the received signal, with reduced spatial resolution from the DSS-14 telescope verified that both landing sites had radar backscatter properties typical of the Martian surface. Neither showed anomalous radar signals that would indicate unusually high or low radar reflectivities.

Similarly, the observation of May 19, 2001 was analyzed where the delay-Doppler signal contained reflections from the Gale landing site. Due to equipment errors during this observation, the site was not observed at an angle less than $\sim 6^\circ$ from normal. Thus analysis of the landing site is reduced to examination of the delay-Doppler images. Like the previously mentioned sites, there is nothing to indicate anomalous radar reflectivities that would present difficulties for the descent radar or rover trafficability.

There are no delay-Doppler data that covers the Mawrth Vallis landing site due to its high northern latitude. However, depolarized S-band (12.6 cm) Arecibo observations (Harmon et al. 1999) do provide a lower resolution site survey. As with the previously mentioned landing sites, the data shows nothing unusual and indicates an average radar return well within the engineering constraints.

10 Assessment of Landing Success

10.1 EDL Site Safety Considerations

Site-specific safety considerations for EDL can be divided into three distinct categories: (1) vehicle interactions with the local atmosphere during entry and parachute descent, (2) radar-terrain interactions during parachute descent and powered flight, and (3) rover mechanical interactions with the surface during touchdown. Due to both functional and temporal separation, EDL safety for each of these interactions can be considered in a largely independent fashion.

10.1.1 Atmospheric Interactions

As with previous Mars landers, atmospheric conditions during entry, descent, and landing directly impact the performance of MSL's EDL system (Chen et al. 2010). While the vehicle's guided entry system allows it to "fly out" a range of atmospheric uncertainties (Brugarolas et al. 2010), its trajectory through the atmosphere creates a variety of atmospheric sensitivities not present on previous Mars entry systems and landers. The performance of the MSL EDL system is most sensitive to atmospheric bulk density, local density variations, and winds, especially during parachute descent.

Like previous ballistic entries, the MSL EDL system is highly dependent on atmospheric drag, both during entry and parachute descent, to slow the vehicle for a safe landing. Consequently, EDL performance is most strongly tied to atmospheric density and density structure. Unlike ballistic entries, MSL's guided entry results in an increase in the downrange distance flown at low altitudes (40–75 km greater than PHX and MER). MSL spends a significant fraction of the downrange distance flown at or near level flight at approximately 10–15 km altitude. Because of this, MSL's altitude and timeline performance are very sensitive to density conditions in this altitude range.

As MSL approaches the supersonic parachute deploy event (Fig. 1), the guided entry's ability to control downrange flight becomes limited. As a result, the vehicle is in open loop controlling downrange distance with only the capability to adjust heading slightly. The open loop nature of this "heading alignment" phase of guided entry presents additional atmospheric sensitivities. Any density or wind differences from the expected conditions will translate directly into elevation and landing performance variations. Lower than expected densities will reduce elevation performance and can also cause the vehicle to fly past the desired landing site. Higher than expected densities will increase elevation performance, but may cause landing short of the site. Vertical steady state winds will affect elevation performance depending on the duration of exposure. Similarly, horizontal steady state winds different than those expected will reduce landing precision and can also affect elevation performance by changing the effective drag on the entry capsule.

Wind conditions at the parachute deployment and heatshield separation events also present key performance sensitivities. Both events are sensitive to Mach number: parachute inflation and drag performance depend on the Mach number; heatshield separation safety is impacted by the Mach number due to reduced parachute drag (Kipp et al. 2007). Winds directly impact the true Mach experienced at both events. Because MSL utilizes inertially propagated navigation velocity triggers for both parachute deployment and heatshield separation and lacks the ability to sense instantaneous wind speeds, variations in winds from the expected condition increase the spread and distribution of Mach number at these events.

As with previous missions, wind deviations from those expected during the parachute descent phase add additional landing error. Steady state wind differences from the expected

winds cause position drift on the parachute. The vehicle has no ability to combat the wind drift while on the parachute and lacks sufficient propellant to correct for any drift during powered descent. Thus, an understanding of the steady state winds during parachute descent is essential in assessing landing precision, especially for lower elevation sites where the time on the parachute is greater.

10.1.2 Radar Terrain Interactions

The MSL Terminal Descent System (TDS) begins operating shortly after the heatshield separates and generates measurements of the spacecraft's surface relative altitude and velocity for the remainder of EDL. The TDS is comprised of six individual radar transmit/receive modules that are body-fixed at different orientations (aligned 0°, 20°, and 50° from the vehicle axis of symmetry) in order to acquire distributed measurements across the surface. Given that the Martian surface will almost certainly be non-planar, each consecutive measurement will yield a slightly different measurement of the local surface altitude and an on-board navigation filter is used to combine measurements and produce a single estimate of the landing site altitude.

The navigation filter has no information regarding where the vehicle will ultimately land, and is reliant upon a distributed set of terrain measurements taken at locations some distance removed from the touchdown location. Altitude solutions produced at high altitudes, when the radar beams are measuring altitude relative to terrain that is farther away from the touchdown location, will invariably be 'wrong' to some degree. The degree of 'wrongness' is a function of local terrain relief over a ∼2 km baseline and will decrease gradually as the vehicle approaches the surface and the radar beams measure terrain closer to the touchdown location (Kipp 2012). MSL's powered descent profile is designed to accommodate these altimetry errors through the use of two altitude "accordions" which are flown at a constant velocity for variable duration until a target altitude is reached.

The first accordion, designed to correct altitude estimation errors from backshell separation, begins after the vehicle has separated from the backshell and performed powered approach. At the end of powered approach, the vehicle will have decelerated to 32 m/s vertical velocity and 0 m/s horizontal velocity and will be directly above the touchdown location at an altitude of between ∼150 m and ∼350 m. During the first accordion, the TDS continues taking measurements and the spacecraft continually updates its onboard altitude. These altitude estimates are continually improving as the TDS is now measuring terrain in closer proximity (within 150 m) to the landing location. The spacecraft will spend between 0 and 6 seconds descending vertically at a constant velocity until it reaches an altitude of ∼150 m. After reaching this target altitude the first accordion is completed.

The first accordion is sized to consume anywhere from 0 m to 200 m of altitude in order to "fly out" altimetry errors of up to ±100 m. Terrain relief exceeding 100 m over a ∼1 km baseline can result in EDL failure. If the altitude solution at backshell separation is over 100 m too low, then the first accordion saturates at 0 m and the vehicle is at risk of impacting the surface before the sky crane phase begins. Conversely, if the altitude solution is over 100 m too high, then the vehicle is at risk of running out of fuel due to exceeding the amount of fuel allocated for the first accordion.

The second accordion, designed to correct altitude estimation errors from the beginning of the sky crane phase, begins after the rover is ready for touchdown. At this point the rover is descending vertically at 0.75 m/s at an altitude of ∼0 to ∼6 meters. The vehicle continues to descend vertically at constant velocity until the rover touches the surface and the second accordion is completed.

The second accordion is sized to consume anywhere from 0 to 6 m of altitude in order to "fly out" altimetry errors of up to ±3 m. Terrain relief exceeding 3 m over a ∼10 m baseline can result in EDL failure. If the altitude solution at the beginning of the sky crane phase is over 3 m too low, then the vehicle will encounter the surface before it is mechanically configured for touchdown. If the altitude solution at the beginning of the sky crane phase is over 3 m too high, then, as with the first accordion, the vehicle is at risk of running out of fuel.

10.1.3 Surface Terrain Interactions

Because EDL is designed to begin the sky crane phase at carefully controlled conditions (altitude and velocity), the landing event is effectively decoupled from atmospheric dispersions (winds, temperatures, density, etc.) and the safety of touchdown is driven entirely by the local terrain. *Curiosity* will be placed on the surface in its ready-for-touchdown or surface ready configuration. In this configuration the rover's six wheeled surface-mobility system is deployed and will encounter the surface at a gentle 0.75 m/s. Because the mobility system was designed to handle large rocks and slopes during the surface mission, it is an inherently capable landing system and can safely tolerate slopes (up to 30°) and rocks (up to 0.6 m high). Touchdown failures can occur when the combination of local rocks and slopes exceeds the stability limit of the rover or when a rock is encountered that exceeds its ground clearance and impinges on the rover's belly pan. Belly pan strikes can result in a high-centered rover that is unable to traverse, internal damage to the rover, or both.

10.2 Assessment of EDL Success

Overall EDL success probabilities are determined by a two-step process. The first step is to assess entry and descent success via Monte Carlo simulations, and the second is to assess touchdown success via the use of hazard maps that define the probability of successful touchdown at each location within a landing ellipse (Kipp 2012).

10.2.1 Entry and Descent Success Assessment

Entry and descent success is assessed via Monte Carlo simulation of several thousand EDL scenarios, referred to as 'cases', using the primary MSL EDL performance verification simulation, built within the Program to Optimize Simulated Trajectories (POST) (Way et al. 2007). This program is the highest fidelity environment used to simulate end-to-end EDL trajectories. The simulation incorporates the MSL EDL flight software and includes detailed, and generously dispersed models of the vehicle's initial state prior to entry, the vehicle's mass properties, the vehicle's aerodynamic properties, and all of the vehicle's critical sensors and actuators. In addition to these detailed system models, the landing site environments are modeled in the simulation as well. The simulation incorporates dispersed atmospheric conditions derived from site-specific mesoscale atmosphere models (Chen et al. 2010) and simulates the surface using the highest resolution rock maps and DEMs available. For each simulated EDL scenario, over 5000 individual variables are stored to represent the state of the vehicle at key times during the EDL sequence of events. These stored variables are post-processed to determine system margins and identify any out-of-specification cases that violate predetermined EDL flight rules. Any EDL scenario that includes even a single out-of-specification parameter is flagged and identified as a potential failed case. Taking the percentage of flagged cases provides an assessment of the entry and descent success probability at each landing site.

Table 16 Touchdown capability and failure rate

Touchdown Capability	Failure Rate %
Slope Tolerance °	
<24	0
24–30	1
30–35	12
Rock Tolerance Rock Abundance %	
5	0.03
10	0.31
15	0.82
20	1.43
25	2.09
30	2.78
>30	100
Inescapable Hazards	100

10.2.2 Touchdown Success Assessment

Because the end-to-end simulation does not model the touchdown event in high fidelity, a second step is necessary to determine the probability of successful touchdown. Touchdown hazard maps, which define the local probability of successful touchdown at any location on the surface were generated by considering the local terrain and the capability of the rover to handle the terrain during touchdown. Touchdown capabilities on rocks and slopes were determined via a series of tests and test validated analyses (White et al. 2012) summarized in Table 16. Many potential failure modes were considered including sky crane engine plume interactions with the local terrain, terrain-induced touchdown trigger spoofing, and the potential for bridles to damage hardware on the rover's top deck. Additionally, the post-touchdown state of the rover was considered inasmuch as the rover must be left in a safe orientation and location for surface operations to begin. After assessing each of these failure modes, it was determined that slope tolerance is primarily limited by the stability and structural loading of the rover during touchdown. Failures of this nature increase at slopes that exceed 30°.

During touchdown the vehicle is tolerant of all rocks that safely fit under the rover's belly pan at 0.6 m height. The combined effect of encountering slopes with rocks less than 0.6 m high is considered in the analysis and included in the slope tolerance numbers (Table 16). Assuming hemispherical rocks, rocks larger than 1.2 m in diameter will pose a hazard to the belly-pan at touchdown. Additionally, rocks larger than 2.25 m diameter will pose a threat to the mobility system. Failure rates due to local rock abundance, as given in Table 16, are calculated based on the abundance of rocks 1.2–2.25 m diameter over the 2.682 m^2 area of just the belly pan. Note that the reduced probability of encountering a potentially hazardous rock (Table 14) is due to use of a smaller footprint (2.682 m^2 versus 4 m^2) and a smaller rock diameter (1.2 m versus 1.1 m).

Armed with this knowledge of the EDL system's slope and rock tolerance during touchdown, as well as with the co-registered DEMs and rock maps, it is straightforward to calculate the local probability of a successful touchdown. For the purposes of MSL, the Martian surface was discretized into a uniform grid with 150 m cells. Rover-scale slope statistics

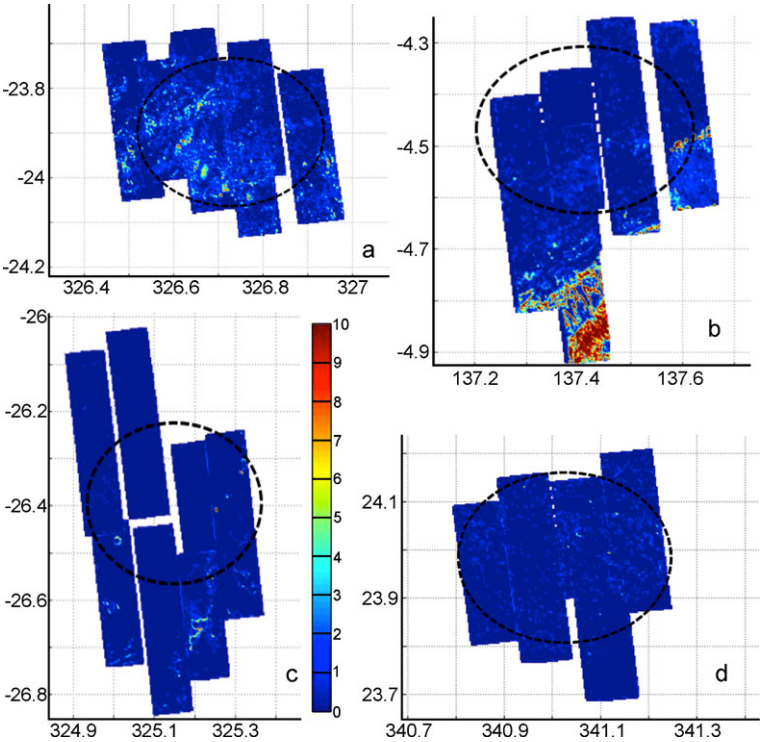

Fig. 13 Touchdown failure maps for the four MSL landing sites (ellipses shown): (**a**) Eberswalde, (**b**) Gale, (**c**) Holden, and (**d**) Mawrth. Maps show the probability of failure (0–10 %) from rocks and slopes within each 150 m cell

were derived from DEMs for each cell and local rock abundances were also determined for each cell. Each cell is then assigned an overall touchdown failure rate according to the combination of local rock abundance, local slope statistics, and the capability of the system in Table 16. Touchdown failure maps are shown in Fig. 13 for the four final sites. Not surprisingly, these maps are similar to the slope and rock maps on which they are based with areas with high rock abundance or slope having the highest probability of failure.

The final step to determine the probability of safe landing at a given location in the hazard map incorporates knowledge from the end-to-end EDL simulation. Thousands of individual simulation cases yield thousands of landing points that are combined to produce a landing probability map that gives the probability of successfully landing at each location within the site. By convolving this landing probability map with the local hazard map, the overall probability of successful touchdown can be determined.

10.2.3 Assessment Results

An 8001 case Monte Carlo simulation was run at each of the final four landing sites to enable a direct comparison of entry and descent performance between them. These simulations were run assuming no internal spacecraft faults in order to isolate site-specific risks from those risks that are internal to the system and may be present regardless of the selected site. As such, these results are not intended to represent the overall probability of EDL success,

Table 17 Out of specification landing site simulation cases for the four MSL landing sites

Parameter	Eberswalde (Number of Cases)	Gale (Number of Cases)	Holden (Number of Cases)	Marwth (Number of Cases)
Descent stage flyaway distance range <150 m	0	0	0	0
Backshell recontact (long term) range <60 m	15	0	7	4
Backshell recontact (short term) CPA <40 m	2	0	1	1
Touchdown before diff release (TD too Early) TD in mode 34	1	0	0	1
Peak heating rate exceeded (aerothermal) >225.7 W/cm^2	0	19	0	2
Touchdown rover vertical velocity exceeded >0.85 m/s	0	0	1	1
Parachute inflation loads exceeded >65,000 lbf	0	2	1	1
Peak shear exceeded (aerothermal) >538 Pa	0	1	0	0
Mortar cover recontact CPA <20 m	0	0	2	1
Entry and Descent Total	18 / 8001 (0.22 %)	22 / 8001 (0.27 %)	12 / 8001 (0.15 %)	11 / 8001 (0.14 %)
Touchdown Hazard	0.64 %	0.21 %	0.21 %	0.14 %
EDL Success	99.14 %	99.52 %	99.64 %	99.72 %

but rather to illuminate site-to-site differences in the level of EDL risk. Because each site presents different challenges for EDL, certain parameters (e.g., parachute deployment) must be tuned differently at each site. Simulations run in support of site selection were set up to approximate how EDL would be individually tuned for each site with the understanding that a detailed final tuning would only be performed at the selected site. Hence these results represent an upper bound on the number of "out-of-spec" cases at each site. These results were generated in May 2011 in support of the final landing site down-selection.

Out-of-specification cases were tracked and are summarized in Table 17. Less than 0.3 % of cases were flagged as out of specification at any site. Conversely, over 99.7 % of simulated cases performed a successful entry and descent at all sites. Landing point distributions generated from each Monte Carlo simulation were convolved with terrain hazard maps to determine touchdown failure rates due to terrain. As with entry and descent, the percent of cases subject to hazards at touchdown are less than one percent at all sites. As expected based on slopes and rocks, touchdown hazards are more likely to be encountered at Eberswalde than at the other three sites. However, the overall EDL success rate is assessed to be greater than 99 % at all sites. In addition to looking at out-of-specification cases, key EDL margins were tracked to verify adequate timeline margin, fuel margin, and acceptable time exposure to supersonic parachute descent. These metrics are indicators of EDL robustness and margins were determined to be healthy and acceptable at all four sites.

The combined entry, descent, and landing success rates across the four landing sites ranged from 99.14 % to 99.72 % (Table 17). The engineering judgement of the EDL systems team ascribed a ±0.5 % uncertainty on these results. Thus, the difference in overall assessed success rate is comparable with the level of uncertainty of the result. There is, however, an unambiguous conclusion that Eberswalde Crater, presents steeper and rockier terrain than the other sites and thus is more taxing on the EDL system. The result is that EDL robustness at Eberswalde, while still adequate, is less than the other three sites. Nonetheless,

the assessed success rates at all sites are very high compared to historical precedent and the project concluded that differences in EDL safety did not represent a significant discrimator to be used in selecting the final site.

11 Traversability of the Landing Sites

11.1 Introduction and Drive Modes

The goal of this section is to evaluate each landing site in terms of driving difficulty and duration between landing locations and science targets. MSL has been designed to traverse long distances, which has enabled the consideration of "go to" sites in which the materials of prime scientific interest are outside of the landing ellipse. This requires the rover to traverse out of the landing ellipse quickly enough to leave time for studying the target materials within the nominal mission (one Mars year). As a result, the drive duration must be factored into the site selection decision along with the potentially increased mission risk. The availability of HiRISE images and derived DEMs makes it possible to do a detailed survey of landing site traversability to a degree never possible before from orbit.

Past and current rover missions have relied almost exclusively on surface images to make tactical decisions on the selection of safe routes. The terrain ahead of the rover is evaluated by comparison with previous experience and rover performance when moving over terrain of similar slope and obstacles and hazards such as rocks, scarps, and eolian bedforms (Biesiadecki et al. 2008). On the basis of this evaluation of surfaces ahead of the rover, some features are negotiable (perhaps with varying degree of difficulty), but some can pose a serious mobility risk and need to be identified and avoided in path planning (Biesiadecki et al. 2005; Leger et al. 2005).

Obstacles that can be identified from surface or orbital imagery are either avoided by selecting a safe path (Parker et al. 2010) or by selecting a more autonomous driving mode (Biesiadecki and Maimone 2006; Biesiadecki et al. 2007). Selecting a safe path in the surface images is called "blind" driving, in which the rover is commanded to move specific distances in specific directions or to specific locations based solely on inertial measurements and wheel odometry. The rover monitors various mobility safety parameters such as vehicle attitude, suspension, and actuator currents as it drives, but does not capture any images of the surrounding terrain (hence the name of this driving mode).

Whenever the terrain coverage or image quality is insufficient, for example at great distances from the rover, operators can make use of the on-board mobility software to ensure safe operation of the vehicle. MSL flight software, like MER flight software, includes two autonomous mobility modes: Autonomous Navigation (AutoNav) and visual odometry (Visodom) (Maimone et al. 2006, 2007a, 2007b).

AutoNav is a software mode that generates a three dimensional model of the terrain near the vehicle from a stereo pair, locates potential obstacles such as rocks, troughs, steep slopes and rough terrain, and selects the safest and shortest path to the rover destination. This mode is useful to safely navigate through rugged terrain (Matthies et al. 2007a, 2007b; Maimone and Morrison 2004; Goldberg et al. 2002).

Visodom is a flight software mode that compares the position of a set of terrain features before and after the vehicle has moved by a predetermined amount and updates the rover position compensating for any vehicle slip. The mobility software constantly updates the rover position and attitude by integrating wheel odometry and inertial measurement unit data (Ali et al. 2005; Yen et al. 2005). Under normal conditions and other drive modes the

Table 18 MSL rover drive modes, their usage and estimated drive rates (including slip checks)

Drive Mode	Usage	Drive Rate
Blind	No obstacles, low-slope terrain	114 m/hr
AutoNav	Obstacles, rugged terrain, scarps	45 m/hr
Visodom	High-slope terrain, cohesionless terrain	29 m/hr
AutoNav+Visodom	Rugged, sloped terrain	20 m/hr

position estimate is quite accurate, but when the vehicle drives over unconsolidated terrain or steep slopes the vehicle slip is not taken into account so the rover position is less well known. Visodom is quite useful to ensure the vehicle has a correct representation of its position on slopes or terrain in which slip may occur. Visodom also helps ensure that the vehicle avoids pre-identified obstacles as the distance between them and the vehicle is updated during the drive (Maimone et al. 2007a, 2007b; Cheng et al. 2005, 2006).

Both AutoNav and Visodom require a lot of computational time, thereby reducing the effective speed, or drive rate, of the vehicle by almost one order of magnitude (Table 18). Here the effective speed is the distance, in meters, covered in one hour and includes both the time it takes to actually turn the wheels in addition to the image processing and computation time. Although the MSL flight software has been optimized and takes advantage of a faster processor than MER, therefore reducing the computational time of these modes, the effective vehicle speed is still a fraction of the raw vehicle speed. Raw vehicle speed is intended as the distance, in meters, covered in one hour without any image processing steps. For this reason AutoNav and Visodom are employed only when absolutely necessary to ensure safe operation of the vehicle. As a result, terrain analysis not only involves locating hazards and obstacles but also helps in selecting appropriate driving modes and flight software settings.

The MER rover drivers spend considerable time in analyzing the terrain, evaluating hazards, and designing the optimal path. While some of the factors considered in this process are difficult to quantify (for example the apparent depth of sand over bedrock), most are easily quantifiable (terrain slope, presence of rocks or eolian bedforms) as well as the selection of the most appropriate drive mode. Given the sizeable amount of terrain to be analyzed at each of the MSL landing sites, an automated process was developed to provide consistent results for planning in a reasonable time.

11.2 Data Sets

The MSL rover can negotiate obstacles larger than the MER, but otherwise in tests on Earth the two vehicles perform similarly. As a result, similar traversability criteria are applied. The most important criterion to determine if an area is traversable is the slope. MER experience indicates that wheel slip increases in cohesionless material as the slope increases to a limit of around 15°. MER successfully drove up slopes as high as ∼30° on outcrop. HiRISE derived digital topographic maps with 1 m elevation postings (see Sect. 9.3.3) were used to determine the slope at the rover scale (2 m). The rock maps were also used to determine the type of driving that can be done and to avoid rocks higher than the belly pan (0.6 m). The location and size of each rock measured (Sect. 9.4) was plotted directly on the HiRISE images. Finally the type of material that the rover traverses (e.g., cohesionless sand versus outcrop) was derived from a terrain classifier that determined if the surface material is sand, eolian bedforms (ripples), outcrop, or a scarp by pattern recognition (described in the next section) as well as the surface material property maps derived from the thermal

inertia described in Sect. 9.3. All four data sets were carefully co-registered (Sect. 5.6) and were used to determine the traversability of the terrain, the type of driving needed in the terrain, and the amount of time needed to traverse across the ellipse (Sect. 11.3). These data sets were also used to determine the traversability of specific types of features in the ellipse (inescapable hazards, Sect. 11.4) as well as science related traversabilty issues (such as areas with abundant, large eolian bedforms and "go to" science targets, Sect. 11.5).

A machine vision algorithm was used to segments images via pattern recognition into regions with similar textures (Ojala and Pietikainen 1999; Varma and Zisserman 2005; Cheng et al. 2003). The algorithm applies a set of binary feature detector filters or kernels to the image, with each kernel representing a specific image feature. Combining the response of the different kernels identifies the different types of terrain. Proximity, size and orientation filters further improve the texture classification, especially for regions containing eolian bedforms. An example of the partitioning is shown in Fig. 14, which shows a HiRISE image of a portion of Eberswalde crater segmented into regions of featureless terrain, elongated eolian bedforms, scarps, and "unclassified." Regions classified as "featureless" are assumed to be sandy based on their smooth appearance. Regions of elongated eolian bedforms are assumed to represent areas that can easily be traversed in the troughs between the bedforms, but are difficult or impossible to traverse across them (depending upon their size). Finally, regions that have sharp brightness discontinuities represent areas where a vertical discontinuity is possible, for example scarps or troughs. Maps of surface materials using this algorithm were made for each of the landing sites to go along with the slope and rock maps to construct the traversability maps discussed next.

11.3 Traversability Maps

Traversability maps were created by assessing slopes, rocks and surface materials within 10 m by 10 m tiles and then determining the drive mode necessary to traverse each tile. Each tile is first evaluated to determine if it is traversable by comparing the vehicle capabilities to the slopes, obstacles, and hazards inside the tile at one-meter resolution. If the tile is covered by non-traversable hazards and obstacles and their layout does not leave enough room for the rover to maneuver inside each tile, it is marked as non-traversable. All other tiles are marked according to the flight software mode needed to traverse that particular terrain. If the tile contains slopes below a minimum threshold (10°) and if there are no rocks, scarps or eolian bedforms, the tile can be traversed in blind mode. If the tile contains higher slopes, the tile is marked as requiring Visodom. If the tile contains rocks, scarps or eolian bedforms, the tile is marked as requiring AutoNav. For tiles that contain significant slopes and obstacles, the tile is marked as requiring Visodom and AutoNav. Traversability maps assemble the computed driving modes listed in order of fastest (blind driving) to slowest (AutoNav plus Visodom). Tiles that do not have any available data are marked as "unknown" and assumed to be even slower, which minimizes their selection as a drive path in subsequent estimates of traverse time.

The Eberswalde traversability map shows that the most of the area requires driving using Visodom (Fig. 15a) due to the abundance of rocks and slopes. It also has the greatest area covered by non-traversable cells. High rock abundance and slopes require Visodom driving through much of the center HiRISE image, which slows access to the delta to the west, with most favored routes to the south where blind and AutoNav driving is possible. The Gale traversability map shows most of the ellipse can be traversed in bind mode (Fig. 15b). Rougher areas to the east require driving using Visodom. The "go to" area to the south has non-traversable areas and areas requiring Visodom. To drive up the lower part of the

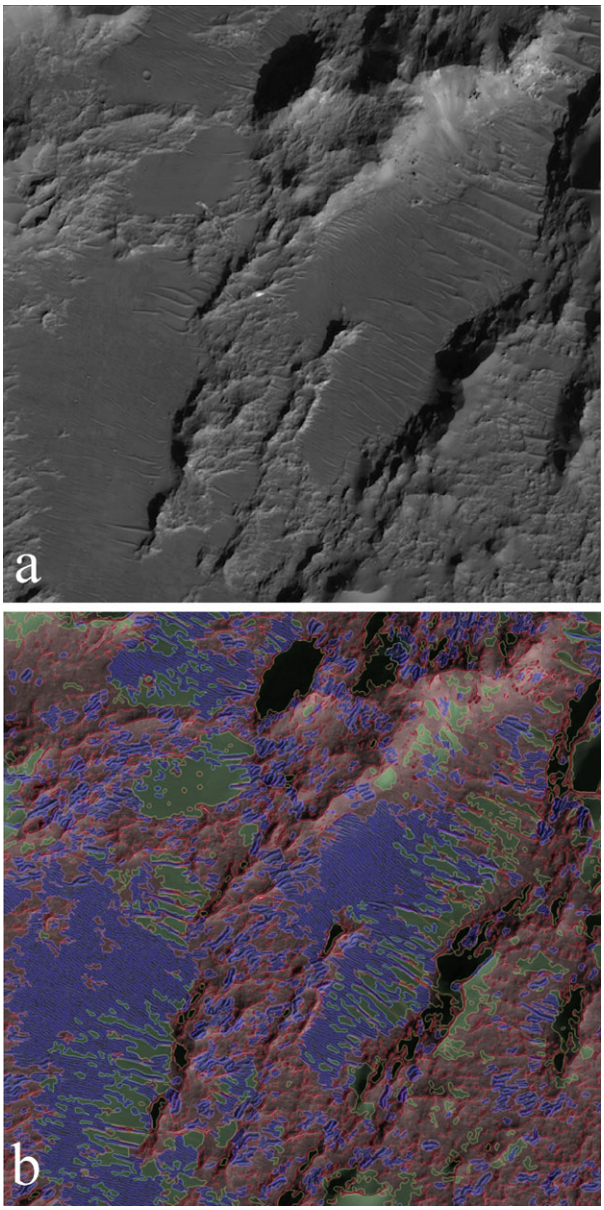

Fig. 14 HiRISE image (**a**) of a portion of the Eberswalde landing site showing terrain classification (**b**) of steep ridges, smooth plains and eolian bedforms (see text) with *blue areas* as ripples, *green areas* as featureless terrain, the *red lines* as scarps, the rest is bedrock, except for the *black areas* which are shadows. Images are 600 m on a side

mound requires driving in lower slope canyons with steep canyon walls and is described in Sect. 11.6.4. The Holden crater ellipse can be traversed mostly in blind mode (Fig. 15c), although some ridges require driving in Visodom mode. The "go to" troughs to the southeast have many untraversable scarps and many areas require AutoNav driving mode. The Mawrth Vallis ellipse can be traversed mostly in blind or Visodom modes (Fig. 15d).

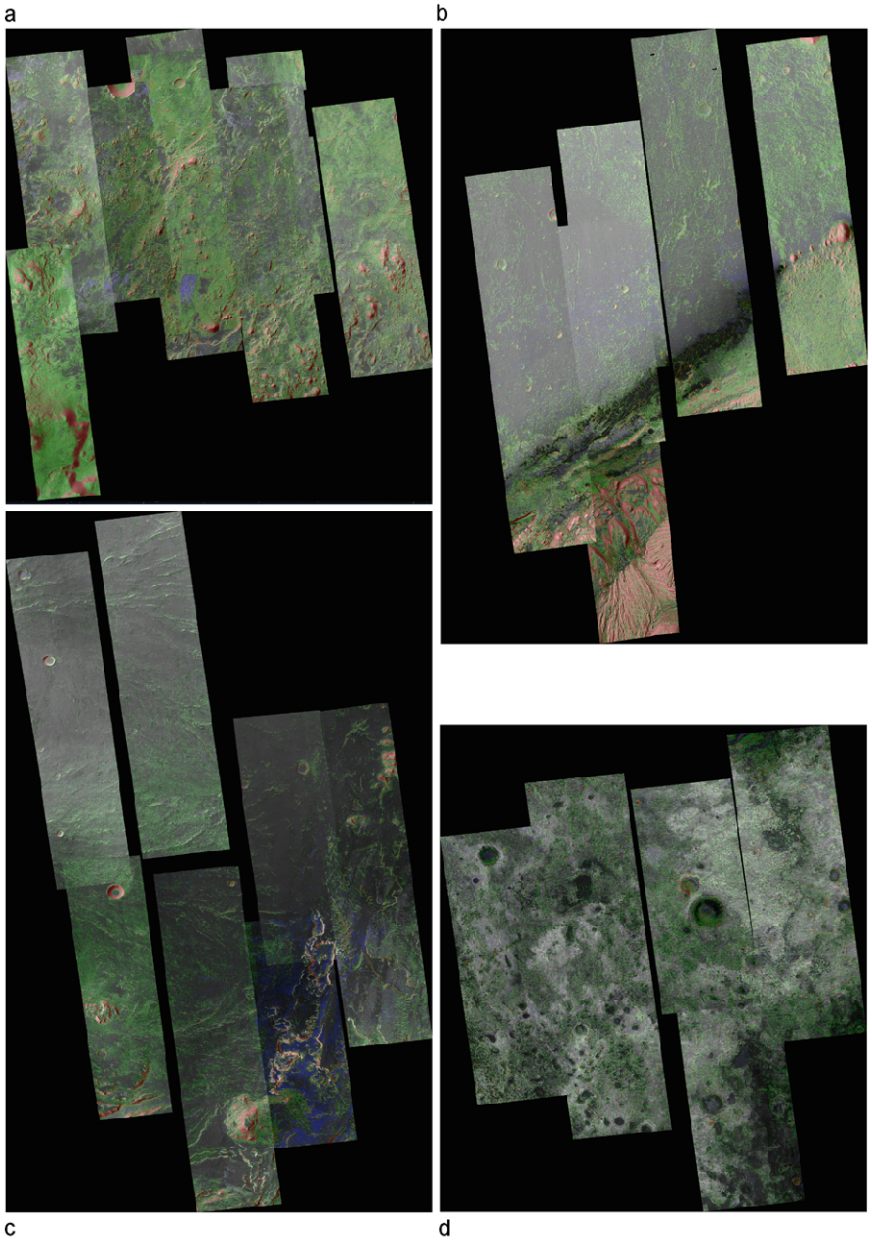

Fig. 15 Traversability maps for (**a**) Eberswalde crater, (**b**) Gale crater, (**c**) Holden crater and (**d**) Mawrth Vallis landing sites. *Gray areas* correspond to blind drive mode, *blue areas* to AutoNav drive mode, *green areas* to Visodom drive mode, *yellow* to AutoNav+Visodom, and *red areas* are not traversable. Abundant rocks and steep scarps requires Visodom driving across much of the Eberswalde (**a**). Most of the Gale (**b**) can be traversed with blind drives. Note areas in red in the Gale mound to the south are not traversable, and driving is funneled into discrete drive paths in steep sided canyons. Most of Holden (**c**) and Mawrth (**d**) can be driven in blind or Visodom modes. Maps are: (**a**) 31.3 km by 34.7 km, (**b**) 27.3 km by 39.4 km, (**c**) 29.4 km by 48.4 km, and (**d**) 29.4 km by 48.4 km with north up

11.4 Traversability Assessment

To determine the optimal paths between waypoints that takes the least amount of time, a path-planning algorithm is used. The Carnegie Mellon Field D* algorithm, which has been used on MER (Carsten et al. 2007) and is included in MSL flight software, traces a path between waypoints that minimizes the total traverse time. These paths thus favor blind driving over other modes and computes the total time needed to traverse from one location to another. Sometimes blind driving over longer distances are quicker than slower drive modes over shorter distances.

The other factor that determines the distance that can be traversed in any given Sol is the power available. The amount of energy available each sol varies over the Martian seasons due to the changes in thermal environment. The rover requires both survival heating for certain elements (e.g., instruments at the top of rover remote sensing mast) as well as warm-up heaters for rover mechanisms (e.g., wheel actuators) to raise and maintain them above their −55 °C minimum allowable flight temperature during use (Bhandari et al. 2005; Novak et al. 2010). The resultant energy for driving can therefore vary by more than a factor of two between Martian winter and summer depending on the landing site. The energy available scales directly to the amount of driving time possible and thus when driving occurs during the mission is an important factor to consider in the traverse analysis.

At the time of landing ($L_s \sim 150$), the difference between the thermal environments at the four candidate landing sites is relatively small. Therefore the available drive energy and drive time each sol is similar and it is landing site terrain (and resultant drive mode) that governs drive rate and distance very early in the mission. During the first 6 months of the mission, however, northern landing sites are moving into winter while southern landing sites are moving into summer and the thermal affects on drive distance at the different sites become more pronounced. These seasonal differences have a major impact in the drive distance possible during the first half of the mission, with southern latitude sites enjoying greater drive distances.

The first drive duration analysis assumes that the vehicle lands at the center of the landing ellipse and drives to an end location on the edge of the ellipse for 360 end locations placed one degree apart. The average path length, the number of sols required to traverse to the edge, and the average distance driven per sol are shown in Table 19 for traversing every sol, half of the sols, or 30 % of the sols (other sols book kept for science activities) beginning immediately after landing (L_s 150) or after spacecraft checkout on L_s 166. If the rover were to drive every day beginning on L_s 166, traversing to the edge of the ellipse would take 94–168 sols at the different sites, with the shortest times for the southernmost landing sites, which are in warm summer conditions and the longest time for the northernmost site, Mawrth, which is in colder winter conditions. These seasonal differences are reflected in the average distance driven each sol, with the longest (147 m) at Eberswalde and the shortest (71 m) at Mawrth. The actual percent of sols on which driving would occur is a function of the spatial distribution of science targets encountered on the surface, the efficiency of the ground operations team, and the engineering health of the rover, but these numbers are provided to distinguish between the sites assuming all other factors are equal. If the rover were to drive 50 % of available sols with the same seasonal effects between the sites beginning on L_s 166, traversing to the edge of the ellipse would take 182–271 sols at the different sites with the average distance per sol dropping to 44–76 m. Finally, if the rover were to drive 30 % of available sols beginning on L_s 166, traversing to the edge of the ellipse would take 297–381 sols at the different sites with the average distance per sol decreasing to 31–44 m. These results indicate that the rover can traverse out of the landing ellipse from the center

Table 19 Average path length, rate of travel and duration for traversing from the center of MSL landing sites to the edge of the ellipse for 360 locations space 1° apart beginning immediately after landing or 16 sols later

Landing Site	average path length, m	m/sol ($L_s = 150$)	m/sol ($L_s = 166$)	average sols @ $L_s = 150$	average sols @ $L_s = 166$
Drive 100 % of available Sols					
Eberswalde	13968	139	147	100	95
Gale	11558	106	108	109	107
Holden	12387	125	132	99	94
Mawrth 2	11879	68	71	176	168
Drive 50 % of available Sols					
Eberswalde	13968	73	76	190	185
Gale	11558	54	54	215	214
Holden	12387	66	68	188	182
Mawrth 2	11879	42	44	283	271
Drive 30 % of available Sols					
Eberswalde	13968	44	44	317	316
Gale	11558	35	35	326	326
Holden	12387	41	42	300	297
Mawrth 2	11879	30	31	395	381

Numbers shown for driving 100 % of sols, driving for half the available sols, and driving on 30 % of the available sols

Table 20 Drive analysis and durations to traverse from landing point estimates to "go to" targets starting on either L_s 150 (landing) or 166 assuming that the rover drives 100 % of available sols

Landing Site	Average path length	Meters/Sol @ L_s 150	Meters/Sol @ L_s 166	Average Sols @ L_s 150	Average Sols @ L_s 166
Eberswalde	11793	126	134	93	88
Gale	16965	161	164	105	104
Holden	12347	112	117	111	105

point at all of the sites in 14–25 %, 27–41 % or 44–57 % of the nominal mission (1 Mars year) if driven 100 %, 50 % or 30 % of available sols at the four landing sites, respectively, thus leaving about ~80–50 % of the nominal mission available to investigate areas outside of the ellipse.

To estimate the time required to drive to the "go to" sites, the set of 8001 Monte Carlo simulated landing locations for each site were input as starting points and the path that minimizes drive time to the "go to" target was computed (Table 20). For Eberswalde, a point at the southwestern edge of the ellipse was selected to provide access to the closest lobe of the delta. Drive paths selected avoided the rugged topography north of this location. For Gale, the "go to" location is south of the ellipse at the contact between the clay layer and the overlying sulfates near the entrance to the canyons (Fig. 16). Drive paths selected tend to avoid the eastern portion of the ellipse that requires Visodom driving mode. For Holden, the "go to" location is the southeastern edge of the ellipse where it intersects the troughs with

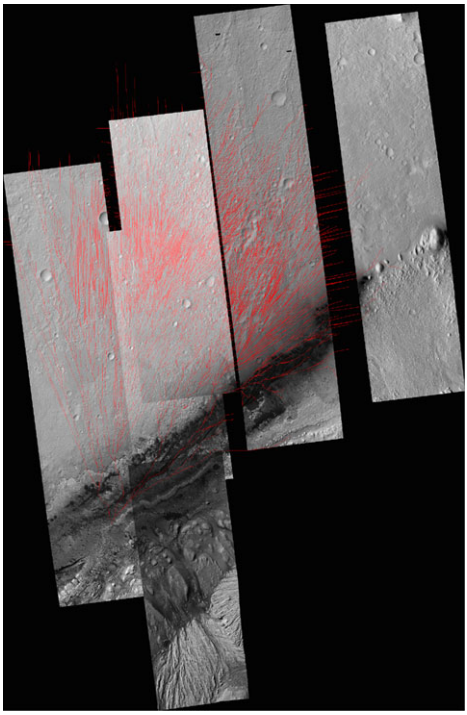

Fig. 16 Calculated minimum duration paths for 5001 Monte Carlo landing locations in the Gale crater ellipse to the "go to" location in the clay layer at the base of the mound. Average duration of paths is 104 sols if the rover is driven 100 % of the available sols (see Table 20). HiRISE images are 8 km wide

the light-toned layered deposits. Drive paths selected tend to prefer the eastern and southern portions of the ellipse where blind driving is possible.

Results show that if the rover is driven every sol starting on L_s 166, it can get to the "go to" point in an average of 88, 104 and 105 sols, driving at an average distance of 134 m, 164 m and 117 m per sol at Eberswalde, Gale and Holden, respectively, for the cloud of landing points within the ellipse. Because these durations and distances are generally similar to the previous case, the likely decrease from driving half or 30 % of the available sols will also be similar. As a result, the rover can drive to the "go to" locations from the expected landing locations in roughly 20 %, 35 % and 50 % of the nominal mission if driven 100 %, 50 % or 30 % of available sols, respectively, thus leaving about 80–50 % of the nominal mission available to investigate the "go to" areas.

11.5 Inescapable Hazards

11.5.1 Introduction

The traversability of specific types of hazards or regions were also evaluated in the ellipses. Inescapable hazards are defined as locations were the rover might land safely, but could not traverse out of. The most common type of such features are fresh craters in which the rover might land safely on the relatively flat floor, but would be unable to traverse up steep interior crater walls to escape. For a mission such as MSL in which traversing long distances within and outside of the ellipse is required, being trapped inside a crater would be a mission failure. Other areas that could be inescapable hazards are flat-topped mesas or hills with steep sides and fields of fresh sand dunes or other large eolian bedforms in which no escape paths are available.

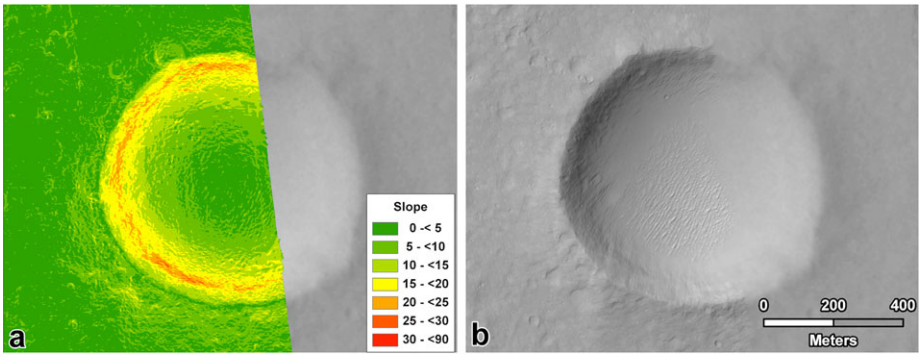

Fig. 17 One-meter slope map (**a**) and HiRISE image (**b**) of crater ID 2 in the Gale crater ellipse. Slopes on the interior wall exceed 15°, which for the soil covered surface (no outcrop obvious), would be too steep to drive out of. However, because no elevation data exist for the east side of the crater, it is classified as a probably inescapable hazard. Location of this crater can be found in Fig. 21b

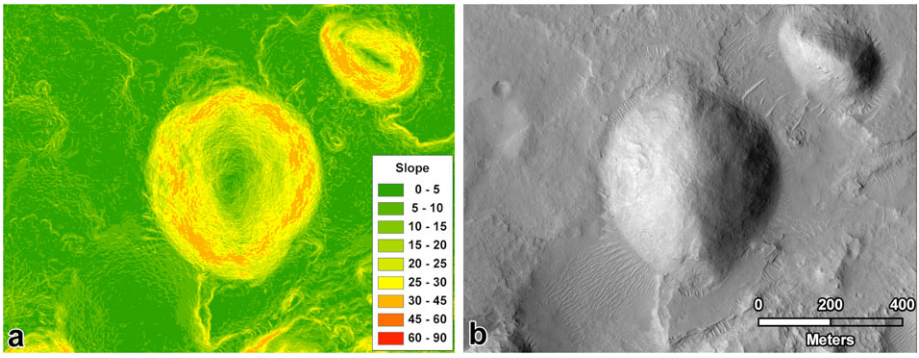

Fig. 18 One-meter slope map (**a**) and HiRISE image (**b**) of mounds in eastern part of ellipse in Gale crater (ID 87). Even though slopes on the edge of the mounds typically exceed 30°, they are less than 45° indicating that the rover would be able to drive off them if it were to land safely on top and mission success depended on it. All mounds in Gale crater are considered escapable using this criterion. Location of this mound can be found in Fig. 21b

Finding potential inescapable hazards is straightforward and involved making 1 m slope maps from the DEMs and looking for relatively flat areas surrounded by high slopes. Assigning higher slopes distinctive colors in the map, such as red, made visual identification of such areas easy. To determine if the slopes are traversable, the experience of the MER rovers and the results of MSL tests were used. Areas that exceeded 30° are considered too steep to drive up. Areas with slopes less than 15° are considered traversable and areas with slopes in between can be driven up if the surface is outcrop. The rover is stable on slopes of up to 45°, so this is the limit assumed if the rover were to land on top of a steep sided mesa and had to drive off of it to escape. HiRISE images were used to identify soil-covered surfaces versus outcrop. Surfaces covered by eolian bedforms, or soil (with or without rocks) without any organized layers or distinct outcrop were identified as soil or sandy surfaces. Areas with distinct layers, stratigraphy or part of a rock mass were identified as outcrop. Examples of potential inescapable hazards are shown in Figs. 17 to 20. All slope maps of the landing ellipses were carefully inspected for areas of high slopes surrounding low slope

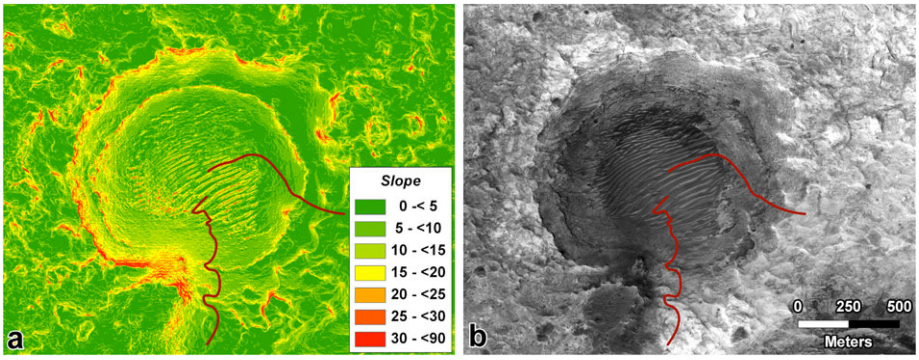

Fig. 19 One-meter slope map (**a**) and HiRISE image of fairly large escapable crater in Mawrth Vallis ellipse (ID 37). Eolian bedforms on bottom are far enough apart to drive inbetween and although slopes of the inner wall typically exceed 15°, there are many paths with slopes <20°, which should be traversable on exposed outcrop (two such paths shown in red). Location of this crater can be found in Fig. 21d

areas. If escape routes that meet the above criteria could be found they were classified as escapable (Figs. 18 and 19). If no escape routes could be found or escape routes might be too narrow for the rover to drive (<5–10 m) or complete data did not exist, they were classified as probably inescapable (Fig. 17). If no escape routes could be found, they were classified as inescapable hazards (Fig. 20).

11.5.2 Results

The Eberswalde crater ellipse has the second largest number of potentially inescapable hazards (42). Most of the hills and mesas are fairly small (<300 m diameter), and are found in rugged terrain in the western part of the ellipse along with some to the south and east (Fig. 21a). One of these mesas has continuous surrounding slopes that exceed 45° and so is inescapable (ID 24) and covers 0.0037 % of the ellipse (95 m diameter). Of the possible inescapable craters in Eberswalde, two are inescapable and cover 0.01 % of the landing ellipse.

Within the landing ellipse of Gale crater, 55 possible inescapable hazards were evaluated in the 1 m slope map and HiRISE images (Fig. 21b). Of these, 6 mesas or hills, all in the eastern edge of the ellipse, have slopes less than 45° and so are escapable (e.g., Fig. 18). Of the remaining, 31 possibly inescapable hazards, four were considered probably inescapable or inescapable, including the fairly large diameter (>700 m) crater (ID 2) shown in Fig. 17. All together these craters comprise 0.19 % of the surface area within the ellipse.

The Holden crater ellipse had the fewest potentially inescapable hazards (17), dominated by craters (Fig. 21c). Of these, four craters (including the largest crater >1 km, ID 68) are probably inescapable and occupy 0.27 % of the ellipse. One 220 m diameter crater (ID 77) is inescapable and occupies 0.0097 % of the ellipse (Fig. 20). Most of these craters have very large eolian bedforms (relative to the size of the rover) that are likely not traverable (Fig. 20). Most of these are located in the southern part of the ellipse, near the "go to" area of greatest scientific interest. Together the inescapable and probably inescapable craters occupy 0.28 % of the ellipse.

Mawrth Vallis has 46 potentially inescapable hazards, with most of these being small (<200 m diameter) craters and (<300 m diameter) mesas scattered throughout the ellipse (Fig. 21d). Of these, two craters are inescapable and cover 0.01 % of the ellipse. No mesas

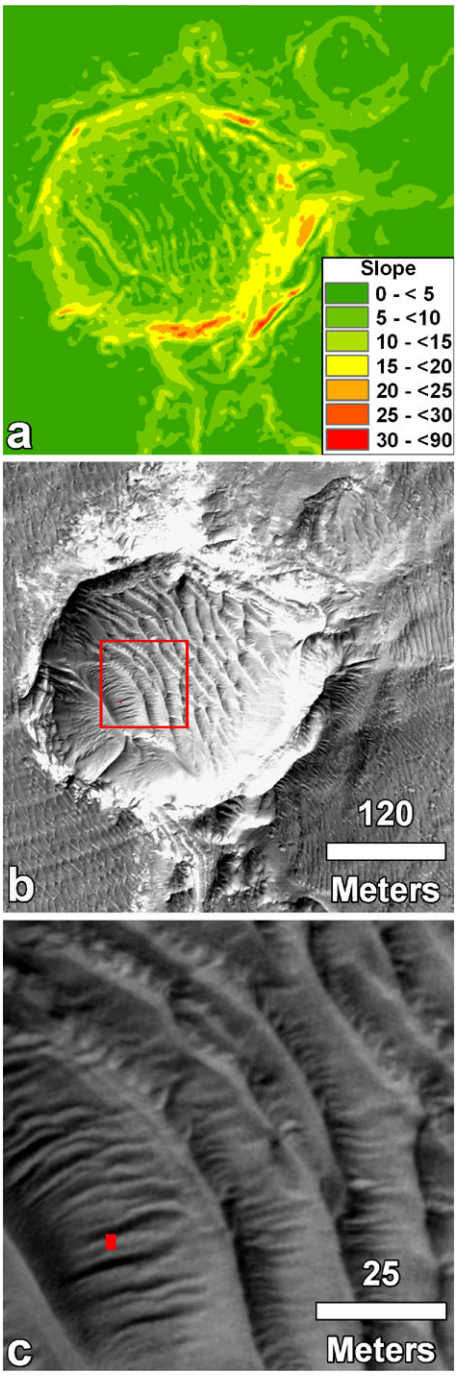

Fig. 20 One-meter slope map (**a**), corresponding HiRISE image (**b**), and enhanced view of the west-southwest portion of the crater interior with red rectangular footprint (2 by 3 m) of the MSL rover for scale (**c**) of 220 m diameter crater in Holden (ID 77). Although some crater wall slopes appear $<15°$, giant eolian bedforms (relative to the rover) that typically exceed 15° form closed depressions that would trap the rover, indicating that it is an inescapable hazard. Location of this crater can be found on Fig. 21c

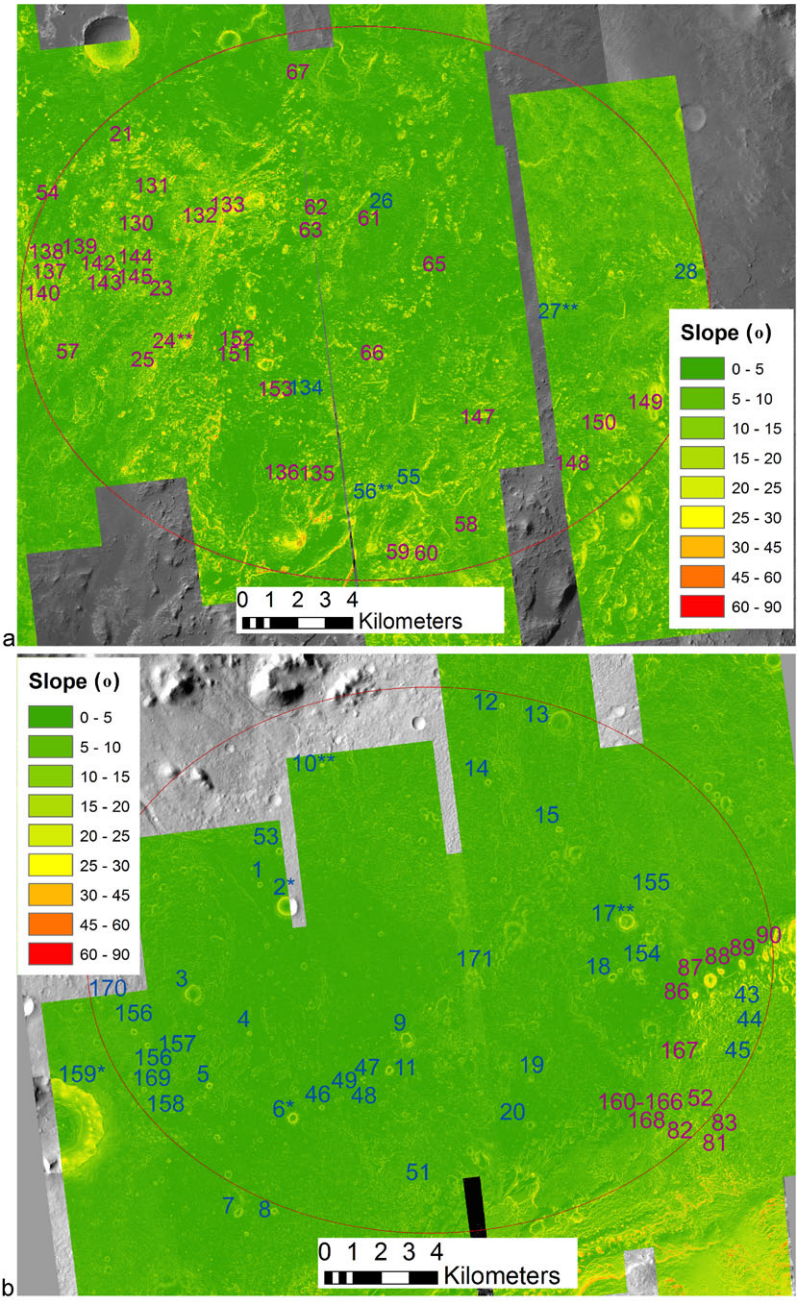

Fig. 21 One-meter slope maps for (**a**) Eberswalde, (**b**) Gale, (**c**) Holden, and (**d**) Mawrth showing potential crater inescapable hazards in blue, potential hill inescapable hazards in purple; probable inescapable hazards marked with * and inescapable hazards marked with **. Landing ellipse shown in *red*

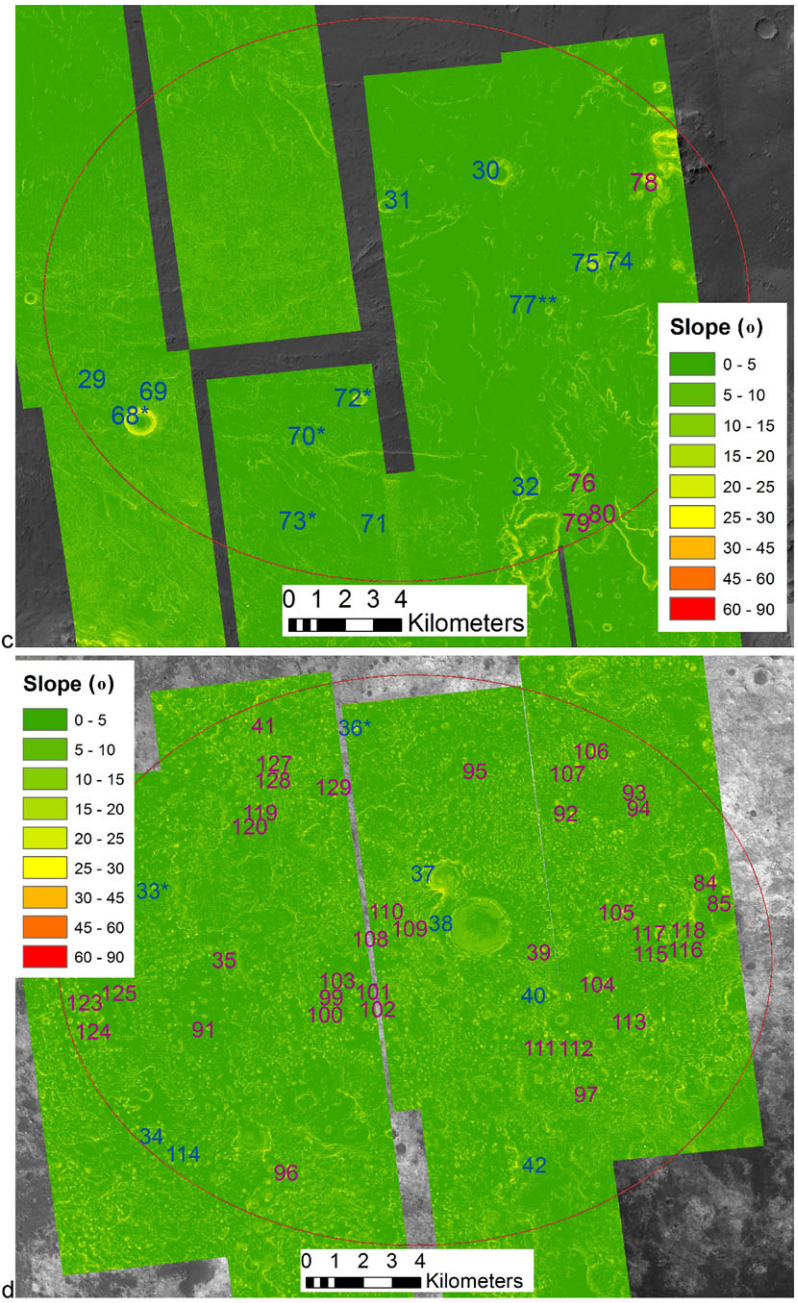

Fig. 21 (*Continued*)

are inescapable. Two large craters near the center of the ellipse are escapable (ID 37 and 38) and with the stratigraphy exposed in their walls actually represent interesting science targets (Fig. 19).

All together, inescapable hazards within the four landing ellipses cover extremely small areas of the ellipses (0.01–0.28 %) and are thus not a factor in site selection. Even so, all inescapable and probably inescapable hazards were included as failures in the landing simulations described in Sect. 10.

11.6 Science Related Traversability Issues

11.6.1 Introduction

Specific areas and traversability issues important for carrying out the expected scientific investigations at the landing sites were examined as well. This was done as a check on the results derived in Sect. 11.3, but also to make sure that traversability issues would not limit the key scientific investigations planned at the landing sites. To carry out this investigation, 1 m slope maps from the DEMs were binned according to slope in 5° increments and co-registered HiRISE images were examined to distinguish the type of material being traversed. Traversability criteria (slope and material) are the same as used in Sects. 11.2 and 11.5.1. The size of eolian bedforms was also compared to the size of the rover to assess their trafficability. Experience with the Opportunity rover has clearly shown that eolian ripples at a scale comparable to the wheel diameter (50 cm) become difficult or impossible to cross with substantial wheel slip. In terrain with such large ripples at Meridiani Planum, paths were planned along the ripple troughs to avoid ripple faces with higher slope (Parker et al. 2010). Finally, ripples that are much larger than the rover as well as large sand dunes with steep slip faces were not traversable because they had slopes that approached or exceeded 15° and are composed of loose or poorly consolidated sand or sediment. This process using HiRISE images was used to plan the 20 km long path from Victoria crater to Endevour crater to avoid large eolian bedforms (Parker et al. 2010) that Opportunity has successfully traversed over 3 years without mobility issues across terrain that matched that expected in the images.

11.6.2 Mawrth Vallis and Eberswalde Crater

There do not appear to be any major traversability issues with the Mawrth Vallis landing ellipse. Although small regions of high slope exist throughout the ellipse (Fig. 21d), they do not block assess to the different phyllosilicate materials observed and there are multiple places to assess the different units mapped in the CRISM and HiRISE images.

Eberswalde crater has lots of rocky mesas and hills that are too steep sided to traverse (e.g., Fig. 21a). The western portion of the ellipse has many of these rocky mesas and hills making access to the delta to the west of the ellipse somewhat slow going. A number of paths also appear to provide access to the delta (Fig. 22). At least one path also provides access to well defined stratigraphic layers at the exposed edge of the delta (Fig. 23).

11.6.3 Holden Crater

Although the Holden crater ellipse had few potential inescapable hazards, most of the landing ellipse is covered by moderate to large eolian bedforms that resemble the ubiquitous ripples that cover the Meridiani Planum where Opportunity has traversed. An example of

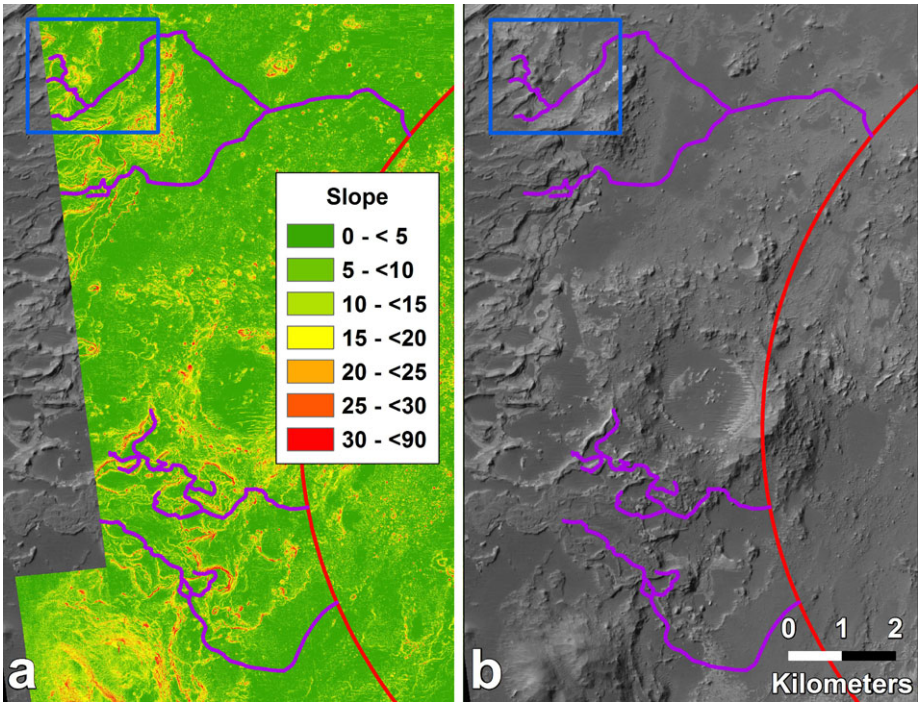

Fig. 22 One-meter slope map (**a**) and HiRISE image (**b**) showing access to the Eberswalde delta. Traversable paths shown in *purple*, western edge of landing ellipse shown in *red*, and *blue box* shows location of Fig. 23

the ripples is shown in Fig. 24 with a red rectangle that approximates the MSL rover footprint. As can be seen, most of the surface is covered with closely spaced north-trending ripples that are similar in scale to the rover. As a result, like the Opportunity rover, drives would be planned down the troughs between the ripples to reduce wheel slip (Parker et al. 2010). The terrain appears traversable, but crossing the grain of the ripples would be done at break points between the ripples and would thus reduce the flexibility in selecting the drive direction. Because the area of greatest scientific interest is located in the southeastern part of the ellipse, even if the rover were to preferentially land in the center of the ellipse a large component of southerly driving would be expected.

The area of greatest scientific interest for Holden crater are outcroppings of light toned, phyllosilicate bearing layered deposits exposed in a series of troughs that extend south from the southeastern edge of the ellipse. Six key science locations where layered materials are well exposed along the trough walls have been identified by Irwin (2010) (Fig. 25). An example of the first target near the southern constriction of the northernmost trough, shows that the canyon floor is covered by huge eolian bedforms that dwarf the rover (Fig. 26). This is representative of most of the trough floors with very large eolian bedforms that are of order 10 m wide, meters high, and routinely exceed the 15° slope limit for the rover. The bedforms are so closely spaced that traversing inside the troughs would either be impossible or would be so slow as to be impractical. Fortunately the plains surfaces outside of the troughs are easily traversable with comparatively small bedforms. In addition the outcroppings of key stratigraphy at the important science areas identified by Irwin (2010) are all at slopes that are less than 15°, which should be easily traversable on outcrop. As a result, although

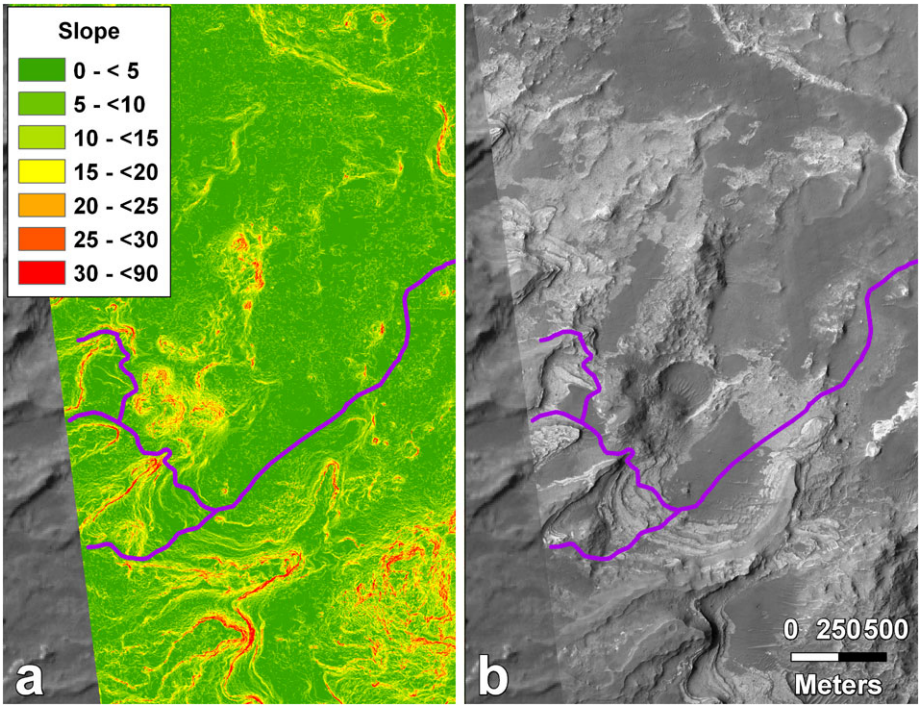

Fig. 23 One-meter slope map (*left*) and corresponding HiRISE image showing traversable paths that provide access to well defined stratigraphic layers at the exposed edge of the Eberswalde delta. Traversable paths shown in *purple*; location of figure shown in Fig. 22

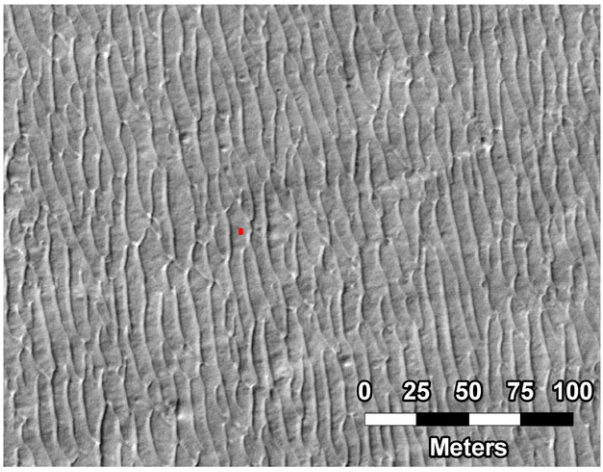

Fig. 24 Typical Holden crater surface with ripples and red 2 m by 3 m rectangle showing the footprint of the MSL rover (*middle of image*). Given that the ripples are at a similar scale to the rover, experience driving the Opportunity rover in comparable terrain, indicates that drives will be preferentially planned down the troughs between the ripples (Parker et al. 2010). Crossing ripples to go either east or west would be done at breaks between the ripples, which would reduce flexibility in the drive direction

driving inside of the troughs will not be possible (or practical), all of the key stratigraphic sections can be accessed by driving on the plains and dipping into and out of trough walls (Fig. 25).

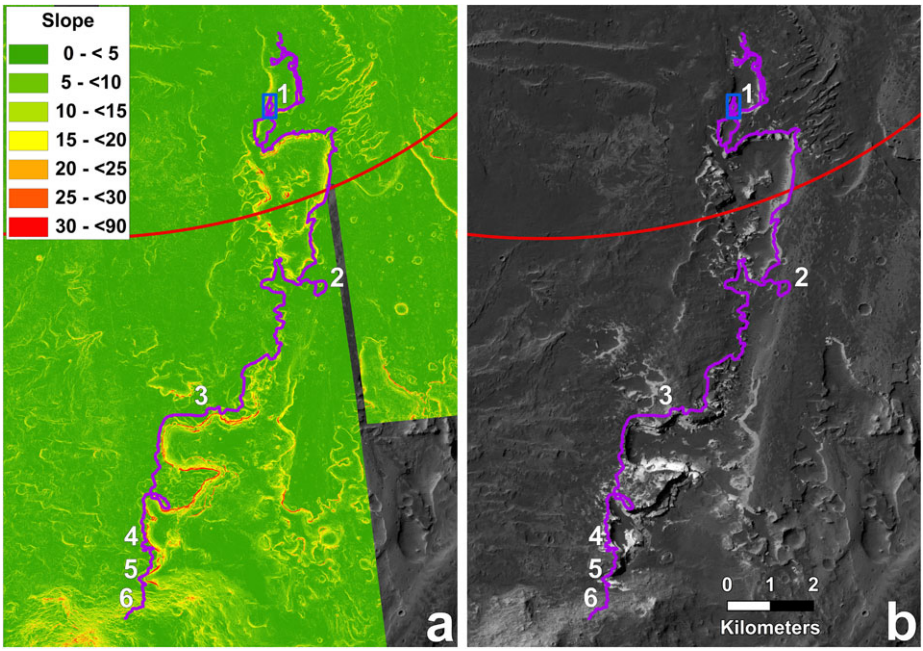

Fig. 25 One-meter slope map (**a**) and corresponding HiRISE image (**b**) showing traversable paths (*in purple*) that provide access to all high science priority light toned layered deposits exposed in troughs identified by Irwin (2010) in Holden crater (numbered). Southeastern edge of landing ellipse shown *in red*; location of Fig. 26 shown in rectangle near 1

11.6.4 Gale Crater

The Gale crater landing site requires driving out of the ellipse to the south to sample sufate and phyllosilicate bearing strata in the lower part of the central mound. As a result, the ellipse must be traversable to the south and the lower part of the mound must be accessible by the rover. Although there are no mobility concerns for most of the landing ellipse, a series of dark, fresh sand dunes that could be active (Hobbs et al. 2010) extend from the southern edge of the ellipse to the northeast. Examination of these dunes in HiRISE images and slope maps shows many of the dunes exceed the slope limit for driving on cohesionless material, but that there are a number of traversable troughs mostly swept clean of dark sand (Fig. 28) that cross the dune fields from north to south (Fig. 27). As a result, traversing to the south to exit the landing ellipse appears feasible.

South of the Gale ellipse a stratigraphic section has been identified in CRISM spectra that includes a lowermost sulfate rich layer with an overlying clay-bearing layer that is overlain by more sulfates, with mixed clay and sulfate layers in between (Milliken et al. 2010). The rover must be able to sample all of these layers to address the most important science topics at this site. Examining the slope maps of the lower mound and correlating with the mineral layers identified in CRISM shows that the lowermost sulfate layer is easily accessible south of the dune field. The boundary between the lowermost sulfates and the overlying clay unit occurs at the first steep slope, that has been called the “first fence” (Fig. 29). Between 10 and 20 paths have been identified through the “first fence,” so access to the clay layer is also possible. The mixed sulfate and clay layer above the clay layer begins above a second

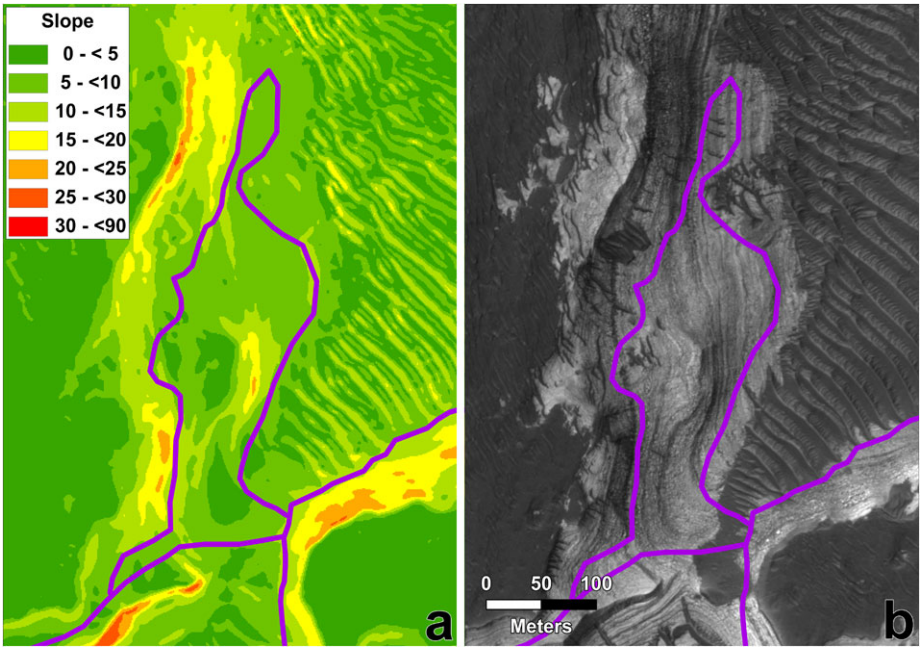

Fig. 26 One-meter slope map (**a**) and corresponding HiRISE image (**b**) showing traversable paths at southern trough constriction at the northernmost key science target identified by Irwin (2010) in the northern trough of the Holden crater landing ellipse. Ripples like this that dwarf the rover are ubiquitous in the trough floors and have slopes that typically exceed 15° making driving in the trough floors impossible. Driving on the plains adjacent to the troughs should be easy and the rover can dip into low slope exposures of the key layered strata as shown in this example. Location of this figure shown in Fig. 25

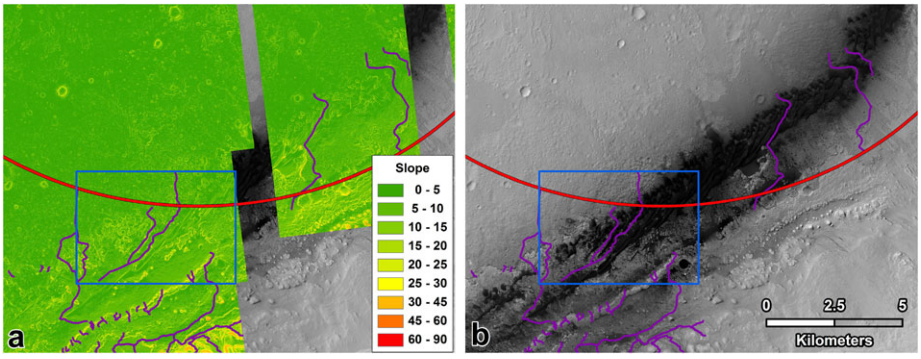

Fig. 27 One meter slope map (**a**) and corresponding HiRISE image (**b**) showing traversable paths (*in purple*) through dark dunes at southern edge of Gale crater ellipse (*in red*). Blue rectangle shows detail in Fig. 28

zone of steep slopes called the "second fence," which also has multiple traversable paths (5–10) through it, so the rover should be able to sample this unit as well. After this unit, the topography of the mound steepens substantially and all travel is funneled into a number of relatively low slope pathways that weave among mounds and in steep sided canyons. There are over 10 possible pathways that cross the first steep line of mesas and mounds. Driving up

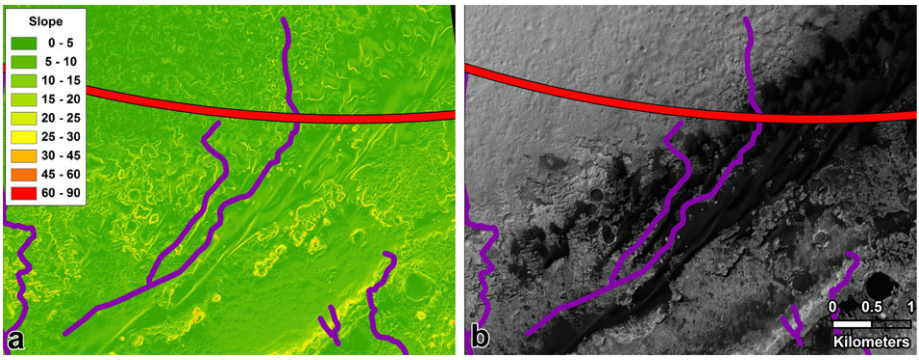

Fig. 28 One-meter slope map (**a**) and corresponding HiRISE image (**b**) showing detail of traversable paths (*in purple*) through dark dunes at southern edge of Gale crater ellipse (*in red*). Paths are low slope and partially swept clean of sand. Location of image shown in Fig. 27

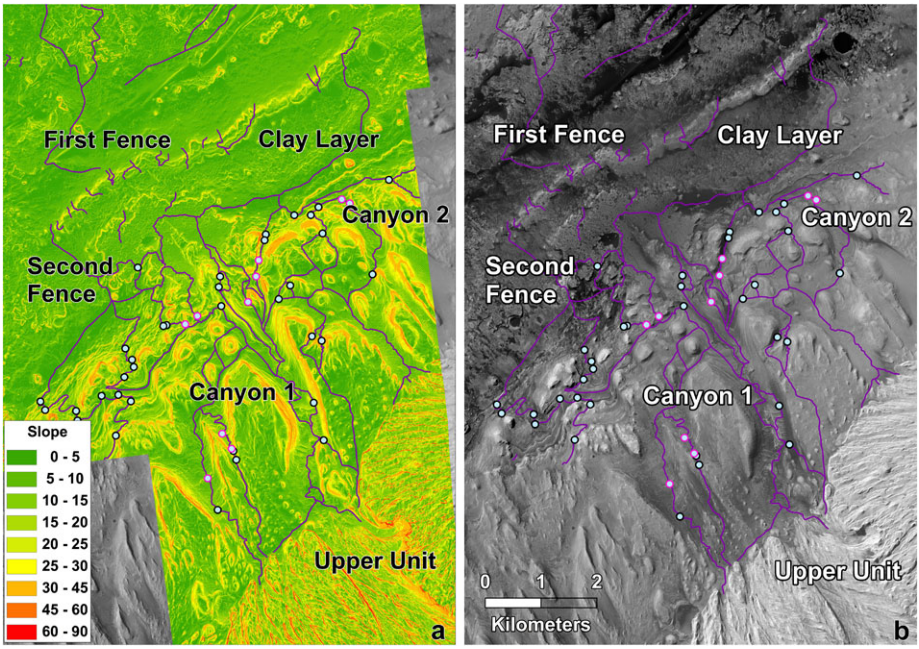

Fig. 29 One-meter slope map (**a**) and corresponding HiRISE image (**b**) showing traversable paths (*in purple*) through high science priority clay and sulfate deposits south of the Gale crater ellipse. Choke points where the traverse path must go through a narrow canyon are shown as dots. *Blue dots* are the locations where the slope along the traverse approaches the rover limit for the observed material. *Pink dots* are where the traverse path is between 5–10 m wide; all others are $\geq$10 m wide

any one of them would provide access to the overlying sulfate rich strata. Beyond the first line of steep mesas and mounds about 6 possible pathways could allow driving up to the uppermost light-toned unit that is unconformably overlain on the sulfate unit underneath. Ubiquitous steep slopes in this uppermost unit indicates it is not traversable. A number of narrow potential choke points, that are 5–10 m wide or require bedrock to traverse slopes

$>15°$ have been identified along many of these pathways (Fig. 29). Given uncertainties in the stereo derived elevations and difficulties in uniquely identifying soil patches from layered rock along many of the paths, it may be difficult to be sure about the traversability of some of them. Nevertheless, the fact that multiple paths allow access to all of the key mineral layers identified from orbit, indicates that the main science goals of sampling these layers can be accomplished at this site.

12 Final Deliberations, Reviews and Selection

The final steps leading to selection of the Gale landing site included an all-hands MSL Science Team meeting, meetings of the Project Science Group and the MSL project, an independent certification review, a planetary protection review, and two meetings at NASA Headquarters between the Project and the NASA selection official, the Associate Administrator for the Science Mission Directorate. The MSL Science Team met after the fifth community workshop, spending the morning in final discussion of preferred landing sites. The team considered their scientific merits and worked through scenarios of how scientific exploration might unfold at the different sites. A strong consensus emerged to advance the Eberswalde and Gale landing sites. The deltaic environment at Eberswalde provided a quiet depositional environment with clay that might have preserved organic carbon. Gale had the greatest diversity of geologic environments that could be explored for evidence related to habitability, including preserved organic carbon. It was further noted that the Gale mound would offer a visually spectacular mission for the general public. The Project Science Group met in the afternoon and discussed the merits of Eberswalde versus Gale, and the application of their instruments in addressing the principal goals of the mission, with a consensus for Gale. Having already determined that no engineering or operational factors clearly discriminated between the final sites, the MSL Project decided to recommend Gale and Eberswalde to the Associate Administrator, with a preference for Gale.

On June 9 and 10 the Project presented to the NASA-chartered, Independent Landing Site Certification Board the process leading up to the recommendations. The Board, consisting of three scientists and three engineers, found the process to be fair and comprehensive and concurred with the project recommendation. The NASA Planetary Protection Office held a review on June 23, 2011 and determined that there was no evidence that any of the four sites violate the provisions related to extant water and water ice as required for the mission (see Sect. 3). In November 2011, NASA re-categorized MSL as a IVa mission, with no implication for the landing site, but with additional restrictions on using the rover's non-sterile wheels and sampling tools in regions with a higher likelihood that terrestrial organisms may propagate or a higher potential for extant Martian life forms (neither expected at Gale crater), without first consulting the NASA Planetary Protection Office.

A meeting was held at NASA Headquarters on June 24 where the Project presented to the Associate Administrator, who was accompanied by a Board including the Division Directors (Directorate Program Management Council), the NASA Planetary Protection Officer, and Mars Exploration Program Office. Engineering and science data were shown by the project for all four final landing sites, in addition to summaries representing the views of the Science Team and Project Science Group. After discussion, the Associate Administrator and Board downselected to Eberswalde and Gale for further consideration. These NASA Headquarters officials deliberated for a period of one month and reconvened on July 22. At that time, the NASA Mars Program Scientist presented to the Associate Administrator and Board the "pros" and "cons" of Eberswalde versus Gale. At the end of the presentation, the Board

recommended Gale as the final choice, which was accepted by the Associate Administrator. MSL will land on August 5, 2012 in Gale crater at an ellipse 19.7 km by 6.9 km centered at 4.5965°S, 137.4019°E (Fig. 12b).

13 Summary/Conclusions

The Mars Science Laboratory landing site selection process took over five years, involved broad participation of the science community via five open workshops, and narrowed an initial >50 sites to four finalists (Eberswalde, Gale, Holden and Mawrth) based on science and safety. For the first time, the landing ellipse is small enough (25 by 20 km) and the drive distance and mission lifetime long enough, that "go to" landing sites could be considered. "Go to" landing sites are those in which the ellipse is placed on smooth, flat terrain adjacent to the material of greatest science interest and the rover then drives out of the ellipse to access that material. Most of the high-priority landing sites and three of the final four are mostly "go to" sites, although materials of interest are found in the ellipses as well.

Landing site selection for MSL began before MRO was in its mapping orbit with about 35 widely distributed sites proposed at the first workshop in June 2006. MRO targeted imaging resulted in about 50 sites being considered at the second workshop in October 2007, with six sites selected for further study. A call for new sites based on new MRO data resulted in four new sites being proposed and the steering committee adding a seventh site (Gale). Discussion at the third workshop in September 2008 led to the downselection to four sites (Eberswalde, Gale, Holden and Mawrth). The delay in launch to 2011, allowed a call for new sites based on MRO data in 2009 that had to be as compelling as the final four; seven sites were proposed, two were imaged by MRO and studied, but none were added. Detailed science evaluations, evaluation of surface properties and engineering and traversability studies were presented at the fourth and fifth workshops in 2010 and 2011. After a series of project meetings (addressing both science and engineering issues and potential risks), external reviews, and presentations to NASA Headquarters, the Associate Administrator for space science selected the Gale crater landing site for MSL in July 2011.

Engineering constraints important for locating and selecting landing sites derive from the spacecraft design and the EDL scenario. Aero-maneuvering to remove the effects of atmospheric density variations results in the small landing ellipse (25 by 20 km), compared with simple ballistic descent on previous Mars missions. Because the rover, with its rocker-bogie mobility system is placed directly on the surface by the sky crane, it is the most slope-tolerant lander ever sent to Mars and can accommodate up to 30° slopes. Latitude is limited to ±30° by the thermal management of the rover and instruments. Elevation must be < -1 km with respect to the geoid for sufficient atmosphere to slow the spacecraft. Relief should be less than 100–130 m at baselines of 1–1000 m for control authority and sufficient fuel during powered descent. Rock abundance must be moderate to avoid impacting the belly pan with a rock higher than 0.6 m during touchdown. Finally, the surface must be radar-reflective, load bearing, and trafficable that is safe for landing and roving and not dominated by fine-grained dust.

MSL was categorized by the NASA Planetary Protection Office as a IVc mission because of its hot power source and the concern that it could potentially create an environment favorable to the propagation of microbes. Because the spacecraft was not fully sterilized due to the prohibitive cost, landing is limited to regions not known to have extant water or water ice within 1 m of the surface. The final landing sites were subject to formal review by the NASA Planetary Protection Office for compliance.

The science objectives of the Mars Science Laboratory mission are to quantitatively assess past habitability and the environmental conditions at the site by: (1) determining the nature and inventory of organic carbon compounds, searching for the chemical building blocks of life, and identifying features that may record the actions of biologically relevant processes, (2) characterize the geology of the landing region at all appropriate spatial scales by investigating the chemical, isotopic, and mineralogical composition of surface and near-surface materials, and interpreting the processes that have formed rocks and soils, (3) investigate planetary processes of relevance to past habitability (including the role of water) by assessing the long timescale atmospheric evolution and determining the present state, distribution, and cycling of water and CO_2, and (4) to characterize the broad spectrum of surface radiation. These objectives were translated into specific criteria related to diversity, context, habitability and fossil/biosignature preservation for evaluating and prioritizing prospective landing sites.

MSL benefited from having the most extensive and detailed data sets ever assembled to evaluate landing sites on Mars. In addition to all previous data sets as well as data acquired by spacecraft orbiting during the selection process, MRO extensively targeted HiRISE (~0.3 m/pixel), CTX (6 m/pixel) and CRISM (visible to near-infrared spectra) data that gave an unprecedentedly detailed view of surface characteristics for hazard analysis, but also high-resolution spectral information on key aqueous minerals directly relevant to the science objectives. In addition to data used for all previous landing site selections, data particularly useful for MSL site selection included: (1) 100 m THEMIS thermal images and global mosaic for siting ellipses in smooth, flat locations (Christensen et al. 2004), (2) HRSC multiple orbit stereo orthophotos (12.5 m/pixel) and DEMs (~50 m elevation postings) that are excellently georegistered to MOLA elevation maps (Gwinner et al. 2010a), thereby providing a well referenced cartographic base map with a well understood conversion to inertial space critical for navigating the spacecraft to the correct entry point, (3) global TES thermal inertia data at 3 km/pixel (Putzig et al. 2005; Putzig and Mellon 2007), (4) THEMIS thermal inertia data at 100 m/pixel (Fergason et al. 2006a, this issue), and (5) MRO image data from HiRISE, CTX and CRISM.

Each of the 4 final landing sites clearly address the primary scientific goal of assessing the past habitability of Mars and all represent acceptable science targets for MSL. At Eberswalde crater the presence of a delta makes specific predictions for clay bearing strata deposited in low energy bottomset beds that might have been particularly favorable to the preservation of organic materials and/or other kinds of biosignatures. In addition, the crater stratigraphy, geomorphology, and mineralogy record the formation and evolution of this fluvial-deltaic crater lake. In Gale crater, a thick sequence of finely bedded deposits is exposed in its central mound with both phyllosilicate and sulfate bearing strata, thereby representing a diverse sequence of aqueous habitable environments over an extended time. At Holden crater, laterally extensive, sub-meter phyllosilicate-bearing strata are well exposed in a closed fluvial-lacustrine system with a well understood relationship to the global stratigraphy and regional climatic events. Mawrth Vallis has thick deposits of the most phyllosilicate rich rocks on Mars that record the Late Noachian environment on Mars, when the climate may have been warmer and wetter. Strata containing Mg–Fe smectites and Al-rich phyllosilicates, sulfates, and possibly jarosite record varying aqueous environmental conditions.

Remote sensing data of the final four MSL landing sites can be compared to similar data at the existing six landing sites to interpret their surface characteristics, because ground truth at these sites relate favorably to their signatures in remotely sensed data. Eberswalde, Holden and Mawrth have low albedos and dust cover index indicating these sites should be relatively dust free (similar the Opportunity landing site). The Gale landing ellipse should be

about as dusty as the VL1 site, although the lower mound should be relatively dust free. The bulk thermal inertia of all 4 sites are all comparable or higher than previous landing sites indicating load-bearing surfaces composed of moderately to highly cohesive duricrust or cemented sediments. THEMIS thermal inertia maps correlate with units observed in HiRISE images, with low inertia areas dominated by eolian bedforms composed of cohesionless or poorly cohesive sand sized particles, intermediate thermal inertia areas composed of cohesive duricrust or cemented sediments, and high thermal inertia areas composed of bedrock or strongly indurated sedimentary rock.

Individual rock diameter and height of rocks >1.5 m diameter and rock size-frequency distributions were measured over 80–95 % of the MSL landing sites from shadows cast in HiRISE images. Rocks were counted in 150 m tiles and fit to model size-frequency distributions over 450 m areas. Average rock abundance within the ellipses is greatest at Eberswalde (5.4 %, but varies from 0–27 %), followed by Gale (3.9 %), Mawrth (3.3 %) and Holden (0.3 %) making these sites qualitatively similar to different parts of the Gusev cratered plains. All sites meet the engineering constraint for safe landing from rocks impacting the rover belly pan.

Relief at baseline lengths of 1–1000 m important to ensure proper control authority and fuel consumption during powered descent (100–130 m) was investigated using binned MOLA data at 926 m length scale, along track MOLA data at 300–1200 m length scale (also extrapolated to 100 m), MOLA pulse spread (roughness at 75 m length scale), and in mosaiced HiRISE/HRSC DEMs. All sites have a very low probability of exceeding this constraint. Comparison of slope statistics at 1.2 km and 100 m length scales to the previous landing sites shows all of the MSL sites to be substantially rougher by a factor of 2–5 at 1.2 km length scale (with Eberswalde and Gale the roughest and Holden the smoothest) and comparable (Holden) or rougher at 100 m length scale. Slope statistics at 5 m length scale indicate that Holden and Gale are comparably rough to MPF and VL1 (the roughest of the previous landing sites), whereas Mawrth and Eberswalde are rougher. Even so, the area covered by slopes that exceed 30° (beyond which touchdown failure sharply increases) is substantially less than 1 % at all of the sites. Although no X-band delay-Doppler radar data directly sample any of the 4 landing sites, returns from an observing angle of $>5°$ at Holden, Eberswalde and Gale, and depolarized S-band observations at Mawrth show no unusual or anomalous reflectivities or roughness that might adversely impact the descent radar.

Sophisticated landing success simulations carefully monitored vehicle interactions with the local atmosphere during entry and parachute descent, radar-terrain interactions during parachute descent, and powered flight, and rover mechanical interactions with the terrain during touchdown via 8001 Monte Carlo EDL simulations. For each simulation, over 5000 individual variables are stored to represent the state of the vehicle at key times during the EDL sequence of events and are processed to determine system margins and identify any out-of-specification cases that violate predetermined EDL flight rules. Touchdown hazard maps of each site were derived from co-registered slope statistics and rock abundance in 150 m cells derived from the DEMs and rock maps. The percentage of out of specification cases for entry and descent are less than 0.3 % at all of the sites. The percentage of out of specification cases for touchdown range from 0.64 % at Eberswalde to 0.14 % at Mawrth. Combined EDL success rates range from 99.14 % at Eberswalde to 99.72 % at Marwth. Because the uncertainty in these simulations is estimated to be ± 0.5 %, differences in the success rates are comparable with the incertainty, and so EDL safety was not a significant discrimator in final site selection.

Due to the projected long life of the rover and the potential for driving long distances, the traversability of the landing sites was evaluated to assess the difficulty in driving and

duration between landing locations and science targets and in particular for the "go to" targets at Eberswalde, Gale and Holden. Traversability maps were derived from slope, rock and material property maps, the latter derived from pattern recognition software of HiRISE images that discriminates eolian bedforms, scarps, featureless (sandy) and bedrock and from supervised classification of THEMIS thermal inertia maps. The traversability maps describe the three drive modes in order of decreasing traverse rate (due to computational requirements), blind, autonomous navigation, and visual odometry, needed in 10 m cells based on the rocks, slope and surface material present in each. A path planning algorithm is used to trace paths between waypoints that minimizes the total traverse time. Finally, the thermal environment controlled by the seasons on Mars in which the northern site (Mawrth) is moving into winter and the southern sites (Eberswalde and Holden) are moving into summer strongly controls drive distance (by up to a factor of 2) during the first half of the mission due to the need to heat and thermally manage the mobility system, which reduces the total energy available for driving. Integration of these factors indicate that the rover can traverse to the edge of the landing ellipse from the center point at all of the sites beginning on L_s 166 in 14–25 %, 27–41 % or 44–57 % of the nominal mission (1 Mars year) if driven 100 %, 50 % or 30 % of available sols, respectively, at the four landing sites. The rover can drive to the "go to" locations at Eberswalde, Gale and Holden from the expected landing locations in roughly 20 %, 35 % and 50 % of the nominal mission if driven 100 %, 50 % or 30 % of available sols, respectively, thus leaving about 80–50 % of the nominal mission available to investigate these "go to" areas.

Potential inescapable hazards, such as fresh craters or mesas in which the rover might land safely inside or on top of, but could not traverse out of were also evaluated at all of the landing sites using slope maps from DEMs and surface materials identified in HiRISE images and the drive capabilities of the rover. Of the 161 potential such hazards only 14 are inescapable or probably inescapable and they cover only 0.01 % of the ellipse for Eberswalde and Mawrth and 0.2 % and 0.28 % at Gale and Holden, respectively. Finally, science related traversability issues were evaluated at all 4 landing sites. At Holden crater, ubiquitous ripples at the scale of the rover would likely reduce the flexibility in selecting the drive direction, similar to Opportunity preferentially driving down troughs between large ripples at Meridian Planum. The "go to" light-toned layered deposits exposed in trough walls south of the Holden ellipse are accessible by driving on the plains outside of the troughs and dipping into the troughs at key stratigraphic sections; giant eolian bedforms that dwarf the rover prevent driving within the troughs. At Gale crater, the key stratigraphic clay and sulfate layers are accessible via multiple traversable paths in the lowermost and low slope part of the central mound. Access to sulfates higher in the section would require driving into steep sided canyons with a number of potential choke points whose traversability cannot be positively known with available data. The fact that about 6 possible traversable pathways have been found suggests that an additional 5 km (straight line distance) of traverse into the mound can be accomplished, before ubiquitous steep slopes in the upper unit make driving impossible.

The final steps leading to selection of the Gale landing site included an MSL Science Team meeting, meetings of the Project Science Group and the MSL project, reviews by a NASA-appointed Independent Landing Site Certification Board and the NASA Planetary Protection Office, and two meetings at NASA Headquarters between the Project and the NASA selection official, the Associate Administrator for the Science Mission Directorate, and board of science division directors. Gale crater was selected over Eberswalde crater because of the greater diversity of geologic environments that could be explored for evidence related to habitability, including preserved organic carbon.

Acknowledgements Research described in this paper was partially done by the MSL project, Jet Propulsion Laboratory, California Institute of Technology, under a contract with the National Aeronautics and Space Administration and was supported by the Mars Data Analysis Program. Derived data products were sponsored by the Critical Data Products program administered by the JPL Mars Exploration Program office. We especially thank members of the Council of Atmospheres and Council of Terrains for work on characterizing MSL landing sites. We thank L. Redmond and N. Warner for help with the figures.

References

P. Aftabi, Laboratory testing of the ice-salt intrusions and extrusions in craters for determining Mars landing site, in *Lunar Planet. Sci.*, vol. XXXIX (Lunar and Planetary Institute, Houston, 2008). Abstract 1179

K. Ali, C. Vanelli, J. Biesiadecki, M. Maimone, Y. Cheng, M. San Martin, J. Alexander, Attitude and position estimation on the Mars Exploration Rovers, in *IEEE Systems, Man and Cybernetics Conference Proceedings*, Hawaii, USA, 10 October 2005

F.S. Anderson, A.F.C. Haldemann, N.T. Bridges, M.P. Golombek, T.J. Parker, G. Neumann, Analysis of MOLA data for the Mars Exploration Rover landing sites. J. Geophys. Res. **108**(E12), 8084 (2003). doi:10.1029/2003JE002125

J.A. Anderson, S.C. Sides, D.L. Soltesz, T.L. Sucharski, K.J. Becker, Modernization of the integrated software for imagers and spectrometers, in *Lunar Planet. Sci.*, vol. XXXV (Lunar and Planetary Institute, Houston, 2004). Abstract 2039

R.B. Anderson, J.F. Bell III, Geologic mapping and characterization of Gale Crater and implications for its potential as a Mars Science Laboratory landing site. Mars **5**, 76–128 (2010)

V. Ansan, N. Mangold, A. Lucas, A. Gendrin, S. Le Mouelic, F. Poulet, J.-P. Bibring, Omega Co-Investigator Team, Analysis of layered deposits in Terby Crater (Hellas region, Mars) using multiple datasets MOC, THEMIS and OMEGA/MEX, in *Lunar Planet. Sci.*, vol. XXXVII (Lunar and Planetary Institute, Houston, 2005). Abstract 1378

V. Ansan, D. Loizeau, N. Mangold, S. Le Mouélic, J. Carter, F. Poulet, G. Dromart, A. Lucas, J.-P. Bibring, A. Gendrin, B. Gondet, Y. Langevin, Ph. Masson, S. Murchie, J.F. Mustard, G. Neukum, Stratigraphy, mineralogy, and origin of layered deposits inside Terby crater, Mars. Icarus (2011). doi:10.1016/j.icarus.2010.09.011

R.E. Arvidson et al., Nature and origin of the hematite-bearing plains of Terra Meridiani based on analyses of orbital and Mars Exploration rover data sets. J. Geophys. Res. **111**, E12S08 (2006). doi:10.1029/2006JE002728

R. Arvidson et al., Mars Exploration Program 2007 Phoenix landing site selection and characteristics. J. Geophys. Res. **113**, E00A03 (2008). doi:10.1029/2007JE003021

J.L. Bandfield, V.E. Hamilton, P.R. Christensen, A global view of martian surface compositions from MGS-TES. Science **287**(5458), 1626–1630 (2000). doi:10.1126/science.287.5458.1626

J.L. Bandfield, D. Rogers, M.D. Smith, P.R. Christensen, Atmospheric correction and surface spectral unit mapping using thermal emission imaging system data. J. Geophys. Res. **109**, E10008 (2004). doi:10.1029/2004JE002289

R.A. Beyer, R.L. Kirk, Meter-scale slopes of candidate MSL landing sites from point photoclinometry. Space Sci. Rev., this issue

R.A. Beyer, A.S. McEwen, R.L. Kirk, Meter-scale slopes of candidate MER landing sites from point photoclinometry. J. Geophys. Res. **108**(E12), 8085 (2003). doi:10.1029/2003JE002120

P. Bhandari, G. Birur, M. Pauken, A. Paris, K. Novak, M. Prina, B. Ramirez, D. Bame, Mars Science Laboratory thermal control architecture, in *ICES 2005 Conference*, Rome, Italy, July 2005

J.P. Bhattacharya, T.H.D. Payenberg, S.D. Lang, M.C. Bourke, Dynamic river channels suggest a long-lived Noachian crater lake on Mars. Geophys. Res. Lett. **32**, L10201 (2005). doi:10.1029/2005GL022747

J.-P. Bibring, Y. Langevin, A. Gendrin, B. Gondet, F. Poulet, M. Berthé, A. Soufflot, R. Arvidson, N. Mangold, J. Mustard, P. Drossart, OMEGA team, Mars surface diversity as revealed by the OMEGA/Mars Express observations. Science **307**, 1576–1581 (2005)

J.-P. Bibring, Y. Langevin, J.F. Mustard, F. Poulet, R. Arvidson, A. Gendrin, B. Gondet, N. Mangold, P. Pinet, F. Forget, OMEGA team, Global mineralogical and aqueous Mars history derived from OMEGA/Mars Express data. Science **312**, 400–404 (2006). doi:10.1126/science.1122659

J.J. Biesiadecki, M.W. Maimone, The Mars Exploration Rover surface mobility flight software: Driving ambition, in *March 2006 IEEE Aerospace Conference Proceedings*, Big Sky, Montana, USA, 8 March 2006

J.J. Biesiadecki et al., Mars Exploration Rover surface operations: Driving opportunity at Meridiani Planum, in *October 2005 IEEE Systems, Man and Cybernetics Conference Proceedings*, Hawaii, USA, 10 October 2005

J.J. Biesiadecki, P.C. Leger, M.W. Maimone, Tradeoffs between directed and autonomous driving on the Mars Exploration Rovers. Int. J. Robot. Res. **26**(1), 91–104 (2007)
J. Biesiadecki, R. Liebersbach, M. Maimone, Mars Exploration Rover mobility and IDD downlink analysis tools, in *International Symposium on Artificial Intelligence, Robotics, and Automation for Space (i-SAIRAS) Proceedings*, Los Angeles, CA, 27 February 2008
D. Biggs, M. Andrews, Acceleration of iterative image restoration algorithms. J. Appl. Opt. **36**(8), 1766–1775 (1997)
J.L. Bishop, E.Z. Noe Dobrea, N.K. McKeown, M. Parente, B.L. Ehlmann, J.R. Michalski, R.E. Milliken, F. Poulet, G.A. Swayze, J.F. Mustard, S.L. Murchie, J.-P. Bibring, Phyllosilicate diversity and past aqueous activity revealed at Mawrth Vallis, Mars. Science **321**, 830–833 (2008). doi:10.1126/science.1159699
M.J. Broxton, L.J. Edwards, The Ames Stereo pipeline: Automated 3D surface reconstruction from orbital imagery, in *Lunar and Planetary Science*, vol. XXXIX (Lunar and Planetary Institute, Houston, 2008). Abstract #2419 (CD-ROM)
P. Brugarolas, M. San Martin, E. Wong, The RCS attitude controller for the exo-atmospheric and guided Entry phases of the Mars Science Laboratory, in *International Planetary Probe Workshop*, Barcelona, Spain (2010)
B.J. Butler, The 3.5-cm radar investigation of Mars and Mercury: Planetological implications. Ph.D. Thesis, California Institute of Technology, Pasadena, CA, 1994, 28
N.A. Cabrol, H.E. Newson, R. Landheim, C.P. McKay, Hydrogeologic evolution of Gale crater and its relevance to the exobiological exploration of Mars. Icarus **139**, 235–245 (1999)
B. Cantor, P.B. James, M. Caplinger, M.J. Wolf, Martian dust storms: 1999 Mars Orbiter Camera observations. J. Geophys. Res. **106**, 23653–23688 (2001)
J. Carsten, A. Rankin, D. Ferguson, A. Stentz, Global path planning on board the Mars Exploration Rovers, in *Proceedings of the 2007 IEEE Aerospace Conference*, March 2007
A. Chen, A. Vasavada, A. Cianciolo, J. Barnes, D. Tyler, S. Rafkin, D. Hinson, S. Lewis, Atmospheric risk assessment for the Mars Science Laboratory entry, descent, and landing system, in *IEEE Aerospace Conference*, Big Sky, MT (2010). IEEEAC paper#1153
Y. Cheng, A.E. Johnson, L.H. Matthies, C.F. Olson, Optical landmark detection for spacecraft navigation, in *AAS/AIAA Astrodynamics Specialist Conference*, Ponce, Puerto Rico (2003). http://trs-new.jpl.nasa.gov/dspace/handle/2014/6431
Y. Cheng, M. Maimone, L. Matthies, Visual odometry on the Mars Exploration Rovers, in *IEEE Conference on Systems, Man and Cybernetics*, The Big Island, Hawaii, USA, October 2005
Y. Cheng, M. Maimone, L. Matthies, Visual odometry on the Mars Exploration Rovers. IEEE Robot. Autom. Mag. **13**(2), 54–62 (2006)
P.R. Christensen, Martian dust mantling and surface composition: Interpretation of thermophysical properties. J. Geophys. Res. **87**, 9985–9998 (1982)
P.R. Christensen, The spatial distribution of rocks on Mars. Icarus **68**, 217–238 (1986a)
P.R. Christensen, Regional dust deposits on Mars: Physical properties, age, and history. J. Geophys. Res. **91**, 3533–3545 (1986b)
P.R. Christensen, Aqueous mineral deposits in an ancient, channeled, equatorial terrain. Abstract Submitted for a New MSL Landing Site to the Landing Site Steering Committee, Aug. 22, 2009, posted at https://marsoweb.nas.nasa.gov/landingsites/
P.R. Christensen, M.C. Malin, High resolution thermal imaging of Mars (abs.), in *Lunar Planet. Sci.*, vol. XIX (Lunar and Planetary Institute, Houston, 1988), pp. 180–181
P.R. Christensen, H.J. Moore, The martian surface layer, in *MARS*, ed. by H.H. Kieffer, B.M. Jakosky, C.W. Snyder, M.S. Matthews (University of Arizona Press, Tucson, 1992), pp. 686–727
P.R. Christensen, D.L. Anderson, S.C. Chase, R.N. Clark, H.H. Kieffer, M.C. Malin, J.C. Pearl, J. Carpenter, N. Bandiera, F.G. Brown, S. Silverman, Thermal Emission Spectrometer experiment: Mars Observer Mission. J. Geophys. Res. **97**(E5), 7719–7734 (1992)
P.R. Christensen et al., Mars Global Surveyor Thermal Emission Spectrometer experiment: Investigation description and surface science results. J. Geophys. Res. **106**, 23823–23871 (2001)
P.R. Christensen, B.M. Jakosky, H.H. Kieffer, M.C. Malin, H.Y. McSween Jr., K. Nealson, G.L. Mehall, S.H. Silverman, S. Ferry, M. Caplinger, M. Ravine, The Thermal Emission Imaging System (THEMIS) for the Mars 2001 Odyssey mission. Space Sci. Rev. **110**, 85–130 (2004)
G. Dromart, C. Quantin, O. Broucke, Stratigraphic architectures spotted in southern Melas Chasma, Vallis Marineris, Mars. Geology **35**(4), 363–366 (2007)
K.S. Edgett, The sedimentary rocks of Sinus Meridiani: Five key observations from data acquired by the Mars Global Surveyor and Mars Odyssey orbiters. Mars **1**, 5–58 (2005). doi:10.1555/mars.2005.0002
B.L. Ehlmann, J.F. Mustard, C.I. Fassett, S.C. Schon, J.W. Head III, D.J. Des Marais, J.A. Grant, S.L. Murchie, CRISM team, Clay mineralogy and organic preservation potential of lacustrine sediments from a Martian delta environment, Jezero crater, Nili Fossae, Mars. Nat. Geosci. **1** (2008a). doi:10.1038/ngeo207

B.L. Ehlmann, J.F. Mustard, S.L. Murchie, F. Poulet, J.L. Bishop, A.J. Brown, W.M. Calvin, R.N. Clark, D.J. Des Marias, R.E. Milliken, L.H. Roach, T.L. Roush, G.A. Swayze, J.J. Wray, Orbital identification of carbonate-bearing rocks on Mars. Science **322**, 1828–1832 (2008b). doi:10.1126/science.1164759

B.L. Ehlmann, J.F. Mustard, G.A. Swayze, R.N. Clark, J.L. Bishop, F. Poulet, D.J. Des Marais, L.H. Roach, R.E. Milliken, J.J. Wray, O. Barnouin-Jha, S.L. Murchie, Identification of hydrated silicate minerals on Mars using MRO-CRISM: Geologic context near Nili Fossae and implications for aqueous alteration. J. Geophys. Res. **114**, E00D08 (2010). doi:10.1029/2009JE003339

E.S. Eliason et al., Software interface specification for HiRISE reduced data record products. MRO JPL Document D-32006, 2009, online at http://hirise.lpl.arizona.edu/pdf/HiRISE_RDR_v12_DTM_11_25_2009.pdf

W.H. Farrand, T.D. Glotch, J.W. Rice Jr., J.A. Hurowitz, G.A. Swayze, Discovery of jarosite within the Mawrth Vallis region of Mars: Implications for the geologic history of the region. Icarus **204**(2), 478–488 (2009)

C.I. Fassett, J.W. Head, Fluvial sedimentary deposits on Mars: Ancient deltas in a crater lake in the Nili Fossae region. Geophys. Res. Lett. **32**, L14201 (2005). doi:10.1029/2005GL023456

R.L. Fergason et al., THEMIS thermal inertia of the MSL landing sites. Space Sci. Rev., this issue

R.L. Fergason, P.R. Christensen, J.F. Bell III, M.P. Golombek, K.E. Herkenhoff, H.H. Kieffer, Physical properties of the Mars Exploration Rover landing sites as inferred from Mini-TES derived thermal inertia. J. Geophys. Res. **111**(E2), E02S21 (2006b). doi:10.1029/2005JE002583

R.L. Fergason, P.R. Christensen, H.H. Kieffer, High-resolution thermal inertia derived from the Thermal Emission Imaging System (THEMIS): Thermal model and applications. J. Geophys. Res. **111**, E12004 (2006a). doi:10.1029/2006JE002735

J.B. Garvin, J.J. Frawley, J.B. Abshire, Vertical roughness of Mars from Mars Orbiter Laser Altimeter. Geophys. Res. Lett. **26**, 381–384 (1999)

S.B. Goldberg, M.W. Maimone, L. Matthies, Stereo vision and rover navigation software for planetary exploration, in *March 2002 IEEE Aerospace Conference Proceedings*, Big Sky, Montana, USA, vol. 5 (2002), pp. 2025–2036. doi:10.1109/AERO.2002.1035370

M. Golombek, D. Rapp, Size-frequency distributions of rocks on Mars and Earth analog sites: Implications for future landed missions. J. Geophys. Res. **102**, 4117–4129 (1997)

M.P. Golombek, R.A. Cook, H.J. Moore, T.J. Parker, Selection of the Mars Pathfinder landing site. J. Geophys. Res. **102**, 3967–3988 (1997a)

M.P. Golombek et al., Overview of the Mars Pathfinder mission and assessment of landing site predictions. Science **278**, 1743–1748 (1997b)

M.P. Golombek, H.J. Moore, A.F.C. Haldemann, T.J. Parker, J.T. Schofield, Assessment of Mars Pathfinder landing site predictions. J. Geophys. Res. **104**, 8585–8594 (1999)

M.P. Golombek et al., Selection of the Mars Exploration Rover landing sites. J. Geophys. Res. **108**(E12), 8072 (2003a). doi:10.1029/2003JE002074, 48pp.

M.P. Golombek et al., Rock size-frequency distributions on Mars and implications for MER landing safety and operations. J. Geophys. Res. **108**(E12), 8086 (2003b). doi:10.1029/2002JE002035

M.P. Golombek et al., Assessment of Mars Exploration Rover landing site predictions. Nature **436** (2005). doi:10.1038/nature03600

M. Golombek, J. Grant, L. Lorenzoni, A. Steltzner, A.R. Vasavada, C. Voorhees, M. Watkins M, Preliminary constraints and plans for Mars Science Laboratory landing site selection, in *Lunar and Planetary Science*, vol. XXXVII (Lunar and Planetary Institute, Houston, 2006a). Abstract #2172 (CD-ROM)

M.P. Golombek et al., Geology of the Gusev cratered plains from the Spirit rover transverse. J. Geophys. Res. **111**, E02S07 (2006b). doi:10.1029/2005JE002503

M. Golombek, J. Grant, A.R. Vasavada, M. Watkins, Landing sites proposed for the Mars Science Laboratory mission, in *Lunar and Planetary Science*, vol. XXXVIII (Lunar and Planetary Institute, Houston, 2007a). Abstract #1392 (CD-ROM)

M. Golombek, J. Grant, A.R. Vasavada, M. Watkins, L. Lorenzoni, J. Griffes, Preliminary constraints, plans and proposed landing sites for the Mars Science Laboratory mission, in *The Seventh International Conference on Mars*, Pasadena, CA, July 9–13, 2007 (Lunar and Planetary Institute, Houston, 2007b). Abstract #3037 (CD-ROM)

M.P. Golombek et al., Size-frequency distributions of rocks on the northern plains of Mars with special reference to Phoenix landing surfaces. J. Geophys. Res. **113**, E00A09 (2008a). doi:10.1029/2007JE003065

M.P. Golombek, A.F.C. Haldemann, R.A. Simpson, R.L. Fergason, N.E. Putzig, R.E. Arvidson, J.F. Bell III, M.T. Mellon, Martian surface properties from joint analysis of orbital, Earth-based, and surface observations, in *The Martian Surface: Composition, Mineralogy and Physical Properties*, ed. by J.F. Bell III (Cambridge University Press, Cambridge, 2008b), pp. 468–497. Chap. 21

M. Golombek, J. Grant, A.R. Vasavada, M. Watkins, E. Noe Dobrea, J. Griffes, T. Parker, Downselection of landing sites for the Mars Science Laboratory, in *Lunar and Planetary Science*, vol. XXXIX (Lunar and Planetary Institute, Houston, 2008c). Abstract #2181 (CD-ROM)

M. Golombek, J. Grant, A.R. Vasavada, J. Grotzinger, M. Watkins, D. Kipp, E. Noe Dobrea, J. Griffes, T. Parker, Selection of four landing sites for the Mars Science Laboratory, in *Lunar and Planetary Science*, vol. XL (Lunar and Planetary Institute, Houston, 2009a). Abstract #1404 (CD-ROM)

M.P. Golombek, A.F.C. Haldemann, R.A. Simpson, R.L. Fergason, N.E. Putzig, A. Huertas, R.E. Arvidson, T. Heet, J.F. Bell III, M.T. Mellon, A.S. McEwen, Relationships between remote sensing data and surface properties of Mars landing sites, in *40th Lunar and Planetary Science Conference* (Lunar and Planetary Institute, Houston, 2009b). Abstract 1409 (CD-ROM)

M. Golombek, J. Grant, A.R. Vasavada, J. Grotzinger, M. Watkins, D. Kipp, E. Noe Dobrea, J. Griffes, T. Parker, R. Kirk, R. Fergason, R. Beyer, A. Huertas, R. Milliken, Y. Sun, Landing sites under consideration for Mars Science Laboratory, in *41st Lunar and Planetary Science* (Lunar and Planetary Institute, Houston, 2010). Abstract #2407 (CD-ROM)

M.P. Golombek, A. Huertas, D. Kipp, Rocks and rock size-frequency distributions at the Mars Science Laboratory landing sites, in *42nd Lunar and Planetary Science* (Lunar and Planetary Institute, Houston, 2011a). Abstract #1547

M. Golombek, J. Grant, A.R. Vasavada, J. Grotzinger, M. Watkins, D. Kipp, E. Noe Dobrea, J. Griffes, T. Parker, Final four landing sites for the Mars Science Laboratory, in *42nd Lunar and Planetary Science* (Lunar and Planetary Institute, Houston, 2011b). Abstract #1520

M. Golombek, A. Huertas, D. Kipp, F. Calef, Detection and characterization of rocks and rock distribution at the Mars Science Laboratory Landing Sites. Mars (2012), submitted

J.A. Grant, T.J. Parker, Drainage evolution of the Margaritifer Sinus region, Mars. J. Geophys. Res. **107**, 5066 (2002). doi:10.1029/2001JE001678

J.A. Grant, S.A. Wilson, Late alluvial fan formation in southern Margaritifer Terra, Mars. Geophys. Res. Lett. **38**, L08201 (2011). doi:10.1029/2011GL046844

J.A. Grant, R.P. Irwin III, J.P. Grotzinger, R.E. Milliken, L.L. Tornabene, A.S. McEwen, C.M. Weitz, S.W. Squyres, T.D. Glotch, B.J. Thomson, HiRISE imaging of impact megabreccia and sub-meter aqueous strata in Holden Crater, Mars. Geology **36**, 195–198 (2008). doi:10.1130/G24340A

J.A. Grant, M.P. Golombek, J. Grotzinger, S.A. Wilson, M. Watkins, A.R. Vasavada, J. Griffes, T. Parker, The science process for selecting the landing site for the 2011 Mars Science Laboratory. Planet. Space Sci. (2010a). doi:10.1016/j.pss.2010.06.016

J.A. Grant, R.P. Irwin III, S.A. Wilson, Aqueous depositional settings in Holden crater, Mars, in *Lakes on Mars*, ed. by N.A. Cabrol, E.A. Grin (Elsevier, Oxford, 2010b). Chap. 12

J.A. Grant, R.P. Irwin III, S.A. Wilson, D. Buczkowski, K. Siebach, A lake in Uzboi Vallis and implications for Late Noachian-Early Hesperian climate on Mars. Icarus **212**(1), 110–122 (2011)

J. Grotzinger, Beyond water on Mars. Nat. Geosci. **2**, 231–233 (2009). doi:10.1038/ngeo480

J. Grotzinger et al., Mars Science Laboratory Mission and science investigation. Space Sci. Rev., this issue. doi:10.1007/s11214-012-9892-2

K. Gwinner, F. Scholten, R. Jaumann, T. Roatsch, J. Oberst, G. Neukum, Global mapping of Mars by systematic derivation of Mars Express HRSC high-resolution digital elevation models and orthoimages, in *ISPRS IV/7 Extraterrestrial Mapping Workshop*, Houston, TX (2007)

K. Gwinner, F. Scholten, M. Spiegel, R. Schmidt, B. Giese, J. Oberst, R. Jaumann, C. Heipke, G. Neukum, Derivation and validation of high-resolution digital terrain models from Mars Express HRSC-data. Photogramm. Eng. Remote Sens. **75**(9), 1127–1141 (2009)

K. Gwinner, J. Oberst, R. Jaumann, G. Neukum, Regional HRSC multi-orbit digital terrain models for the Mars Science Laboratory candidate landing sites, in *41st Lunar and Planetary Science Conference* (Lunar and Planetary Institute, Houston, 2010a). Abstract 2727 (CD-ROM)

K. Gwinner et al., Topography of Mars from global mapping by HRSC high-resolution digital terrain models and orthoimages: Characteristics and performance. Earth Planet. Sci. Lett. **294**, 506 (2010b)

T. Hagfors, Backscattering from an undulating surface with applications to radar returns from the Moon. J. Geophys. Res. **69**, 3779–3784 (1964)

A.F.C. Haldemann, D.L. Mitchell, R.F. Jurgens, M.A. Slade, D.O. Muhleman, Mars Pathfinder landing site assessment with Goldstone delay-Doppler and CW radar experiments. J. Geophys. Res. **102**, 4097–4106 (1997)

J.K. Harmon, R.E. Arvidson, E.A. Guinness, B.A. Campbell, M.A. Slade, Mars mapping with delay-Doppler radar. J. Geophys. Res. **104**, 14065–14089 (1999)

M.H. Hecht, A.R. Vasavada, Transient liquid water near an artificial heat source on Mars. Mars **2**, 83–96 (2006). doi:10.1555/mars.2006.0006

T.L. Heet, R.E. Arvidson, S.C. Cull, M.T. Mellon, K.D. Seelos, Geomorphic and geologic settings of the Phoenix Lander mission landing site. J. Geophys. Res. **114**, E00E04 (2009). doi:10.1029/2009JE003416

S.W. Hobbs, D.J. Paull, M.C. Bourke, Aeolian processes and dune morphology in Gale Crater. Icarus **210**, 102–115 (2010). doi:10.1016/j.icarus.2010.06.006

T.J. Holmes et al., Light microscopic images reconstructed by maximum likelihood, in *Handbook of Biological Confocal Microscopy*, ed. by J.B. Pawley (Plenum Press, New York, 1995)
B.M. Hynek, R.J. Phillips, The stratigraphy of Meridiani Planum, Mars, and implications for the layered deposits' origin. Earth Planet. Sci. Lett. **274**, 214–220 (2008)
B.M. Hynek, R.E. Arvidson, R.J. Phillips, Geologic setting and origin of Terra Meridiani hematite deposit on Mars. J. Geophys. Res. **107**, 5088 (2002). doi:10.1029/2002JE001891
R. Irwin, An overview of the setting of Holden crater. Presentation at the 4th MSL Landing Site Workshop, Sept. 27–29, 2010, in Monrovia, CA. https://marsoweb.nas.nasa.gov/landingsites/msl/workshops/4th_workshop/talks/1_Irwin_Holden.pdf
R.P. Irwin III, J.A. Grant, Geologic Map of MTM-15027, -20027, -25027, -25032 Quadrangles, Margaritifer Terra region of Mars. U.S. Geol. Surv. Scientific Investigations Map, scale 1:500,000, 2011
B.M. Jakosky, The effects of nonideal surfaces on the derived thermal properties of Mars. J. Geophys. Res. **84**(B14), 8252–8262 (1979)
B.M. Jakosky, P.R. Christensen, Global duricrust on Mars: Analysis of remote-sensing data. J. Geophys. Res. **91**, 3547–3559 (1986)
D.J. Jerolmack, D. Mohrig, M.T. Zuber, S. Byrne, A minimum time for the formation of Holden northeast fan, Mars. Geophys. Res. Lett. **31**, L21701 (2004). doi:10.1029/2004GL021326
H.H. Kieffer, S.C. Chase Jr., E. Miner, G. Münch, G. Neugebauer, Preliminary report on infrared radiometric measurements from the Mariner 9 spacecraft. J. Geophys. Res. **78**(20), 4291–4312 (1973)
H.H. Kieffer, T.Z. Martin, A.R. Peterfreund, B.M. Jakosky, E.D. Miner, F.D. Palluconi, Thermal and albedo mapping of Mars during the Viking primary mission. J. Geophys. Res. **82**(28), 4249–4291 (1977)
J.R. Kim, J.P. Muller, Multi-resolution topographic data extraction from Martian stereo imagery. Planet. Space Sci. **57**(14–15), 2095–2112 (2009). doi:10.1016/j.pss.2009.09.024
D. Kipp, Terrain safety assessment in support of the Mars Science Laboratory mission, in *IEEE Aerospace Conference*, Big Sky, MT (2012). doi:10.1109/AERO.2012.6186995
D. Kipp, M. San Martin, J. Essmiller, D. Way, Mars Science Laboratory entry, descent and landing triggers, in *IEEE Aerospace Conference*, Big Sky, MT (2007). IEEAC paper #1445
R. Kirk et al., High-resolution topomapping of candidate MER landing sites with Mars Orbiter Camera narrow angle images. J. Geophys. Res. **108**(E12), 8088 (2003). doi:10.1029/2003JE002131
R.L. Kirk et al., Ultrahigh resolution topographic mapping of Mars with MRO HiRISE stereo images: Meter-scale slopes of candidate Phoenix landing sites. J. Geophys. Res. **113**, E00A24 (2008). doi:10.1029/2007JE003000
R.L. Kirk, E. Howington-Kraus, D. Galuszka, B. Redding, J. Antonsen, K. Coker, E. Foster, M. Hopkins, A. Licht, A. Fennema, F. Calef III, S. Nuti, T.J. Parker, M.P. Golombek, "Wall to wall" 1-m topographic coverage of the Mars Science Laboratory candidate landing sites, in *42nd Lunar and Planetary Science Conference* (2011a). Abstract #2407
R.L. Kirk et al., Near-complete 1-m topographic models of the MSL candidate landing sites: Site safety and quality evaluation, in *European Planetary Science Conference*, vol. 6, (2011b). Abstract EPSC2011-1465
A. Kleinbohl et al., Mars Climate Sounder limb profile retrieval of atmospheric temperature, pressure, and dust and water ice opacity. J. Geophys. Res. **114**, E10006 (2009). doi:10.1029/2009JE003358
K.W. Larsen, R.F. Jurgens, A.F.C. Haldemann, M.A. Slade, H.C. Rumsey Jr., Terrestrial quadstatic interferometric radar observations of Mars. IEEE Trans. Geosci. Remote Sens. **48**(6), 2670–2684 (2010). doi:10.1109/TGRS.2010.2040084
P.C. Leger et al., Mars Exploration Rover surface operations: Driving Spirit at Gusev crater, in *October 2005 IEEE Systems, Man and Cybernetics Conference Proceedings*, Hawaii, USA, 10 October 2005
K.W. Lewis, O. Aharonson, Stratigraphic analysis of the distributary fan in Eberswalde crater using stereo imagery. J. Geophys. Res. **111**, E06001 (2006). doi:10.1029/2005JE002555
D. Loizeau, N. Mangold, F. Poulet, J.-P. Bibring, A. Gendrin, V. Ansan, C. Gomez, B. Gondet, Y. Langevin, P. Masson, G. Neukum, Phyllosilicates in the Mawrth Vallis region of Mars. J. Geophys. Res. **112**, E08S08 (2007). doi:10.1029/2006JE002877
D. Loizeau, N. Mangold, F. Poulet, V. Ansan, E. Hauber, J.-P. Bibring, B. Gondet, Y. Langevin, P. Masson, G. Neukum, Stratigraphy in the Mawrth Vallis region through OMEGA, HRSC color imagery and DTM. Icarus **205**, 396 (2010). doi:10.1016/j.icarus.2009.04.018
M. Maimone, J. Morrison, Rover navigation 101: Autonomous rover navigation. JPL Mars Exploration Rover website, January 13, 2004
M. Maimone, J. Biesiadecki, E. Tunstel, Y. Cheng, C. Leger, Surface navigation and mobility intelligence on the Mars Exploration Rovers, in *Intelligence for Space Robotics*, March (TSI Press, San Antonio, 2006), pp. 45–69. Chap. 3
M. Maimone, Y. Cheng, L. Matthies, Two years of visual odometry on the Mars Exploration Rovers. J. Field Robot. **24**(3), 169–186 (2007a)

M.W. Maimone, P.C. Leger, J.J. Biesiadecki, Overview of the Mars Exploration Rovers' autonomous mobility and vision capabilities, in *IEEE International Conference on Robotics and Automation (ICRA) Space Robotics Workshop*, Rome, Italy, 14 April 2007b

M.C. Malin, K.S. Edgett, Sedimentary Rocks of Early Mars. Science **290**(5498), 1927–1937 (2000)

M.C. Malin, K.S. Edgett, Mars Global Surveyor Mars Orbiter Camera: Interplanetary cruise through primary mission. J. Geophys. Res. **106**, 23429–23570 (2001a)

M.C. Malin, K.S. Edgett, Rock stratigraphy in Gale crater, Mars, in *32nd Lunar and Planetary Science Conference*, (Lunar and Planetary Institute, Houston, 2001b). Abstract #1005

M.C. Malin, K.S. Edgett, Evidence for persistent flow and aqueous sedimentation on Mars. Science **302**, 1931–1934 (2003). doi:10.1126/science.10905444

M.C. Malin et al., Context Camera Investigation on board the Mars Reconnaissance Orbiter. J. Geophys. Res. **112**, E05S04 (2007). doi:10.1029/2006JE002808

N. Mangold, F. Poulet, J.F. Mustard, J.-P. Bibring, B. Bondet, Y. Langevin, V. Ansan, P. Masson, C. Fasset, J.W. Head, H. Hoffmann, G. Neukum, Mineralogy of the Nili Fossae region with OMEGA/Mars Express data: 2. Aqueous alteration of the crust. J. Geophys. Res. **112**, E08S04 (2007). doi:10.1029/2006JE002835

N. Mangold, V. Ansan, P. Masson, C. Vincendon, Estimate of the aeolian dust thickness in Arabia Terra, Mars: Implications of a thick mantle (20 m) for hydrogen detection. Géomorph. Relief Process. Environ. **1**, 23–32 (2009)

H. Masursky, N.L. Crabill, The Viking landing sites: Selection and certification. Science **193**, 809–812 (1976a)

H. Masursky, N.L. Crabill, Search for the Viking 2 landing site. Science **194**, 62–68 (1976b)

H. Masursky, N.L. Crabill, Viking site selection and certification. NASA SP-429, 34pp., 1981

L.M. Matthies et al., Computer Vision on Mars. Int. J. Comput. Vis. (2007a). doi:10.1007/s11263-007-0046-z

L. Matthies, M. Maimone, Y. Cheng, A. Johnson, R. Willson, Computer vision in the Mars Exploration Rover (MER) mission, in *Computational Vision in Neural and Machine Systems* (Cambridge University Press, Cambridge, 2007b), pp. 71–84. ISBN 978-0-521-86260-8. Chap. 4

S. Mattson, A. Boyd, R.L. Kirk, D.A. Cook, E. Howington-Kraus, HiJACK: Correcting spacecraft jitter in HiRISE images of Mars, in *European Planetary Science Conference*, vol. 4 (2009). Abstract EPSC2009-0604

A.S. McEwen et al., Mars Reconnaissance Orbiter's High Resolution Imaging Science Experiment (HiRISE). J. Geophys. Res. **112**, E05S02 (2007). doi:10.1029/2005JE002605

A.S. McEwen et al., The High Resolution Imaging Science Experiment (HiRISE) during MRO's Primary Science Phase (PSP). Icarus **205**, 2–37 (2010). doi:10.1016/j.icarus.2009.04.023

N.K. McKeown et al., Characterization of phyllosilicates observed in the central Mawrth Vallis region, Mars, their potential formational processes, and implications for past climate. J. Geophys. Res. **114**, E00D10 (2009)

M.T. Mellon, B.M. Jakosky, H.H. Kieffer, P.R. Christensen, High-resolution thermal inertia mapping from the Mars Global Surveyor Thermal Emission Spectrometer. Icarus **148**, 437–455 (2000)

M.T. Mellon, W.C. Feldman, T.H. Prettyman, The presence and stability of ground ice in the southern hemisphere of Mars. Icarus **169**, 324–340 (2004). doi:10.1016/j.icarus.2003.10.022

M.T. Mellon et al., The thermal inertia of the surface of Mars, in *The Martian Surface: Composition, Mineralogy and Physical Properties*, ed. by J.F. Bell III (Cambridge University Press, Cambridge, 2008), pp. 399–427. Chap. 19

G.F. Mendeck, L.E. Craig, Entry guidance for the 2011 Mars Science Laboratory Mission, in *AIAA Atmospheric Flight Mechanics Conference and Exhibit*, Portland, Oregon Aug. 8–11 2011. AIAA 2011-6639

MEPAG, Special Regions Science Analysis Group et al., Findings of the Mars Special Regions Science Analysis Group. Astrobiology **6**, 677–732 (2006). doi:10.1089/ast.2006.6.677

J.M. Metz, J.P. Grotzinger, D. Mohrig, R. Milliken, B. Prather, C. Pirmez, A.S. McEwen, C.M. Weitz, Sublacustrine depositional fans in southwest Melas Chasma. J. Geophys. Res. **114**, E10002 (2009). doi:10.1029/2009JE003365

J.R. Michalski, E.Z.N. Noe Dobrea, Evidence for a sedimentary origin of clay minerals in the Mawrth Vallis region, Mars. Geology **35**, 830–833 (2007). doi:10.1130/G23854A.1

J. Michalski, F. Poulet, J.-P. Bibring, N. Mangold, Analysis of phyllosilicate deposits in the Nili Fossae region of Mars: Comparison of TES and OMEGA data. Icarus **206**, 269–289 (2010a). doi:10.1016/j.icarus.2009.09.006

J.R. Michalski et al., The Mawrth Vallis region of Mars: A potential landing site for the Mars Science Laboratory (MSL) mission. Astrobiology **10**(7), 687–703 (2010b)

S.B. Miller, A.S. Walker, Further developments of Leicadigital photogrammetric systems by Helava. ACSM/ASPRS Annu. Conv. Expo. Tech. Pap. **3**, 256–263 (1993)

S.B. Miller, A.S. Walker, Die Entwicklung der digitalen photogrammetrischen Systeme von Leica und Helava. Z. Photogramm. Fernerkund. **63**(1), 4–16 (1995)
R.E. Milliken, D. Bish, Sources and sinks of clay minerals on Mars. Philos. Mag. **90**(17), 2293–2308 (2010)
R.E. Milliken, J. Grotzinger, J.A. Grant, R. Arvidson, S. Murchie, Understanding sedimentary sources and sinks on Mars from orbit. Geol. Soc. Am. Prog. Abstr. (2008). Abstract 134-1
R.E. Milliken, J.P. Grotzinger, B.J. Thomson, Paleoclimate of Mars as captured by the stratigraphic record in Gale crater. Geophys. Res. Lett. **37**, L04201 (2010). doi:10.1029/2009GL041870
J.M. Moore, A.D. Howard, Large alluvial fans on Mars. J. Geophys. Res. **110**, E04005 (2005). doi:10.1029/2005JE002352
H.J. Moore, B.M. Jakosky, Viking landing sites, remote-sensing observations, and physical properties of martian surface materials. Icarus **81**, 164–184 (1989)
J.M. Moore, A.D. Howard, W.D. Dietrich, P.M. Schenk, Martian layered fluvial deposits: implications for Noachian climate scenarios. Geophys. Res. Lett. **30**, E06001 (2003). doi:10.1029/2003GL019002
MSL Project, MSL landing site selection user's guide to engineering constraints. The Mars Science Laboratory Project Document, Jet Propulsion Laboratory, Pasadena, CA, vol. 4.5, 2007, 15 pp.
S. Murchie et al., Compact Reconnaissance Imaging Spectrometer for Mars (CRISM) on Mars Reconnaissance Orbiter (MRO). J. Geophys. Res. **112**, E05S03 (2007). doi:10.1029/2006JE002682
J.F. Mustard, B.L. Ehlmann, Three distinct habitable environments defined by aqueous alteration traversing the alkaline-acidic transition. Abstract submitted for a New MSL Landing Site to the Landing Site Steering Committee, Aug. 22, 2009, posted at https://marsoweb.nas.nasa.gov/landingsites/
J.F. Mustard et al., Hydrated silicate minerals on Mars observed by the Mars Reconnaissance Orbiter CRISM instrument. Nature **454**, 305–309 (2008). doi:10.1038/nature07097
J.F. Mustard, B.L. Ehlmann, S.L. Murchie, F. Poulet, N. Mangold, J.W. Head, J.-P. Bibring, L.H. Roach, Composition, morphology, and stratigraphy of Noachain/Phyllosian crust around the Isidis Basin. J. Geophys. Res. **114**, E00D12 (2010). doi:10.1029/2009JE003349
G.A. Neumann, J.B. Abshire, O. Aharonson, J.B. Garvin, X. Sun, M.T. Zuber, Mars Orbiter Laser Altimeter pulse width measurements and footprint scale roughness. Geophys. Res. Lett. **30**, 1561–1565 (2003)
H.E. Newsom, N.L. Lanza, A.M. Ollila, S.M. Wiseman, T.L. Roush, G.A. Marzo, L.L. Tornabene, C.H. Okubo, M.M. Osterloo, V.E. Hamilton, L.S. Crumpler, Inverted channel deposits on the floor of Miyamoto crater, Mars. Icarus **205**, 64–72 (2010). doi:10.1016/j.icarus.2009.03.030
E.Z. Noe Dobrea et al., Mineralogy and stratigraphy of phyllossilicate-bearing and dark mantling units in the greater Mawrth Vallis/west Arabia Terra area: Constraints on geological origin. J. Geophys. Res. (2010). doi:10.1029/2009JE003351
E.Z. Noe Dobrea, J. Michalski, G. Swayze, Aqueous mineralogy and stratigraphy at and around the proposed Mawrth Vallis MSL Landing Site: New insights into the aqueous history of the region, Mars. Mars **6**, 32–46 (2011)
K.S. Novak, Y. Liu, C.-J. Lee, S. Hendricks, Mars Science Laboratory Rover actuator thermal design, in *40th ICES Conference*, Barcelona, Spain, July 2010
S.A. Nowicki, P.R. Christensen, Rock abundance on Mars from the Thermal Emission Spectrometer. J. Geophys. Res. **112**, E05007 (2007). doi:10.1029/2006JE002798
T. Ojala, M. Pietikainen, Unsupervised texture segmentation using feature distributions. Pattern Recognit. **32**, 477–486 (1999)
M.M. Osterloo, V.E. Hamilton, J.L. Bandfield, T.D. Glotch, A.M. Baldridge, P.R. Christensen, L.L. Tornabene, F.S. Anderson, Chloride-bearing materials in the southern highlands of Mars. Science **319**(5870), 1651–1654 (2008). doi:10.1126/science.1150690
M.M. Osterloo, F.S. Anderson, V.E. Hamilton, B.M. Hynek, Geologic context of proposed chloride- bearing materials on Mars. J. Geophys. Res. **115**, E10012 (2010). doi:10.1029/2010JE003613
F.D. Palluconi, H.H. Kieffer, Thermal inertia mapping of Mars from 60°S to 60°N. Icarus **45**, 415–426 (1981)
T.J. Parker, M.P. Golombek, M.W. Powell, Geomorphic/geologic mapping, localization, and traverse planning at the Opportunity landing site, Mars, in *41st Lunar Planet. Sci.* (Lunar and Planetary Institute, Houston, 2010). Abstract #2638 (CD-ROM)
S.M. Pelkey, B.M. Jakosky, Surficial geologic surveys of Gale Crater and Melas Chasma, Mars: Integration of remote-sensing data. Icarus **160**, 228–257 (2002)
S.M. Pelkey, B.M. Jakosky, P.R. Christensen, Surficial properties in Gale Crater, Mars from Mars Odyssey THEMIS data. Icarus **167**, 244–270 (2004)
L.K. Pleskot, E.D. Miner, Time variability of Martian bolometric albedo. Icarus **45**, 179–201 (1981)
B.D. Pollard, C.W. Chen, The radar terminal descent sensor for the Mars Science Laboratory mission, in *Proceedings of the Aerospace Engineering Symposium*, Big Sky, MT (2009). doi:10.1109/AERO.2009.4839463
M. Pondrelli, A. Baliva, S. Di Lorenzo, L. Marinangeli, A.P. Rossi, Complex evolution of paleolacustrine systems on Mars: An example from the Holden crater. J. Geophys. Res. **110**, E04016 (2005). doi:10.1029/2004JE002335

M. Pondrelli, A. Pio Rossi, L. Marinangeli, E. Hauber, A. Baliva, An application of sequence stratigraphy to Mars: The Eberswalde fan delta. GeoActa **1**, 237–253 (2008). Special Publication

C. Popa, F. Esposito, L. Colangeli, New landing site proposal for Mars Science Laboratory (MSL) in Xanthe Terra, in *Lunar Planet. Sci.*, vol. XLI (Lunar and Planetary Institute, Houston, 2010) Abstract 1807

F. Poulet, J.-P. Bibring, J.F. Mustard, A. Gendrin, N. Mangold, Y. Langevin, R.E. Arvidson, B. Gondet, C. Gomez (OMEGA Team), Phyllosilicates on Mars and implications for the early Mars history. Nature **438**, 623–628 (2005)

F. Poulet, C. Gomez, J.-P. Bibring, Y. Langevin, B. Gondet, P. Pinet, G. Belluci, J. Mustard, Martian surface mineralogy from Observatoire pour la Minéralogie, l'Eau, les Glaces et l'Activité on board the Mars Express spacecraft (OMEGA/MEx): Global mineral maps. J. Geophys. Res. **112**, E08S02 (2007). doi:10.1029/2006JE002840

F. Poulet, R.E. Arvidson, C. Gomez, R.V. Morris, J.-P. Bibring, Y. Langevin, B. Gondet, J. Griffes, Mineralogy of Terra Meridiani and western Arabia Terra from OMEGA/MEx and implications for their formation. Icarus **195**(1), 106–160 (2008a). doi:10.1016/j.icarus.2007.11.031

F. Poulet, N. Mangold, D. Loizeau, J.-P. Bibring, Y. Langevin, J. Michalski, B. Gondet, Abundance of minerals in the phyllosilicate-rich units on Mars. Astron. Astrophys. **487**(2), L41–L44 (2008b)

R. Prakash et al., Mars Science Laboratory entry, descent, and landing system overview, in *IEEE Aerospace Conference* (2008). doi:10.1109/AERO.2008.4526283. IEEEAC paper #1531

N.E. Putzig, M.T. Mellon, Apparent thermal inertia and the surface heterogeneity of Mars. Icarus **191**, 68–94 (2007). doi:10.1016/j.icarus.2007.05.013

N.E. Putzig, M.T. Mellon, R.E. Arvidson, K.A. Kretke, Global thermal inertia and surface properties of Mars from the MGS mapping mission. Icarus **173**, 325–341 (2005)

C. Quantin, P. Allemand, N. Mangold, G. Dromart, C. Delacourt, Fluvial and lacustrine activity on layered deposits in Melas Chasma, Valles Marineris, Mars. J. Geophys. Res. **110**, E12S19 (2005). doi:10.1029/2005JE002440

S.C.R. Rafkin, R.M. Haberle, T.I. Michaels, The Mars Regional Atmospheric Modeling System (MRAMS): Model description and selected simulations. Icarus **151**, 228–256 (2001)

M.S. Rice, S. Gupta, J.F. Bell III, N.H. Warner, Influence of fault controlled topography on fluvio-deltaic sedimentary systems in Eberswalde crater, Mars. Geophys. Res. Lett. **38**, L16203 (2011). doi:10.1029/2011GL048149

S.W. Ruff, P.R. Christensen, Bright and dark regions on Mars: Particle size and mineralogical characteristics based on Thermal Emission Spectrometer data. J. Geophys. Res. **107**(E12), 5127 (2002). doi:10.1029/2001JE001580

D.H. Scott, K.L. Tanaka, Geologic map of the western equatorial region of Mars. U. S. Geological Survey Miscellaneous Investigations Series I-1802-A, scale 1:15,000,000, 1986

R.A. Simpson, J.K. Harmon, S.H. Zisk, T.W. Thompson, D.O. Muhleman, Radar determination of Mars surface properties, in *MARS*, ed. by H.H. Kieffer et al. (University of Arizona Press, Tucson, 1992), pp. 652–685

M.D. Smith, Interannual variability in TES atmospheric observations of Mars during 1999–2003. Icarus **167**, 148–165 (2004)

D.E. Smith, M.T. Zuber, The relationship between MOLA northern hemisphere topography and the 6.1-Mbar atmospheric pressure surface of Mars. Geophys. Res. Lett. **25**, 4397–4400 (1998)

D.E. Smith et al., Mars Orbiter Laser Altimeter (MOLA): experiment summary after the first year of global mapping of Mars. J. Geophys. Res. **106**, 23689–23722 (2001)

S.W. Squyres et al., Overview of the Opportunity Mars Exploration Rover mission to Meridiani Planum: Eagle Crater to Purgatory Ripple. J. Geophys. Res. **111**, E12S12 (2006). doi:10.1029/2006JE002771

A. Steltzner, D. Kipp, A. Chen, D. Burkhart, C. Guernsey, G. Mendeck, R. Mitcheltree, R. Powell, T. Rivellini, M. San Martin, D. Way, Mars Science Laboratory entry descent and landing system, in *IEEE Aerospace Conference*, Big Sky, MT (2006). IEEAC paper #1497

R.E. Summons, J.P. Amend, D. Bish, R. Buick, G.D. Cody, D.J. Des Marais, G. Dromart, J.L. Eigenbrode, A.H. Knoll, D.Y. Sumner, Preservation of Martian organic and environmental records: Final report of the Mars Biosignature Working Group. Astrobiology **11**, 157–181 (2011). doi:10.1089/ast.2010.0506

B.J. Thomson et al., Constraints on the origin and evolution of the layered mound in Gale Crater, Mars using Mars Reconnaissance Orbiter data. Icarus **214**, 413–432 (2011)

D. Tyler, J.R. Barnes, R.M. Haberle, Simulation of surface meteorology at the Pathfinder and VL1 sites using a Mars mesoscale model. J. Geophys. Res. **107**(E4), 5018 (2002). doi:10.1029/2001JE001618

M. Varma, A. Zisserman, A statistical approach to texture classification from single images. Int. J. Comput. Vis. **62**(1–2), 61–81 (2005)

A.R. Vasavada et al., Environmental characterization for the Mars Science Laboratory EDL and surface operations. Space Sci. Rev., this issue

M. Vincendon, J. Mustard, F. Forget, M. Kreslavsky, A. Spiga, S. Murchie, J.-P. Bibring, Near-tropical subsurface ice on Mars. Geophys. Res. Lett. **37**, L01202 (2010). doi:10.1029/2009GL041426

D.W. Way, R.W. Powell, A. Chen, A.D. Steltzner, A.M.S. Martin, P.D. Burhart, G.F. Mendeck, Mars Science Laboratory: Entry, descent, and landing system performance, in *IEEE Aerospace Conference*, Big Sky, MT (2007). IEEAC paper #1467

C.V. White, G. Antoun, J. Tippmann, Analysis and testing of the Mars Science Laboratory entry, descent, and landing loads—Part 2—Landing loads phase, in *53rd AIAA/ASME/ASCE/AHS/ASC Structures, Structural Dynamics, and Materials Conference*, Honolulu, HI, April 2012

S.A. Wilson, A.D. Howard, J.M. Moore, J.A. Grant, Geomorphic and stratigraphic analysis of crater Terby and layered deposits north of Hellas basin, Mars. J. Geophys. Res. **112**, E08009 (2007). doi:10.1029/2006JE002830

S.M. Wiseman, R.E. Arvidson, F. Poulet, R.V. Morris, S. Murchie, F.P. Seelos, J.C. Andrews-Hanna, CRISM Science Team, Stratigraphic context of phyllosilicate deposits in Sinus Meridiani, Mars, in *Lunar Planet. Sci.*, LPI, Houston, TX, vol. XXXIX (2008). Abstract 7035

J.J. Wray, B.L. Ehlmann, S.W. Squyres, J.F. Mustard, R.L. Kirk, Compositional stratigraphy of clay-bearing layered deposits at Mawrth Vallis, Mars. Geophys. Res. Lett. **35**, L12202 (2008)

J. Yen, B. Cooper, F. Hartman, S. Maxwell, J. Wright, C. Leger, Physical-based simulation for Mars Exploration Rover tactical sequencing, in *Proceedings of the 2005 IEEE Conference on Systems, Man, and Cybernetics*, October 2005

B. Zhang, Towards a higher level of automation in softcopy photogrammetry: NGATE and LIDAR processing in SOCET SET1. Paper presented at Geocue Corporation 2nd Annual Technical Exchange Conference, Nashville, Tenn., 26–27 September 2006

B. Zhang, S. Miller, Adaptive automatic terrain extraction. Proc. SPIE Int. Soc. Opt. Eng. **3072**, 27–36 (1997)

B. Zhang, S. Miller, K. DeVenecia, S. Walker, Automatic terrain extraction using multiple image pair and back matching. Paper presented at ASPRS 2006 Annual Conference, Am. Soc. Photogramm. Remote Sens., Reno, Nevada, 1–5 May 2006